AD-A141 866 IDENTIFICATION OF STRAIN-SOFTENING PROPERTIES AND COMPUTATIONAL PREEICTIO.. (U) COLORADO UNIV AT BOULDER DEPT OF CIVIL ENVIRONMENTAL AND ARCH.. 1/2

UNCLASSIFIED K J WILLAM ET AL. 01 MAR 84 F/G 11/2 NL

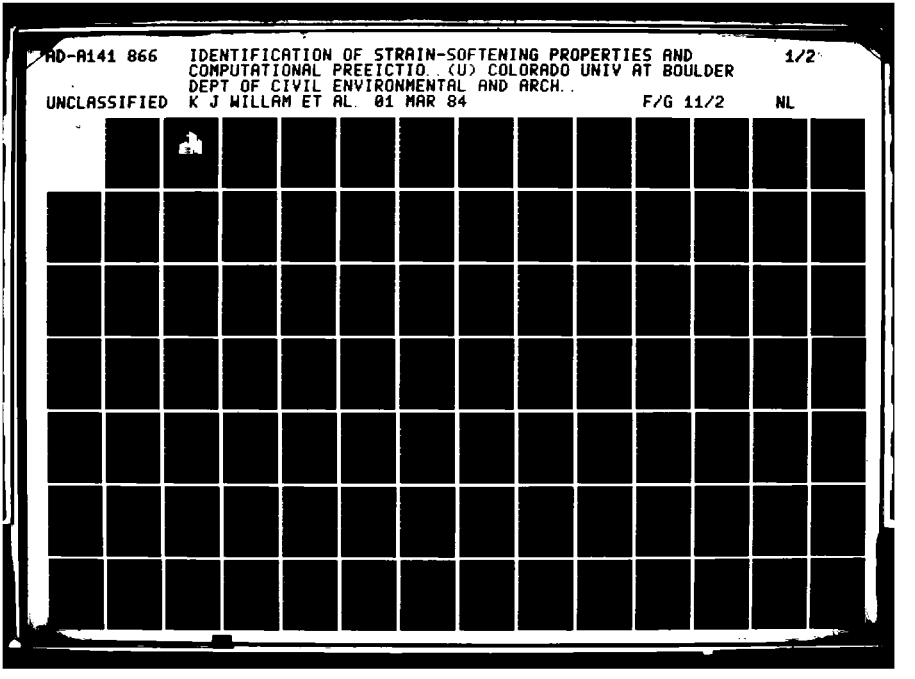

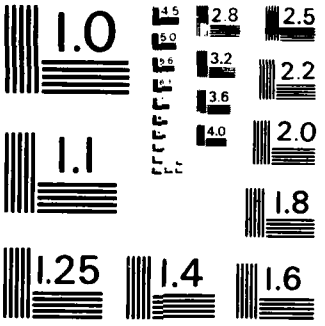

MICROCOPY RESOLUTION TEST CHART
NATIONAL BUREAU OF STANDARDS - 1963 - A

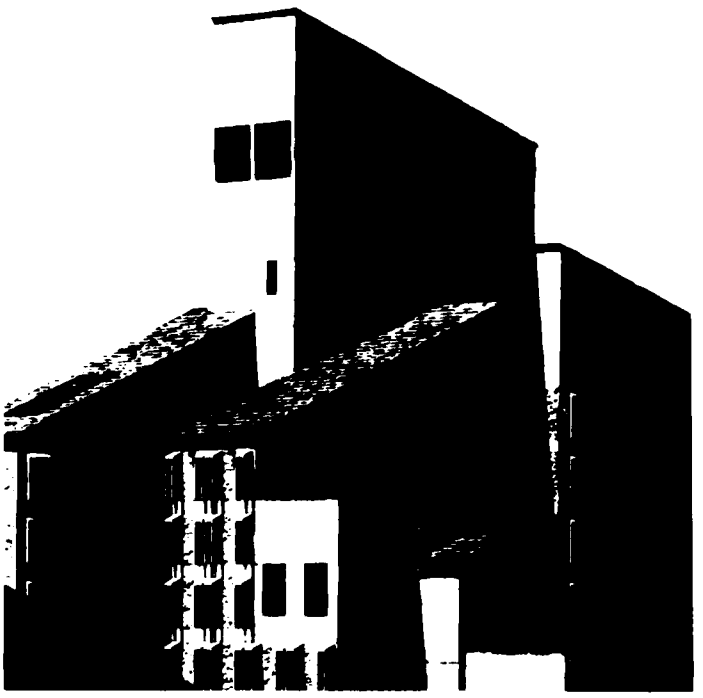

IDENTIFICATION OF STRAIN-SOFTENING PROPERTIES AND COMPUTATIONAL PREDICTIONS OF LOCALIZED FRACTURE

by

K.J.Willam, S.Sture, N.Bicanic, J.Christensen and B.Hurlbut

Department of Civil, Environmental,
and Architectural Engineering

College of Engineering
and Applied Science

University of Colorado, Boulder

Qualified requestors may obtain additional copies from the Defense Technical Information Service

UNCLASSIFIED

SECURITY CLASSIFICATION OF THIS PAGE

AD-A

REPORT DOCUMENTATION PAGE

1a. REPORT SECURITY CLASSIFICATION: Unclassified	1b. RESTRICTIVE MARKINGS
2a. SECURITY CLASSIFICATION AUTHORITY	3. DISTRIBUTION/AVAILABILITY OF REPORT: Approved for Public Release; Distribution Unlimited.
2b. DECLASSIFICATION/DOWNGRADING SCHEDULE	
4. PERFORMING ORGANIZATION REPORT NUMBER(S)	5. MONITORING ORGANIZATION REPORT NUMBER(S): AFOSR-TR. 84-0423
6a. NAME OF PERFORMING ORGANIZATION: UNIVERSITY OF COLORADO, BOULDER; 6b. OFFICE SYMBOL (If applicable)	7a. NAME OF MONITORING ORGANIZATION: HE OSR / NA
6c. ADDRESS (City, State and ZIP Code): Dept. of CIVIL, ENVIRONMENTAL & ARCHITECTURAL ENGINEERING, BOULDER, CO 80309	7b. ADDRESS (City, State and ZIP Code): Bolling HFB, DC
8a. NAME OF FUNDING/SPONSORING ORGANIZATION: OFFICE OF SCIENTIFIC RESEARCH; 8b. OFFICE SYMBOL (If applicable): AFOSR/NA	9. PROCUREMENT INSTRUMENT IDENTIFICATION NUMBER: AFOSR-82-0273
8c. ADDRESS (City, State and ZIP Code): Bolling AFB, DC 20332	10. SOURCE OF FUNDING NOS.

PROGRAM ELEMENT NO.	PROJECT NO.	TASK NO.	WORK UNIT NO.
61102F	2307	C2	

11. TITLE (Include Security Classification): "STRAIN-SOFTENING PROPERTIES & COMPUTATIONAL PREDICTIONS OF LOCALIZED FRACTURE"(Unclassified)

12. PERSONAL AUTHOR(S): K.J.WILLAM, S.STURE, N.BICANIC, J.CHRISTENSEN, J.HURLBUT

13a. TYPE OF REPORT	13b. TIME COVERED	14. DATE OF REPORT (Yr., Mo., Day)	15. PAGE COUNT
ANNUAL	FROM 8/82 TO 2/84	1984, MARCH 1	189

16. SUPPLEMENTARY NOTATION

17. COSATI CODES		
FIELD	GROUP	SUB. GR.

18. SUBJECT TERMS (Continue on reverse if necessary and identify by block number): COMPOSITE DAMAGE MODEL FOR CRACKING AND SHEAR SLIP FINITE ELEMENT COMPUTATIONS OF LOCALIZED FRACTURE DIRECT TENSION, TRIAXIAL COMPRESSION AND DIRECT SHEAR TESTS OF MORTAR.

19. ABSTRACT (Continue on reverse if necessary and identify by block number)

The main objective of the present investigation is to evaluate strain-softening formulations for contained fracture in cementitious materials such as concrete and geo-materials. This report includes two principal developments: (i) a rational approach to identify softening properties due to tensile cracking and frictional slip from displacement controlled material testing, and (ii) a systematic verification of contained fracture computations from small-scale structural testing. To this end, a composite damage model is proposed to describe the degradation of strength and stiffness in the post-peak regime with the aid of a volume fraction formulation of localized damage within a finite element.

20. DISTRIBUTION/AVAILABILITY OF ABSTRACT	21. ABSTRACT SECURITY CLASSIFICATION
UNCLASSIFIED/UNLIMITED ☒ SAME AS RPT. ☐ DTIC USERS ☐	UNCLASSIFIED

22a. NAME OF RESPONSIBLE INDIVIDUAL	22b. TELEPHONE NUMBER (Include Area Code)	22c. OFFICE SYMBOL
LAWRENCE D. HOKANSON, Lt. Col. USAF	(202) 767-4935	AFOSR/NA

DD FORM 1473, 83 APR EDITION OF 1 JAN 73 IS OBSOLETE.

UNCLASSIFIED

SECURITY CLASSIFICATION OF THIS PAGE

IDENTIFICATION OF STRAIN-SOFTENING PROPERTIES AND COMPUTATIONAL PREDICTIONS OF LOCALIZED FRACTURE

by

K. J. Willam, S. Sture, N. Bicanic, J. Christensen and B. Hurlbut

Structures Research Series, Report No. 8404
Department of Civil, Environmental and Architectural Engineering
University of Colorado, Boulder, Colorado 80309

Submitted to the Air Force Office of Scientific Research

under

Grant No. AFOSR-82-0273

March 1984

TABLE OF CONTENTS

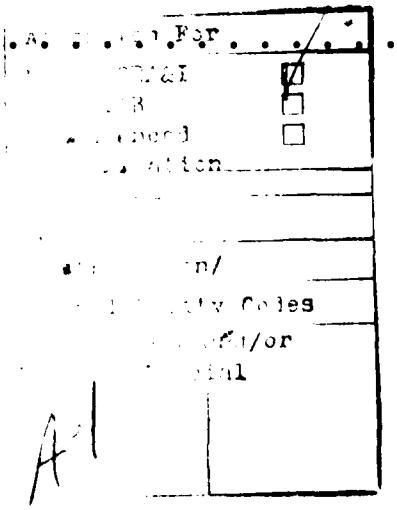

SUMMARY

The main objective of the present investigation is to evaluate strain-softening formulations for contained fracture in cementitious materials such as concrete and geomaterials. This report includes two principal developments: (i) a rational approach to identify softening properties due to tensile cracking and frictional slip from displacement controlled material testing, and (ii) a systematic verification of contained fracture computations from small-scale structural testing. To this end a composite damage model is proposed to describe the degradation of strength and stiffness in the post-peak regime with the aid of a volume fraction formulation of localized damage within a finite element.

The identification of softening properties requires the solution of inverse boundary value problems since the contained fracture process introduces stress redistribution and strain localization, even though the test specimen may be initially homogeneous. As a result displacement controlled post-peak testing does not directly provide material properties but rather structural properties of a fractured discontinuum, which can be used for the idealization of an "equivalent" continuum. To this end two localization parameters are introduced for tensile cracking and frictional slip which define, the extent of material damage as compared to the intact elastic volume, and which provide a characteristic length measure into the strain-softening material formulation. The principal issue with regard to these localization parameters concerns the concept of a fracture process zone which has been introduced in nonlinear

fracture mechanics as an intrinsic fracture property independent of the particular boundary value problem. Therefore, the immediate question arises whether these localization parameters provide a "proper" fracture property or if they are merely mesh size dependent softening parameters which control the overall degradation of strength.

The results of the current investigation demonstrate that these localization parameters are not really a fracture property when distributed cracking and shear slip in unnotched specimens is considered. In this case one cannot assign the entire fracture energy of the specimen to a single element without introducing severe mesh size effects if fracture is not confined to a single predominant fracture band like in notched specimens.

1. INTRODUCTION

1.1 Objective

The finite element method is often used in a rather indiscriminate manner to predict the ultimate load capacity and the associated failure mechanism of structures and solids. Traditionally the concepts of nonlinear elasticity and hardening plasticity have been adopted and extended to model the local material behavior in the pre-and and post-peak regime. Brittle and ductile fracture was simulated in the form of degrading stress-strain relations within the "smeared" approach, in which the localized discontinuities of the field variables were distributed, or rather homogenized, over tributary areas within each finite element. In this way, progressive damage accumulation and the localization of the failure zone were modeled within the framework of hardening/softening constitutive mechanics and were thus readily amenable to standard computational strategies. The inherent instability of local material softening was restrained by the redistribution capacity of the structural configuration during contained fracture propagation. Clearly the strong path- and history-dependence of these confined material instabilities required sophisticated computational methods in order to ensure numerical solutions which would be on one hand sufficiently robust to trace contained fracture propagation and on the other hand sufficiently sensitive to discover imminent structural failure.

Along this line the question was usually raised whether the softening branch of the global load-deformation relationship was a true

material property or simply the result of the experimental configuration and boundary conditions. Recognizing that the post-peak regime was a structural rather than a material phenomenon it was natural to question the extrapolation of these softening properties to other structural configurations.

On the other hand these fundamental questions of structure-independent strain-softening properties appeared again in the discrete fracture approach in the form of decohesive interface properties. In this case the progressive fracture process involved a continuous updating of the structural toplogy, whereby the inherent instability of the strain-softening material formulation was replaced by latent instability of crack growth on the structural level. Although some of the inconsistencies of the softening continuum approach were circumvented in this way, new complications arose with the definition of appropriate contact and interface conditions, which played the same role as the softening branch in the smeared continuum model.

In view of these pressing questions of the smeared and the discrete fracture approaches a comprehensive research program was initiated August 1, 1982 at the University of Colorado, Boulder. The main objective was to scrutinize the computation of progressive damage in structural components up to and beyond collapse. To this end the shortcomings and limitations of the smeared fracture approach were to be explored and compared with pertinent experimental evidence. The main goal was to examine the arguments of the continuum fracture strategy and to delineate guidelines on the range of applications. It was felt that

these basic questions were sufficiently fundamental to all engineering materials exhibiting brittle or ductile fracture in addition to concrete and geotechnical materials which were of immediate concern.

1.2 Scope

The report summarizes the results of the experimental and computational study of contained fracture. Based on Kachanov's concept of continuous damage, a strain-softening formulation will be developed which describes the degradation of strength in terms of the ratio of damaged to undamaged volume. The triaxial strength is described by the Mohr-Coulomb criterion of frictional slip and the tension cut-off condition of tensile cracking. Particular attention will be devoted to the systematic identification of the shear and tension softening properties from triaxial compression tests at different confining pressures and uniaxial tension tests. An inverse identification procedure will be utilized for the characterization of the composite damage model parameters using displacement controlled test data in the post-peak regime. Because of the structural aspects of stress redistribution and fracture localization a series of nonlinear boundary value problems have to be solved in order to quantify the localization of damage within the test specimen. The element localization parameter, or rather the damage volume fraction, determines the rate of overall strength degradation of the specimen in relation to a particular mesh-layout. Moreover, this scalar measure of damage is a function of confining pressure in order to accommodate different softening rates ranging from brittle cracking in tension to ductile slip in shear. The results of several parameter

studies will illustrate the mesh sensitivity of this softening formulation and will answer partially the question if this localization parameter is a proper fracture property which could be physically attributed to the size of the fracture process zone.

Subsequently the resulting strain-softening damage model will be applied to contained fracture predictions. To this end servo-controlled test data obtained in our high capacity direct shear test apparatus will be used for comparison. For different ratios of normal to tangential load level tensile cracking as well as frictional slip take place within the specimen and lead to an overall degradation of shear strength within the specimen down to the residual strength level. Due to the high confinement of the shear box the fracture process is fully contained similar to overstressed regions in a highly indeterminate structure. In this context the direct shear test specimen constitutes a miniature structure and thus furnishes important experimental information for the verification of computational fracture predictions.

1.3 Related Work

Recent progress in the area of servo-controlled testing and the increasing demand of computational mechanics for more realistic material descriptions has led to extensive research efforts in the field of constitutive mechanics. However, in spite of massive activities the reliable prediction of brittle and ductile fracture has been elusive to a large extent and has generated considerable controversies among leading researchers. On the continuum level two approaches have been pursued in the past along the lines of (i) strain-softening continuum models and

(ii) discrete fracture formulations. These two opposing concepts have been partly reconciled in the recent past by bifurcation models in which the localization of the fracture band results from progressing material instabilities in the structure. Another rapidly growing area which has contributed to the development of a more rational approach to fracture is the field of damage mechanics and the underlying state variable formulations. An extensive literature review of the on-going experimental, computational and constitutive modeling work should clearly fill a publication of its own. In the following we will restrict our attention to those contributions which are of immediate concern to the subsequent investigation of localized fracture in concrete and geotechnical materials.

(i) Experimental Studies:

On the experimental side we refer to the early strain-softening studies by Sture and Ko [1] who examined the post-peak behavior and shear band development in rocks with the structurally stiff triaxial Hoek cell device developed at C.U. Boulder. We also make use of our large capacity direct shear apparatus which was originally designed by Sture [2] for studying interface behavior e.g. of rock joints. In the context of the present investigation this servo-controlled test device will be employed to verify our computational fracture predictions of confined cracking and frictional slip. In the field of tension testing some of the early test results by Heilmann [3] on unnotched specimens are utilized as well as the recent fracture energy studies by Petersson [4]. Along

this line a forthcoming paper by Gopalaratnam and Shah [5] summarizes the current findings in tension testing of concrete considering primarily notched test specimens. This experimental work will be complemented by our own developments in displacement controlled tension testing of cylindrical mortar specimens that are further described in Section 3.

(ii) Computational Studies:

On the computational front we refer to the softening methodology forwarded earlier by Argyris, Faust and Willam [6] in which the effect of different strain-softening models for tension and shear was examined in conjunction with structural failure predictions. This engineering approach to fracture was used in our previous study of confined fracture in concrete and mortar samples which were tested in the direct shear test [7]. In our attempt to incorporate localization into the smeared strain-softening approach we make use of the elastic-plastic Mohr-Columb model of Pietruszczak and Mroz [8] on several occasions. In this context we repeatedly refer to the blunt crack band approach of Bazant and co-workers [9] who interpreted the fictitious crack model of Hillerborg et al [10] within a crack band of finite rather than infinitesimal width. With reference to the discrete fracture models we intend to resort to the work of Saouma and Ingraffea who described in Ref. [11] the current state-of-the-art of modeling slow fracture propagation and interactive remeshing. Although we will not directly pursue material bifurcation in this report we wish to acknowledge

the fundamental stability studies of Rudnicki and Rice [12] who showed that the localization of shear bands originates in a constitutive instability. In fact, several bifurcation studies have been recently put forward in the geotechnical area, e.g. by Vardoulakis [13] and Vermeer [14] which followed essentially the early development of Hill [15] on the stability and uniqueness of materials. In the context of necking of metals the concept of void nucleation and the resulting structural instability studies advocated by Needleman and Tvergaard [16] are particularly noteworthy since they suggest an alternative approach for tracing fracture localization into the post-peak regime.

(iii) Constitutive Studies

On the constitutive front we wish to acknowledge the continuous strain-softening plasticity formulations proposed earlier by Dougill [17] for elastic fracturing continua and by Naghdi and Trapp [18] within the strain space formulation of plasticity. For our subsequent development of a composite damage model for softening we make use of the original work by Kachanov [19] and refer to the recent developments of continuous damage formulations by Lemaitre and Chaboche [20] as well as by Krajinovic and Fonseka [21].

2. BASIC OBSERVATIONS

2.1 Servo-Controlled Testing

Modern servo-controlled testing e.g. with MTS material testing systems provides additional information on the mechanical response behavior and new insight into the apparent ductility of engineering materials. In particular the nature of fracture appears in another light if displacement controlled experiments are carried out in sufficiently stiff test set-ups. In fact, brittle materials or rather materials which exhibit brittle fracture under load-controlled testing can show considerable ductility under displacement control. But even ductile materials such as mild steel exhibit distinct differences in the response behavior particularly if local material instabilities are considered at initial yield or in the post-peak regime. Figs. 2-1 and 2-2 clearly demonstrate the remarkable differences of load and displacement controlled tests on mortar and steel specimens under uniaxial tension. In both cases the overall load-deformation response data are plotted directly from the output signals. The subsequent extraction of actual material properties raises immediately questions with regard to the appropriate stress-strain measures, the localization of strains within the test specimen and the interpretation of discontinuous fracture bands within a continuum formulation when the post-peak regime is considered.

From the dimensions in both Figs. 2-1 and 2-2 we observe that the overall displacements differ by two orders of magnitude for comparable specimen lengths. As a result the ductile fracture of metals involves large changes of the test geometry and therefore requires a large strain

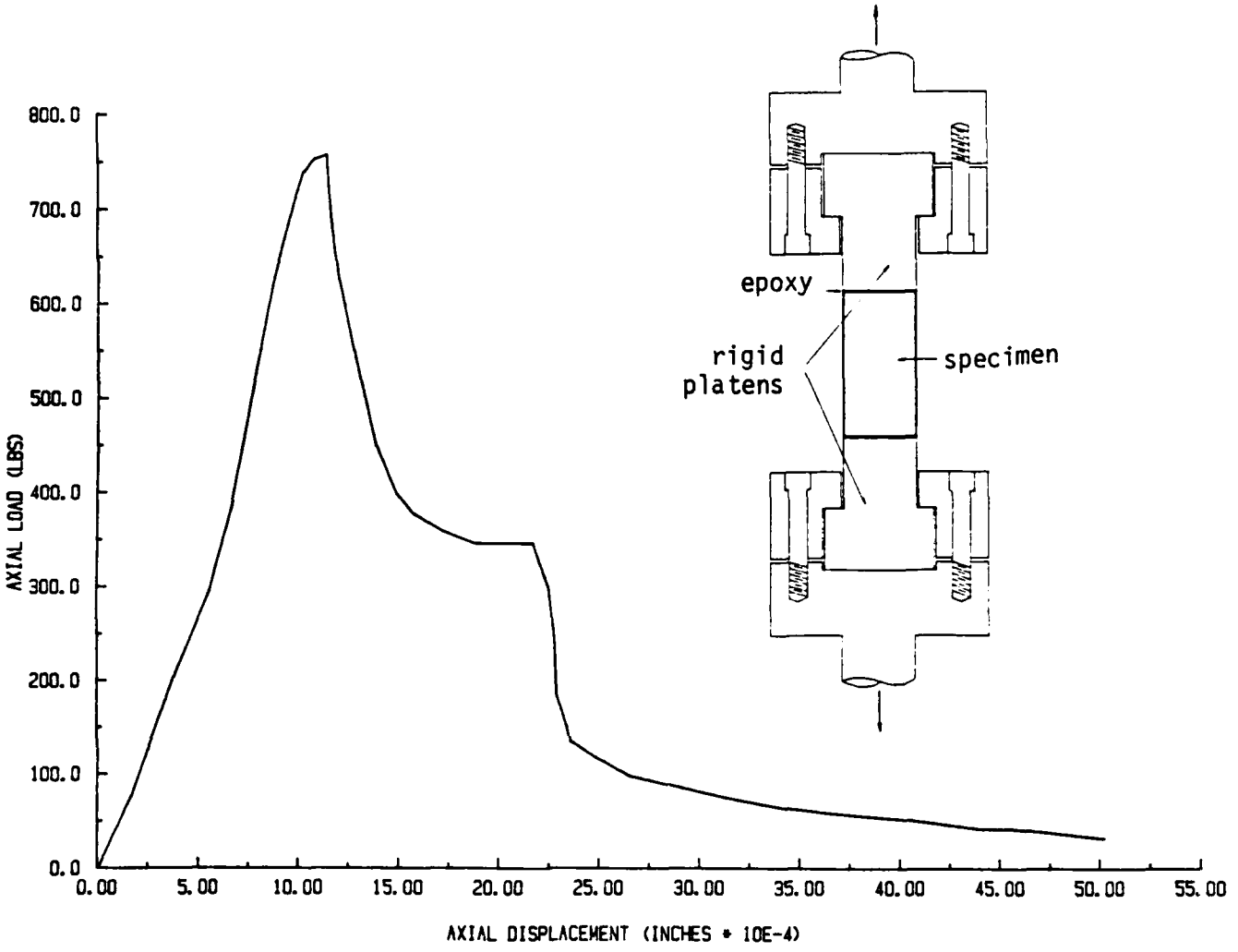

Fig. 2-1 Load-elongation diagram of NX-size mortar specimen under displacement (stroke) control (cylinder size 5.40 x 11.43 cm).

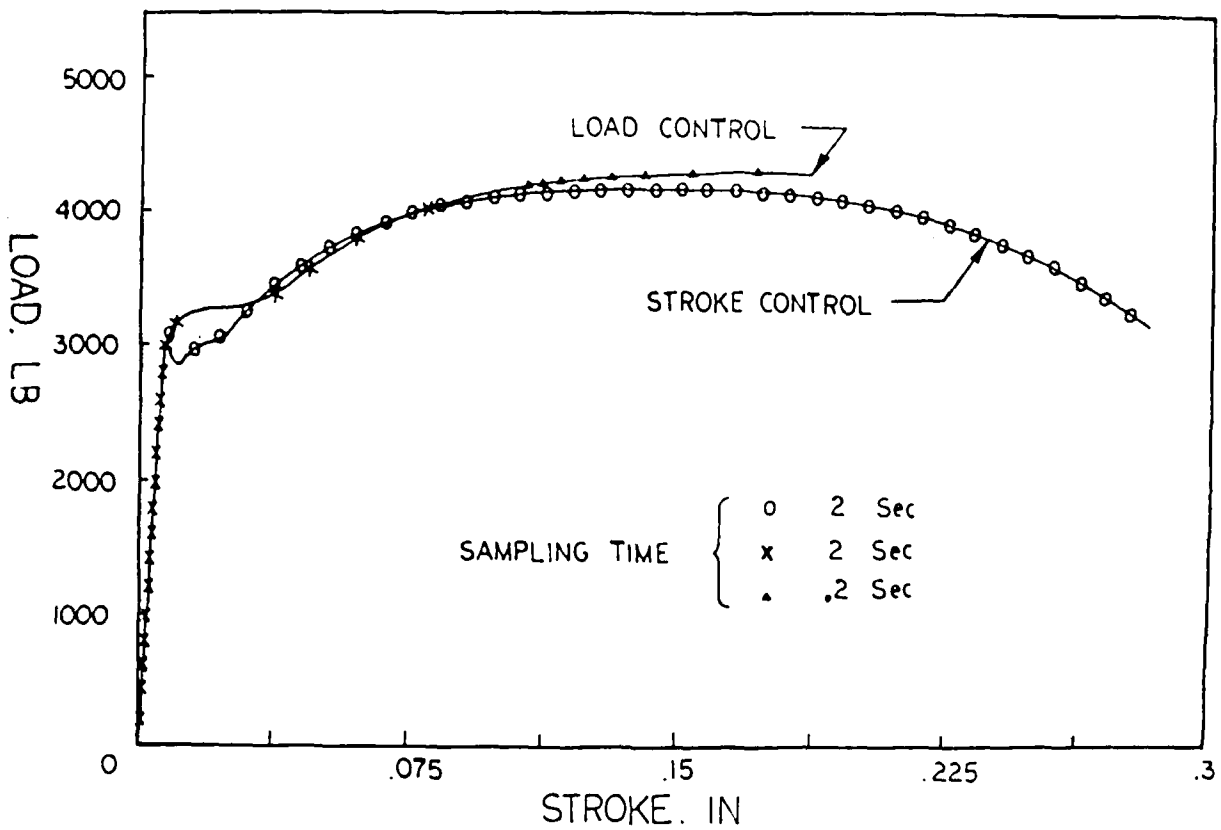

Fig. 2-2 Load-elongation diagram of SAE 1020 steel specimens tested under load and displacement (stroke) control). Note the absence of the yield point and of the post-peak regime under load control. The two specimens have identical geometry [40].

formulation for the proper interpretation of slip bands during necking. In contrast, the brittle fracture of cementitous materials such as concrete and mortar does not involve any noticeable change of the specimen geometry up to the localization of a discrete crack band. In fact, a discrete hairline crack becomes visible only in the very final stage of decohesion in the post-peak regime when the force level approaches zero. As a result, the softening behavior of the specimen can not be explained by large deformations or geometric effects such as necking but rather by decohesion within a stable material fabric due to debonding and progressive microcracking. Consequently, we restrict the development of a composite damage theory of fracture to the theory of small displacement gradients.

Because of the basic differences between load- and displacement-controlled testing we have to ask ourselves if the apparent ductility of servo-controlled experiments can be mobilized in an actual structure and if the computational predictions should include these effects. The answer is clearly in favor of material data from displacement-controlled testing in view of the predominant role of the displacement formulation for the numerical solution of initial boundary value problems in the mechanics of solids and structures. The underlying approximations of the displacement field and the ensuing computational strategies result in displacement-controlled algorithms for nonlinear analysis. Therefore, the finite element displacement method of discretization requires a consistent strain-based formulation of the material behavior and a contiguous displacement control for material testing. Moreover, if we

material models from displacement-controlled testing, the solution of kinematically unconfined boundary value problems will reproduce load-controlled test data if no stress redistribution can take place on the structural level. As a result, displacement control, both experimental as well as computational, simply extends the scope of our numerical predictions into the regime of ductile fracture which is not accessible under load control.

2.2 Strain-Softening and Localization of Fracture

The principal issue of displacement controlled testing is the interpretation and extraction of proper material properties from the overall softening data. We recall that the direct tension test of the mortar specimen in Fig. 2.1 showed no noticeable change of geometry in the post-peak regime. In fact, a hairline crack of the order of 10^{-3} cm developed only at the final test stage when the load bearing capacity had practically diminished to zero. From that particular test it is apparent that decohesion takes place within the material microstructure far before a discrete tension crack develops across the specimen.

In the absence of noticeable changes of the geometric configuration both large deformations and discrete crack mechanics do not provide an obvious explanation. This suggests that strain-softening of the material itself should be considered in order to interpret the degradation of overall strength of the intact specimen in the post-peak regime. In fact, this simple concept has been used in the past within the so-called smeared crack approach to monitor the apparent ductility of solids as described, for example in the recent textbook by Chen and Saleeb [22].

Traditionally, several criticisms have been voiced in the past against strain-softening constitutive models. The negative tangent material modulus $E_T \leq 0$ obviously violates the basic Drucker requirement for stable materials, $E_T > 0$. The lack of positive definiteness introduces complex wave speeds and leads to the loss of uniqueness. In fact, the principle of local action in continuum mechanics of simple materials is in direct conflict with the entire notion of strain-softening and the inherent generation of energy. In this context some of the classical results of Hadamard [23] are often put forward where it was demonstrated that non-positive definite material behavior leads to unbounded error propagation in the context of wave mechanics.

These observations usually originate from basic principles of linear and nonlinear elasticity and are thus not in conflict with a more appropriate interpretation of strain-softening within the framework of non-equilibrium thermodynamic processes. Clearly, strain-softening is the global aspect of changes of the internal material structure which take place in cementitious materials in the form of microcracking, void nucleation and decohesion of the heterogeneous microstructure. Therefore, it is necessary to interpret strain-softening as a non-equilibrium process rather than an equilibrium state. Therefore it is mandatory to describe softening in terms of evolutionary constitutive equations in the form of either plasticity, viscoplasticity or internal variable-based damage formulations with real time or intrinsic time being the independent process variable.

The generation of energy during softening clearly solicits a synergetic approach in which other forms of energy are considered such as

acoustic emissions and heat production quite aside from the kinetic energy of the dynamic fracture process. But even if only an isolated quasistatic mechanical system is considered, there are two possibilities for interpreting the energy release during strain-softening in terms of

(i) fracture mechanics, where a specific amount of fracture energy is required to open a discrete crack surface,

(ii) continuous damage mechanics, where a specific amount of energy is required for the rearrangement of the internal microstructure.

These two concepts lead to fundamentally different formulations as far as constitutive modeling is concerned. The fracture mechanics approach leads to an explicit dependence on a characteristic size, i.e., the localization of the fracture process zone which arises from the conversion of volume energy into surface energy in the constitutive operator. In contrast, the continuous damage approach and the related softening plasticity and viscoplastic models do not introduce a size effect in the constitutive relations, since the damage zones are distributed according to the evolution of the governing process variables. In this case the localization of damage is an implicit result rather than an explicit statement, e.g. of the fracture band models [9] where the material damage is a priori confined to the width of the fracture process zone.

The main subject of the present investigation is this characteristic length and how it affects the computational fracture predictions with regard to mesh size.

2.3 Stable Control of Post-Peak Strength Behavior

In the past it was repeatedly suggested that strain-softening is really a structural instability problem, as asserted by Dougill [24] and Maier et al [25]. Recently, softening has been attributed to strain localization within a narrow fracture band. This choice of instability mode was originally proposed by Rudnicki and Rice [12] for the formation of shear bands. This feature was later adopted by several investigators for the purpose of examining the orientation of shear bands within linear bifurcation studies [13], [14]. In fact, Bazant offered some elementary strain-softening interpretation of concrete in compression [26] along similar lines. Although the study was limited to uniaxial conditions and yielded quite unrealistic modes of strain localization, the simple one-dimensional spring model offered an important insight into the fundamental aspects of strain-softening behavior. He concluded that although "strain-softening is impossible in a continuum" it can exist in a "heterogeneous material if strain localization is considered." Moreover, the size of the localization band should be of the same order as the maximum aggregate since a uniform deformation is assumed to prevail in the fracture band. As a result of the inhomogeneity of concrete, the equivalent continuum considerations are restricted to geometries that are considerably larger than the maximum aggregate. This size limitation is in obvious conflict with the principle of local action of simple materials where the behavior is governed by point measures of stresses and strains obtained from a limiting process of decreasing neighborhoods.

A similar interpretation for the formation of shear bands in rocks was offered by Sture and Ko [1] in the context of the triaxial compression test. In this case the stiffness of the test set-up was considered in the form of parallel as well as series springs in conjunction with the test specimen. This basic strain-softening study of brittle materials clearly demonstrated that stable control of the post-peak regime can not be assured by displacement control alone but it also requires a test device which is sufficiently stiff compared to the test specimen. Again, simple stability considerations showed that strain-softening can only exist if strain localization is introduced in a shear band of finite width.

In view of the importance of these stability arguments with regard to the forthcoming damage formulation, let us briefly review the principal reasoning. To this end we will pursue the stable localization of a crack band in the direct tension test.

Let us consider the elementary axial stiffness model of the direct tension test illustrated in Fig. 2-3. The parallel and series springs k_p and k_s represent the stiffness of the loading frame. The specimen, which is subjected to the prescribed extension $du_p>0$ of the loading platen, remains intact up to the point of incipient instability due to the localization of a crack band of the width L_d. At this stage progressive damage takes place uniformly within the crack band at the softening rate k_d while the remaining portion of the tension specimen unloads elastically along k_e.

If we neglect for the time being geometric stiffness effects which tend to stabilize rather than destabilize the tensile system, we can

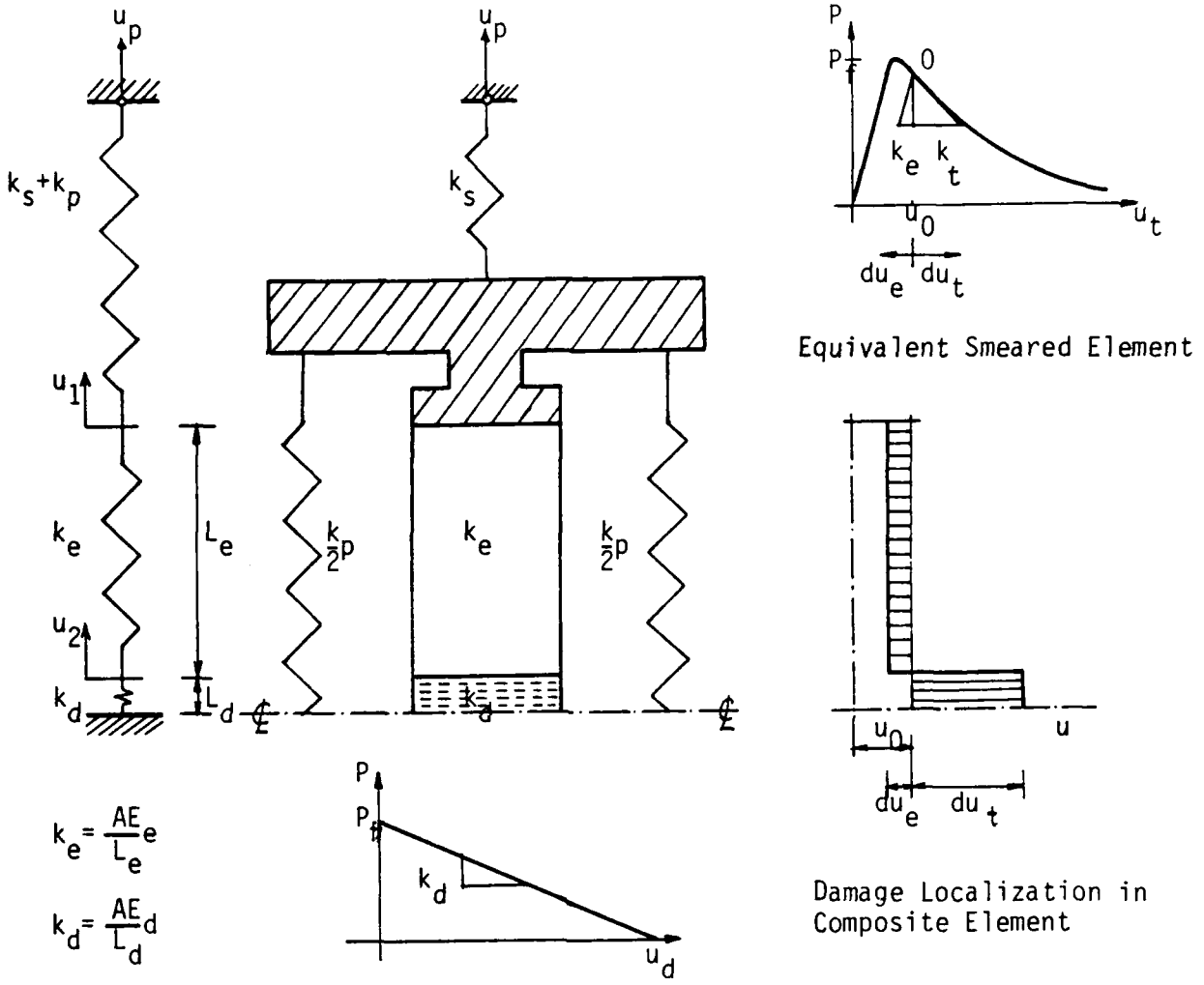

Fig. 2-3 Uniaxial model of direct tension test setup. Decomposition of equivalent smeared element into composite element of intact elastic and weakening damage behavior.

examine the stability of the strain-localization mode simply from the loss of positive definite stiffness of the entire test system. Assuming that a stable equilibrium configuration has been reached which corresponds to point 0 of the stress-strain diagram, a small perturbation leads to incipient instability if the tangential stiffness matrix $\mathbf{K}_T$ becomes singular, i.e., if det $[\mathbf{K}_T] = 0$.

$$\mathbf{K}_T \, d\mathbf{r} = 0 \quad \text{where} \quad \mathbf{K}_T = \begin{bmatrix} k_p+k_s+k_e & -k_e \\ -k_e & k_e+k_d \end{bmatrix} \text{and } d\mathbf{r} = \begin{bmatrix} du_1 \\ du_2 \end{bmatrix} \tag{2.1}$$

with k_p = spring stiffness of parallel test frame

k_s = spring stiffness of in series test frame

$k_e = \dfrac{AE_e}{L_e}$ elastic unloading stiffness of undamaged specimen region

$k_d = \dfrac{AE_d}{L_d}$ softening stiffness of localized damage region

Expansion of the characteristic equation det $\mathbf{K}_T = 0$ leads to the following restriction of the ratio between the tangential softening modulus E_d and the elastic unloading modulus E_e

$$-\frac{E_d}{E_e} \leq \frac{L_d}{L_e + \dfrac{AE_e}{k_s + k_p}} \tag{2.2}$$

Although similar results have been obtained before for uniaxial and triaxial compression tests by Bazant [26] and Sture and Ko [1], it

is worthwhile recalling some of the implications of the stability requirement above. From the inequality Eq. (2.2) we conclude:

(i) When $L_d \to 0$ the damage region diminishes within the specimen. This infers that the tangent softening modulus must remain positive semi-definite, $E_d \geq 0$ corresponding to the traditional postulate of elastic material stability.

(ii) when $L_e \to 0$ the damage region occupies the entire specimen, i.e., $L_d = L_t$. This implies that fully stable control can be maintained during softening as long as the damage stiffness remains smaller than the stiffness of the experimental apparatus.

$$-k_d \leq k_s + k_p \quad \text{where} \quad k_d = \frac{AE_d}{L_d} = \frac{AE_t}{L_t} = k_t \tag{2.3}$$

For perfectly brittle material behavior with $k_d = -\infty$ stable displacement control of the post-peak regime is therefore only possible with infinitely stiff test set-ups, $k_s + k_p \to \infty$.

(iii) when the stiffness of the test apparatus increases, $(k_s + k_p \to \infty)$, stable softening is controlled entirely by theratio of damage to intact elastic volume or their respective stiffnesses k_d and k_e

$$\frac{AE_d}{L_d} + \frac{AE_e}{L_e} \geq 0 \text{ or } -\frac{E_d}{E_e} \leq \frac{L_d}{L_e} \tag{2.4}$$

This simple result implies that for stable post-peak behavior the elastic unloading stiffness k_e must remain larger in absolute value than the softening stiffness of the damaged region k_d. In view of the experimental strain-softening evidence in ref. [5] it is apparent that the softening stiffness decreases in the post-peak regime with decreasing strength. There are two obvious possibilities: either the damage volume $V_d=AL_d$ increases during fracture localization, which leads to an increase of the elastic stiffness since $L_d=L_t-L_e$, or the damage volume fraction remains fixed, L_d/L_e=constant. In this case the decrease of damage modulus E_d must be accompanied by an equivalent decrease of the elastic unloading modulus E_e. In fact the cyclic unloading tension test results published by Shah et al. [5] seem to confirm the latter proposition of keeping L_d/L_e=constant.

These simple observations lead directly to the fundamental issue that strain-softening is <u>not</u> a local material property but rather a structural property. In fact, we have seen from the elementary consideration above that the softening stiffness involves a finite damage volume $V_d= A\ L_d$ and introduces a non-local aspect into the constitutive formulation. In contrast to the continuum theories of hardening materials it is therefore mandatory to accommodate size effects in a continuous softening formulation since $L_d>0$ for stable post-peak behavior. For computational fracture predictions the basic issue then revolves around the question: Is the size of the damage zone L_d a fundamental fracture property which could be interpreted as the width of the fracture process zone, or is the damage volume fraction L_d/L_e a fracture parameter which is independent of the mesh size and the

particular boundary value problem considered?

The elementary analysis of the uniaxial tension test above was based on the assumption that geometric effects remain negligible and that instability occurs only due strain localization of the axial deformations. In fact, it was observed earlier that the geometric stiffness introduces a stabilizing rather than destabilizing effect in the tension specimen. The usual bifurcation analysis along the line of a linearized eigenvalue solution of the tangential stiffness in a stressed configuration states:

$$(\mathbf{K}_E + \lambda\, \mathbf{K}_G)\, d\mathbf{u} = 0 \qquad (2.5)$$

Eq. 2.5 does not lead to destabilization if the critical buckling load remains positive, i.e., tensile. However, it has been suggested on several occasions that the geometric nonlinearities will have a significant influence on the peak strength behavior and thus also the post-peak response if the elastic stiffness $\mathbf{K}_E$ diminishes and becomes singular, e.g., when $E_S \to 0$. For this reason let us consider the full scope of Eq. 2.5 and the relative order of magnitudes of $\mathbf{K}_E$ and $\mathbf{K}_G$ of the simple uniaxial idealization of the direct tension test above.

To this end we restrict again our attention to the uniaxial instability mode because the experimental evidence in Fig. 2-1 does not support any transverse motion in the entire response regime. In this case the usual contribution of the finite rotation $\theta = 1/2\ (dv/dx)^2 \to 0$ to the geometric stiffness $\mathbf{K}_G$ can not be mobilized. The only term of the strain-displacement relation arises from the quadratic strain term ε_{NL}

$1/2(du/dx)^2$. As a result the following geometric stiffness matrix arises for the axial force member

$$K_G = \frac{A\sigma_0}{L}\begin{bmatrix} 1 & -1 \\ -1 & 1 \end{bmatrix} \tag{2.6}$$

The basic stability condition in Eq. 2.1 then simply expands into

$$\det\left\{\begin{bmatrix} k_p+k_s+k_e & -k_e \\ -k_e & k_e+k_d \end{bmatrix} + \lambda \begin{bmatrix} k_g & -k_g \\ -k_g & k_g \end{bmatrix}\right\} = 0 \tag{2.7}$$

where $k_g = \frac{A}{L}$ and $\lambda = \sigma_o$

For the case of an infinitely stiff experimental apparatus-specimen system under displacement control we can restrict our argument to $K_T(2,2) = 0$

$$k_e + k_d + \lambda k_g = 0 \tag{2.8}$$

As a result the effect of initial stress $\lambda=\sigma_0$ leads to the following requirement for stable control of the post-peak regime

$$-\frac{AE_d}{L_d} \leq \frac{AE_e}{L_e} + \frac{\lambda A}{L_t} \quad \text{where } \lambda = \sigma_0 \tag{2.8}$$

In comparison to Eq. 2.4 this condition verifies that the tensile stress state $\lambda=\sigma_0>0$ helps to stabilize or maintain control in the strain-softening regime. In fact if λ is of the same order of magnitude as the

softening modulus, i.e., $\sigma_0=0(E_d)$, then softening control can be maintained irrespective of the elastic unloading modulus E_e as long as $L_d>0$.

$$-\frac{E_d}{L_d} \leq \frac{E_e}{L_t-L_d} + \frac{\sigma_0}{L_t} \tag{2.9}$$

In the compression test, however, the geometric stiffness term introduces an additional destabilizing effect which has been omitted in the previous stability studies of the uniaxial and triaxial compression tests [1,26].

2.4 Fracture Energy Concepts

The origin of fracture mechanics dates back to the early work of Griffith who investigated the brittle fracture of glass. The basic concept of the Griffith theory is related to the notion of an interfacial stress layer in solids similar to surface tension in liquids. Crack propagation in elastic solids is thus governed by the exchange of external work W and internal energy U with the surface energy Γ necessary for advancing the crack. The energy balance during slow crack advance may be expressed as

$$d\,(W-U) = d\Gamma \tag{2.10}$$

where the kinetic energy contribution is assumed to remain negligible. If A denotes the surface area of the crack, then the energy balance due to an increase in the crack surface area is simply

$$\frac{\partial W}{\partial A} = \frac{\partial U}{\partial A} + \frac{d\Gamma}{dA} \tag{2.11}$$

Since the fracture resistance of structural materials is several orders of magnitude larger than the specific surface tension energy $\gamma = d\Gamma/dA$, this theory was revived and extended only much later by Irwin and Orowan who included a dissipative energy component in the form of plastic work at the crack front. However, in the case of small-scale yielding when the energy dissipation around the crack front is very small compared to the crack length then the energy W-U "pumped" into the fracture zone can still be calculated from a purely elastic fracture mechanics solution, using stress intensity factors, the J-integral [27] or equivalent energy (compliance) methods.

The stability of quasi-static fracture propagation may be determined from the variation of Eq. 2.10

$$\frac{d}{dA}\left[\frac{\partial}{\partial A}(W-U) - \frac{d\Gamma}{dA}\right] \begin{cases} > 0 & \text{unstable fracture} \\ = 0 & \text{neutral equilibrium} \\ < 0 & \text{stable fracture} \end{cases} \tag{2.12}$$

We can rewrite this stability condition if we define the internal mechanical energy available for a small crack extension dA as

$$G = \frac{\partial}{\partial A}(W-U) \tag{2.13}$$

and the specific energy necessary to advance the crack as

$$G_c = \frac{d\Gamma}{dA} \tag{2.14}$$

which designates the fracture toughness of the particular material and is known under the name of specific fracture energy or the critical strain energy release rate. In this case the fracture stability condition Eq. 2.12 reduces to the analysis of the scalar function

$$f = G\ (P,A) - G_c \tag{2.15}$$

with regard to the energy released and the energy required for stable or unstable crack growth. Therefore for stable crack growth df=0 and in the event G_c=const the crack propagation under variable loading dP must satisfy the consistency condition

$$dG = \frac{\partial G}{\partial A}\, dA + \frac{\partial G}{\partial P}\, dP = 0 \tag{2.16}$$

Stable crack propagation is thus only possible if the loading is adjusted according to the crack growth dA by

$$dP = - \frac{\frac{\partial G}{\partial A}}{\frac{\partial G}{\partial P}}\, dA \tag{2.17}$$

This control requirement includes hardening as well as softening of the overall load-crack propagation response.

In the case of quasistatic cracking the strain energy release can be readily visualized if we consider the split beam experiment illustra-

ted in Fig. 2-4 with an initial crack length A_1 which advances under displacement control to $A_2=A_1+\Delta A$. The underlying structural response follows the path OAB where k_1 and k_2 define the stiffnesses of the two cantilever beams of lengths A_1 and A_2.The hatched area defines the energy which is released for advancing the crack A_1 by ΔA. Depending on the geometry and boundary condition, crack propagation takes place under increasing loading in stable or sometimes entirely unstable fashion. Fig. 2-5 illustrates some typical examples of stable and unstable crack growth with plots of their respective load-displacement diagrams. Clearly a soft testing apparatus captures only stable crack growth for $\Delta P>0$ and $\Delta u>0$, while a sufficiently stiff test device can maintain stable control for $P<0$ and $\Delta u>0$. However, cracking in the classical Griffith test is fundamentally unstable and can not be controlled since $\Delta u<0$ as well as $\Delta P<0$. This means that there is so much strain energy stored in the specimen that some energy must be removed from the specimen in the form of work corresponding to the area "mcbn" in Fig. 2-5 in addition to the fracture energy during crack propagation.

For concrete-type materials Petersson [4] proposed a simple approach for evaluating G_c directly from the global load-deformation data by equating the energy of crack formation to the work done by the external forces. In the case of the direct tension test, this concept infers that G_c is simply the area under the nominal stress-elongation diagram as seen in Fig. 2-6. Since all softening deformation takes place in the localized fracture zone extending through the entire cross--sectional area,

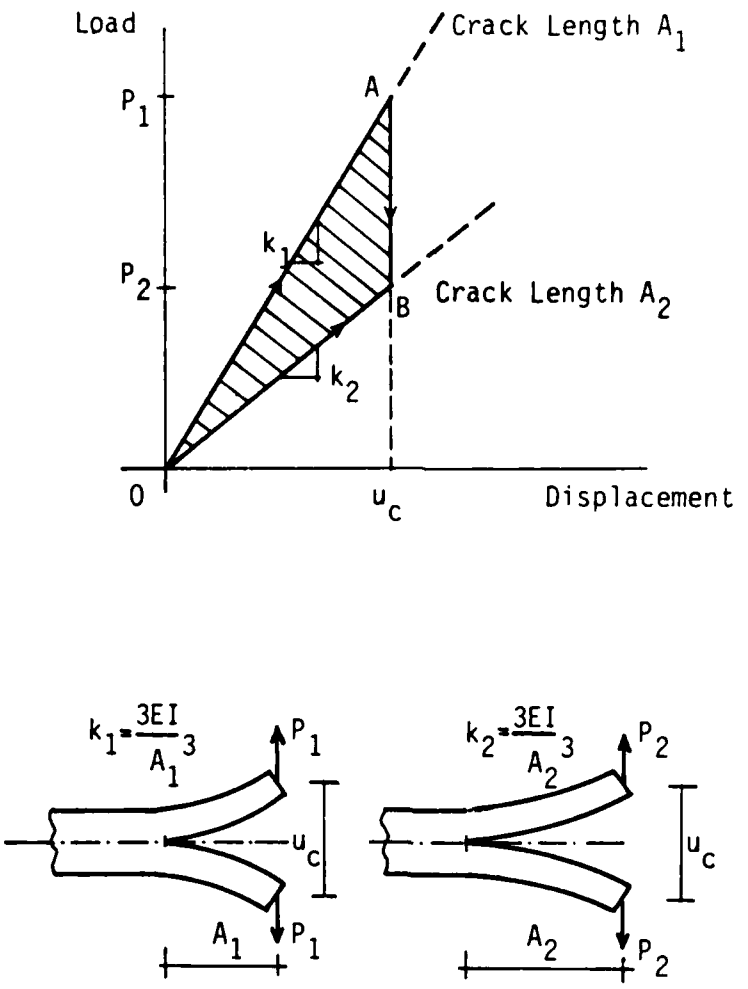

Fig. 2-4 Energy interchange during crack propagation from A_1 to A_2 under constant displacement, u_c = const.

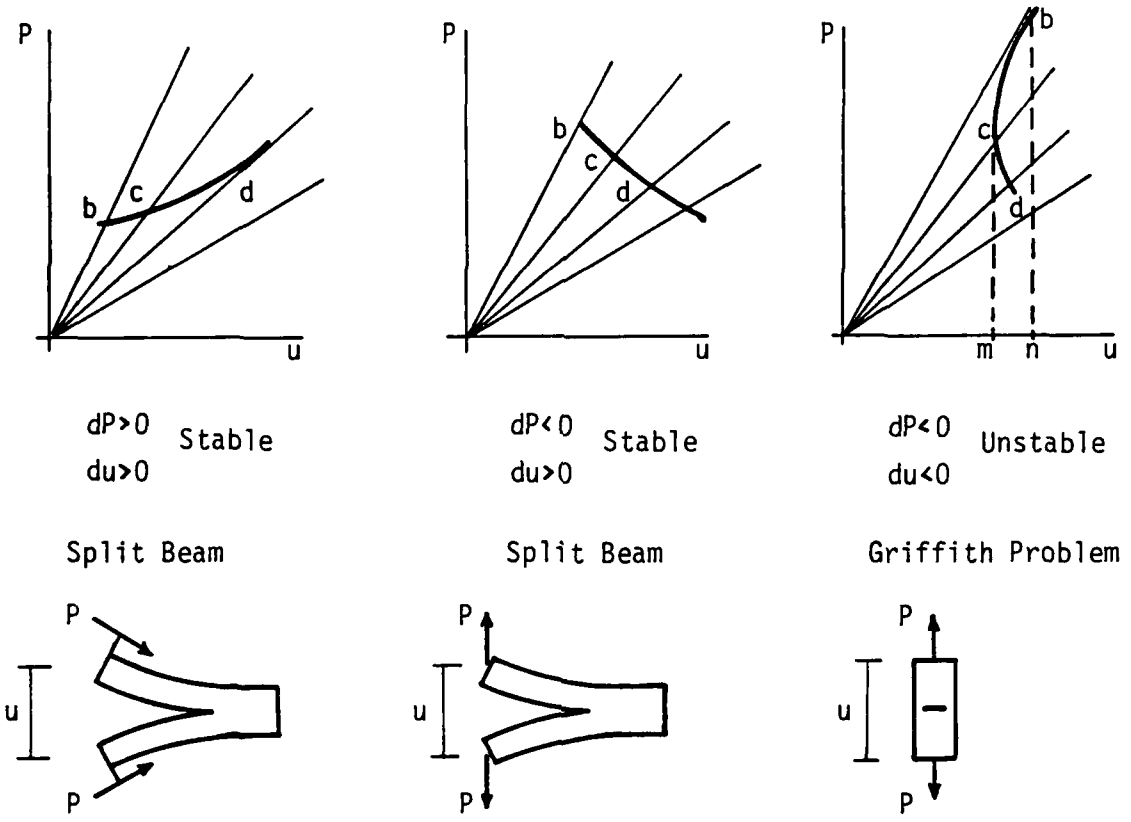

Fig. 2-5 Stability of crack propagation. Stable and unstable crack control of hardening and weakening problems.

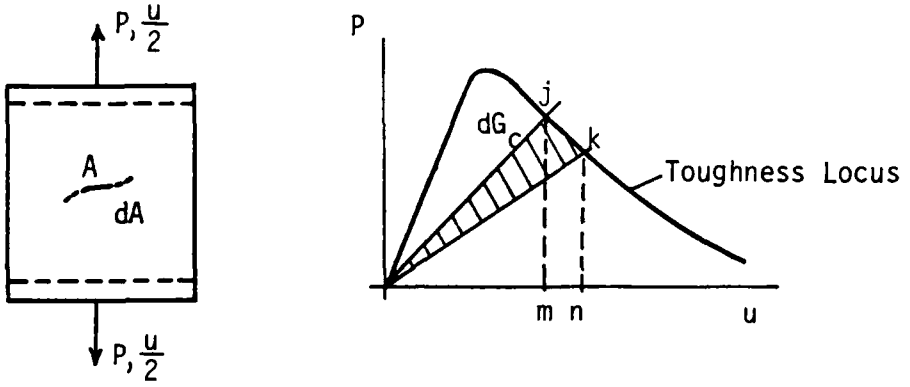

$$2G_c = \int_A P^2 \frac{d}{dA}\left(\frac{u}{P}\right) \qquad G_c \sim \int_{u_r} \sigma_z(u)\, du$$

Fig. 2-6 Fracture energy content in direct tension test for stable crack propagation under displacement control.

$$G_c = \int_0^{u_r} \sigma_z(u)du \qquad (2.18)$$

If G_c is to be a true material property, then the energy consumption outside the crack band must remain negligible and the fracture energy must be independent of the specimen dimension. In other words, stable crack growth is localized entirely in a single fracture band and energy dissipation due to plastic work remains negligible. According to Petersson [4] interpretation of different tensile test results gives rise to typical values of the fracture energy for concrete and mortar in the order of

$$G_c = 55 \text{ to } 80 \text{ N/m} \qquad (2.19)$$

The fracture energy concept was originally utilized by Hillerborg et al. [10] in their "Fictitious Crack Model". This formulation is essentially a discrete fracture approach in which the progressive decohesion at the crack front is monitored according to the Barenblatt model in the form of a gradual decrease of tensile strength with increasing crack opening. Again, the underlying assumption is that the entire fracture process is confined to a single localized crack. Therefore, numerical fracture computations require a discrete crack idealization in which the decohesive interface behavior within the fictitious crack zone is controlled by the gradual release of the fracture energy G_c.

The basic concept of the fictitious crack model was extended by Bazant and Cedolin [28] in their development of the so-called "Crack

Band Model " for the fracture of concrete and geomaterials. In this case, the notion of discrete cracking was replaced by a fracture model within a localized crack band of finite width, in order to accommodate the fracture computations within a stationary finite element idealization which does not require remeshing. This concept goes back to the fundamental derivation of the J-integral by Rice [27] who studied the energy exchange for crack propagation in elastic solids.

An explicit form of the energy balance in Eq. 2.1 leads to the following statement of weak equilibrium

$$\int_V d\mathbf{u}^t \, \mathbf{p}_V \, dv + \int_S d\mathbf{u}^t \, \mathbf{p}_S \, ds = \int_V d\boldsymbol{\varepsilon}^t \, \boldsymbol{\sigma} \, dv + G_c \, dA \qquad (2.20)$$

The change of strains depends on both the change of displacements as well as the change of geometry at the crack front

$$d\boldsymbol{\varepsilon} = \frac{\partial \boldsymbol{\varepsilon}}{\partial \mathbf{u}} \, d\mathbf{u} + \frac{\partial \boldsymbol{\varepsilon}}{\partial A} \, dA \qquad (2.21)$$

For a small change of the crack configuration the equilibrium condition Eq. 2.20 reduces to

$$\int_V \frac{\partial \boldsymbol{\varepsilon}^t}{\partial A} \, \boldsymbol{\sigma} \, dv + G_c = 0 \qquad (2.22)$$

A comparison with the fracture stability condition Eq. 2.12 yields the following expression for the release of internal fracture energy

$$G = - \int_V \frac{\partial \boldsymbol{\varepsilon}^t}{\partial A} \, \boldsymbol{\sigma} \, dv \qquad (2.23)$$

Finite element expansion of the displacement field u yields the following change of strains $\boldsymbol{\varepsilon} = \mathbf{B}\mathbf{r}$ according to Eq. 2.21

$$d\boldsymbol{\varepsilon} = \mathbf{B}\, d\mathbf{r} + \frac{\partial \mathbf{B}}{\partial A}\mathbf{r}\, dA \tag{2.24}$$

As a result the fracture energy within the structure is simply the sum of all element contributions

$$G = -\mathbf{r}^t \int_V \frac{\partial \mathbf{B}^t}{\partial A}\boldsymbol{\sigma}\, dv \tag{2.25}$$

For linear elastic material behavior

$$\boldsymbol{\sigma} = \mathbf{E}\,\boldsymbol{\varepsilon} = \mathbf{E}\,\mathbf{B}\,\mathbf{r} \tag{2.26}$$

The fracture energy expression in Eq. 2.23 can now be interpreted as the elastic strain energy release rate

$$G_E = -\mathbf{r}^t \int_V \frac{\partial \mathbf{B}^t}{\partial A}\,\mathbf{E}\,\mathbf{B}\, dv\,\mathbf{r} \sim -\frac{1}{2}\mathbf{r}^t \frac{d\mathbf{K}_E}{dA}\mathbf{r} \tag{2.27}$$

whereby $d\mathbf{K}_E$ designates in our notation the symmetric part of the change of the elastic stiffness due to the change of crack surface area dA. We recall that the elastic strain energy release rate in Eq. 2.27 corresponds to the change of potential energy due to a small crack extension if the external loading R=const. and is not affected by fracture propagation. Therefore, evaluating the total potential energy of the structure before,

$$\Pi(u,A) = \frac{1}{2}\mathbf{r}^t \mathbf{K}_E\,\mathbf{r} - \mathbf{r}^t\,\mathbf{R} \tag{2.28}$$

and after crack extension by dA, the difference between the two potential energy expressions recovers Eq. 2.27 if we use $\mathbf{K}_E\mathbf{r}=\mathbf{R}$ and neglect higher order terms such as $d\mathbf{K}d\mathbf{r}$

$$d\Pi = \Pi(\mathbf{u},A+dA) - \Pi(\mathbf{u},A) = \frac{1}{2}\,\mathbf{r}^t\, d\mathbf{K}_E\mathbf{r} = -G_E \qquad (2.29)$$

This result of Parks [30] corresponds to that of first order perturbation analysis of the structural stiffness with regard to the nodal coordinates, i.e. $\mathbf{K}\rightarrow\mathbf{K}+d\mathbf{K}$, which was established before in the context of structural modifications. Clearly, in the case of slow crack propagation these modifications are highly localized, i.e. only the elements in the immediate vicinity of the crack front contribute to the non-zero portion of $d\mathbf{K}_E$.

If we return to the original definition of the fracture energy release expression in Eq. 2.23, then the finite element discretization leads to the following format of the internal fracture release forces $\mathbf{P}_f$ due to change of the crack geometry.

$$d\mathbf{P}_f = \int_V \frac{\partial \mathbf{B}^t}{\partial A}\,\boldsymbol{\sigma}\, dv \quad \text{where } G = -\,\mathbf{r}^t d\mathbf{P}_f \qquad (2.30)$$

It was noted only recently by Doltsinis [31] that the integral in Eq. 2.30 gives rise to a geometric stiffness which reflects the effect of internal stress due to a change of the nodal geometry $d\mathbf{x}\rightarrow d\mathbf{x}/dA$.

$$d\mathbf{P}_f = \mathbf{K}_g^x\, d\mathbf{x} \quad \text{where} \quad \mathbf{K}_g^x = \int_V \boldsymbol{\sigma}^t\, \frac{\partial \mathbf{B}}{\partial \mathbf{x}}\, dv \qquad (2.31)$$

The same effect is encountered if the mesh remains invariant during crack propagation and if only the finite element nodal connectivity is updated in a discontinuous fashion. In this case the geometric stiffness originates from the change of topology

$$\mathbf{K}_g^a = \int_v \boldsymbol{\sigma}^t \frac{\partial \mathbf{B}}{\partial \mathbf{a}} \, dv \tag{2.32}$$

where $\mathbf{a}$ denotes the nodal incidence map. In both cases the internal fracture release force $d\mathbf{P}_f$ and consequently the internal fracture energy release rate G are independent of a particular material formulation. Thus they are more general than the first order elastic approximation in Eq. 2.27 since they apply to elastic as well as inelastic material behavior. Moreover, the fracture release forces provide a simple analogy between the discrete and the smeared fracture approaches which is of particular interest to this investigation.

We recall that in the smeared fracture approach the topology of the structural idealization remains intact during crack propagation. The fracture energy release rate is in this case expressed in terms of a strain-softening stress-strain relation. Therefore, the internal fracture release force vector $d\mathbf{P}_s$ result from the decrease of internal stresses

$$d\mathbf{P}_s = \int_v \mathbf{B}^t \, d\boldsymbol{\sigma} \, dv \quad \text{with} \quad G_s = \mathbf{r}^t \, d\mathbf{P}_s \tag{2.33}$$

rather than from the change of crack geometry in Eq. 2.30. Clearly, if we could calibrate the strain-softening formulation in such a way that

$$\int_V \frac{\partial B^t}{\partial A}\,\sigma = \int_V B^t\, d\sigma\, dv \qquad (2.34)$$

the two fracture approaches would be completely equivalent. This is not a simple task since we usually resort to a strain-softening stress-strain relation along the line of

$$d\sigma = E_s\, d\epsilon = E_s\, B\, dr \qquad (2.35)$$

which gives rise to the softening stiffness

$$K_s = B^t\, E_s\, B\, dr \qquad (2.36)$$

The fracture energy release rate is then for the smeared fracture approach

$$G_s = r^t\, K_s\, dr \qquad (2.37)$$

which should be compared with G_E in Eq. 2.27 for the case of elastic fracture.

The discrete and the smeared fracture concepts are again equivalent if the internal fracture release forces coincide, i.e., if

$$-\frac{1}{2}\, dK_E\, r = K_s\, dr \qquad (2.38)$$

Previously, we observed that the discrete fracture approach leads to highly localized changes of the elastic stiffness K_E because of the changes at the crack front. In contrast the softening stiffness K_s in the smeared approach is not confined at all to any particular region

except for the loading condition on the constitutive level which introduces an implicit localization according to the total strain space control. It is exactly for this reason that Bazant and Cedolin introduced the blunt crack band model [28] within their smeared fracture formulation in order to confine the fracture energy release G_s within a fracture band of predefined width. This restriction of the smeared fracture approach is entirely consistent with the usual G_c interpretation of fracture mechanics test data from notched specimens when fracture is assumed to take place in a single crack or shear band. However, it also infers that the computational fracture predictions in a structure are confined to a single predominant crack very much along the line of the discrete crack approach.

In our view this geometric restriction is against the spirit of the smeared fracture approach where cracking and shearing can take place in a distributed manner according to the implicit strain-softening control of the constitutive model. It is exactly this point of distributed fracture which will be addressed in Sections 4 and 5 where a consistent approach will be developed for the interpretation of displacement controlled fracture data of unnotched specimens with the aid of inverse identification of a composite damage formulation. In this context we will resort to the so-called initial load approach where the elastic stiffness is not updated at all and the fracture energy release due to strain-softening is accommodated entirely by the internal fracture release forces dP_s in Eq. 2.33.

3. EXPERIMENTAL PROGRAM

3.1 Introductory Remarks

The following sections describe the laboratory experiments that were performed to identify material parameters for the computational model. These tests also include a miniature structure which served as a benchmark for the verification of computational predictions.

The basic concrete behavior was investigated in a series of triaxial and uniaxial compression and tension experiments conducted on cylindrical and prismatic specimens. Material properties such as unconfined compressive and tensile strength, peak and residual strength friction angles, cohesion, and elastic moduli were derived from these tests.

Direct shear experiments on prismatic specimens of plain concrete were conducted in a large capacity servo-controlled and structurally stiff test apparatus in order to assess the predictive capabilities of the nonlinear computational analysis techniques. The objective in these experiments was not to obtain material properties but rather to investigate load-deformation response behavior and strength characteristics of a mini-structure subjected to the complex states of non-proportional loading imposed by the direct shear test. The specimens were loaded to failure under displacement control and constant normal load. The complete spectrum of structure as well as material responses were observed including pre-peak elastic-plastic hardening, post-peak strength softening, localization and deformation into a shear band, and continued shear gliding at a residual strength level.

3.2 Triaxial Hoek Cell Experiments

Conventional axisymmetric triaxial compression experiments were conducted at different confining stress levels in a University of Colorado Hoek cell, which receives a 5.40 cm (2.125 in.) diameter and approximately 11.43 cm (4.5 in.) long cylindrical specimen. The Hoek cell, which is illustrated in Fig. 3-1, has a confining pressure capacity of 69 MPa (10,000 psi) and has instrumentation for measuring lateral nominal strain. The pressure is provided by hydraulic fluid generated by a manually operated and stable pressure supply. The pressure is transmitted to the specimen by flexible adiprene or polyurethane membranes. These membranes are neither mechanically clamped to the specimen nor the moving loading ram but are firmly located in the end caps of the cell by means of self-sealing flanges, as illustrated in Fig. 3-1. This membrane configuration avoids warping of the membrane's cylindrical shell portion during loading, and it also allows for extension modes of deformation without rupturing the pressure seals. The confining stress has no component in the axial direction of the cylindrical specimen as shown in Fig. 3-1. The axial load was measured in this test program by an internal load cell located within the MTS loading system consisting of a Standard 490 kN (110 kip) MTS load frame with servo controller and function generator units. The experiments were carried out in order to obtain confined as well as unconfined compression strength properties, elastic moduli and their respective ratios.

The test results were also used to investigate brittle-ductile behavior of the concrete as well as the strain-softening response and

residual strength characteristics as a function of confining stress levels. The experiments were carried out at constant confining stress states of 0, 345 kPa (50 psi), 690 kPa (100 psi), 1725 kPa (250 psi), and 3450 kPa (500 psi), while the axial displacement was increased monotonically at a constant rate of 0.106 mm/sec. Unloading and reloading sequences were in some instances carried out in order to precisely assess modulus values. All triaxial specimens were obtained by NX-size (2-1/8 in. dia.) coring of the large prismatic concrete specimens used for the direct shear experiments (described subsequently), and all specimens were from the same concrete batch mixture. The concrete was intentionally made weak and soft so that the model structures could be brought to failure in our available laboratory apparatus.

Great care was exercised to ensure that the end surfaces of the specimens were parallel and smooth. No lubrication was provided between the polished steel loading platens and the specimen ends. The lateral or radial displacements were recorded in some of the tests in order to evaluate Poisson's ratio. The radial measurements were made at the mid-height of the specimens with strain-gaged cantilevers. The results from 6 such cantilevers, spaced at 60° intervals about the circumference of the specimen, provided an average lateral displacement, which in turn was converted into radial strain (Fig. 3-2). The axial displacement was measured by an LVDT. Continuous real-time load-displacement diagrams were produced by an x-y-y' recorder.

3.2.1 Experimental Results

Typical nominal stress-nominal strain response curves are shown in Figs. 3-3 and 3-4. Figure 3-3 contains three sets of test results that

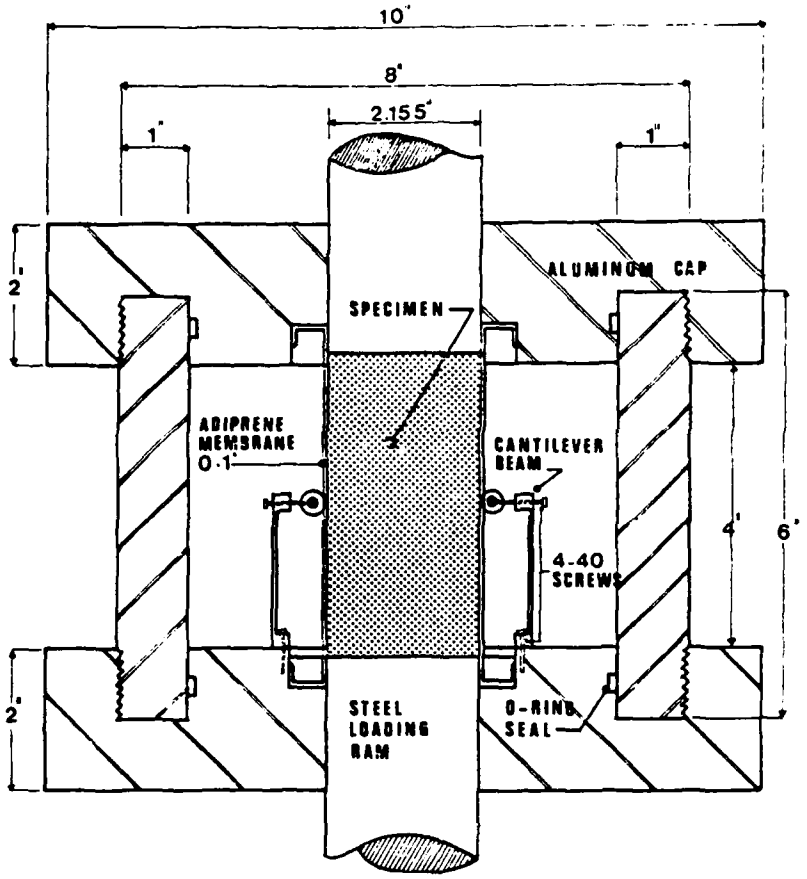

Fig. 3-1 Modified Triaxial Hoek Cell. Cross-section view of cell and specimen.

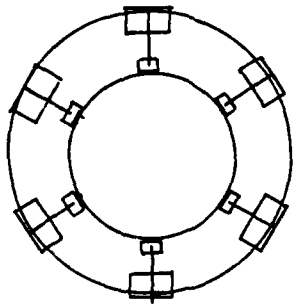

Fig. 3-2 Modified Triaxial Hoek Cell. Top view of apparatus showing radial displacement measuring cantilever positions.

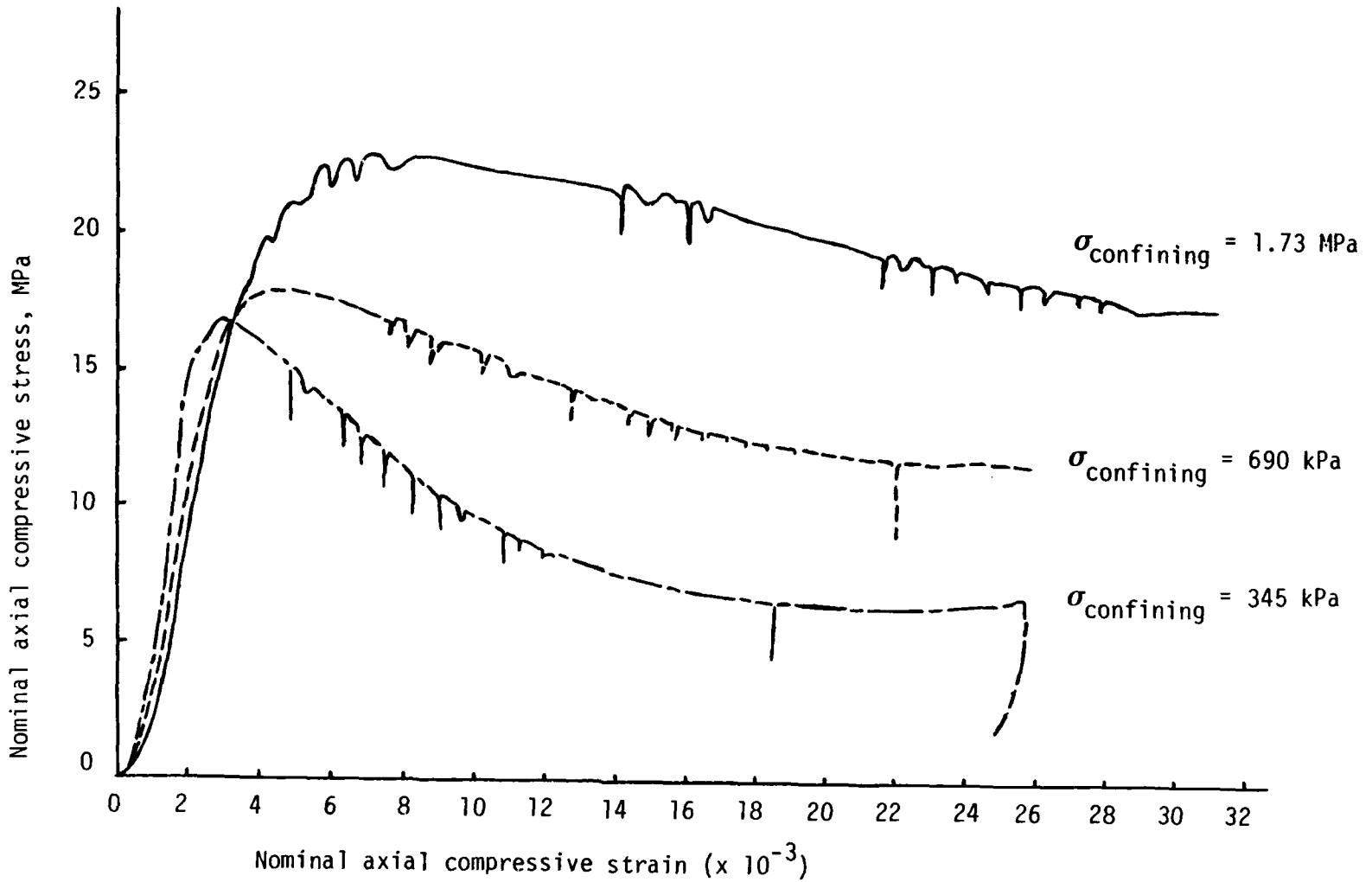

Fig. 3-3 Stress-strain response curves for concrete. Nominal axial strain vs. nominal axial stress traces are described.

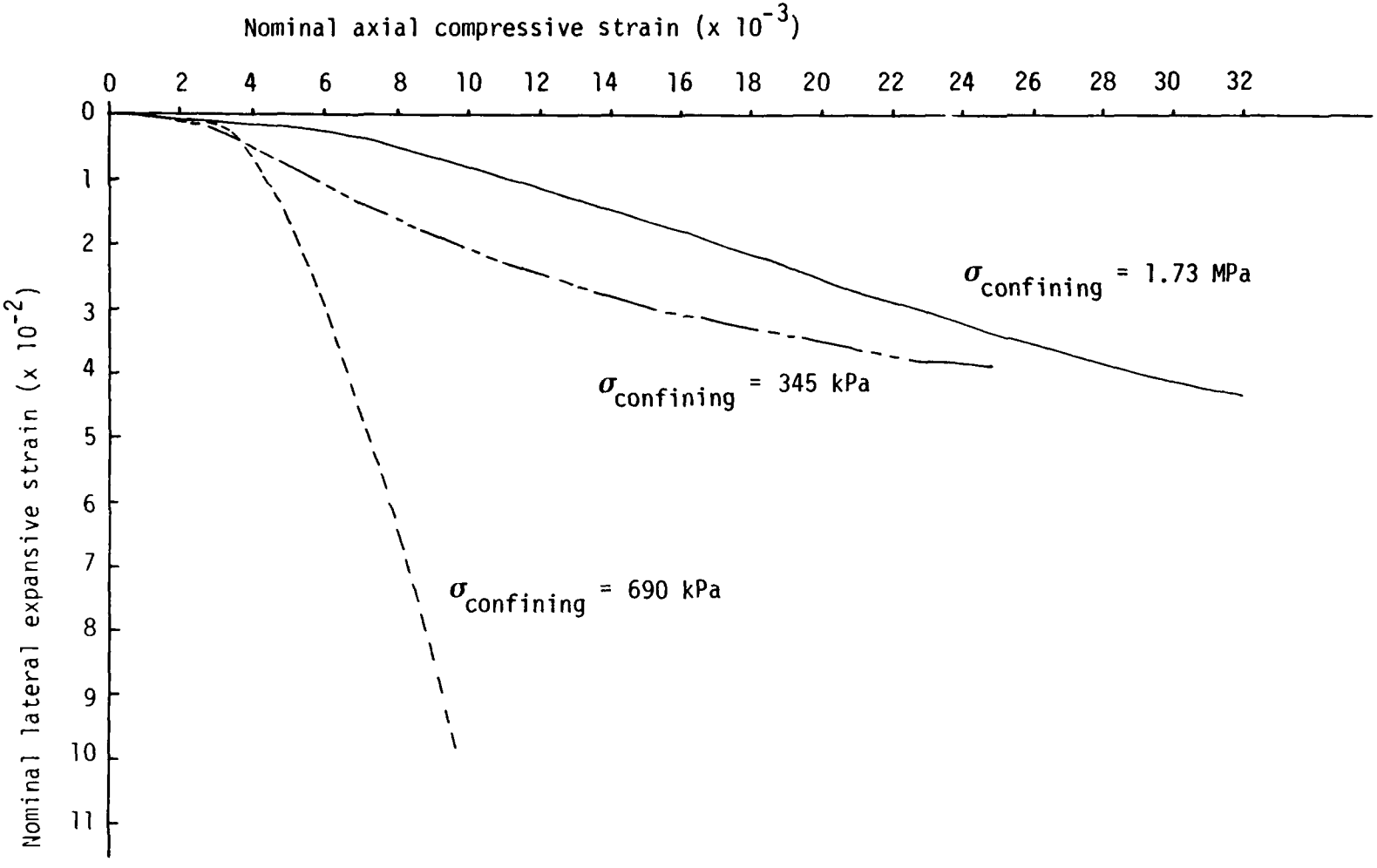

Fig. 3-3 (continued)

were obtained at an early stage of the test program. The concrete was approximately 4 weeks old. Lateral as well as axial nominal strains are shown vs. axial nominal stress. Young's modulus was found to vary between 6.76 and 8.28 GPa (980 and 1,200 ksi) and Poisson's ratio was determined to be 0.2. An equal isotropic confining stress state was applied to the specimens prior to application of the axial deviator stress, and the initial isotropic compressive volumetric strain response is shown in nearly all the stress-strain traces except for the uniaxial test. Excessive rebound upon unloading in the axial direction below the confining cell pressure level for the 1.73 MPa test can be attributed to membrane penetration between specimen and axial loading ram. The pronounced difference in elastic behavior was attributed to heterogeneity in the weak and soft concrete mixture. Although the specimens were sufficiently large in relation to the maximum aggregate size, it is believed that the wet and high slump concrete resulted in nonuniform properties not observed in normal strength concrete. Figure 3-4 shows five sets of test results that were obtained at the end of the test program, and the concrete was at that stage approximately 6 months old. Young's modulus was in this instance found to vary between 6.00 and 8.28 GPa (870 and 1,200 ksi). The lateral nominal strain traces shown in Fig. 3-3 reveal highly dilatant behavior at the onset of fracture in the concrete, and the expansion that took place as a result of the rubblization and bulking exceeded volumetric strain values that are normally observed during shearing of dense cohesionless soils and many rocks. Post-experiment analyses of the specimens showed

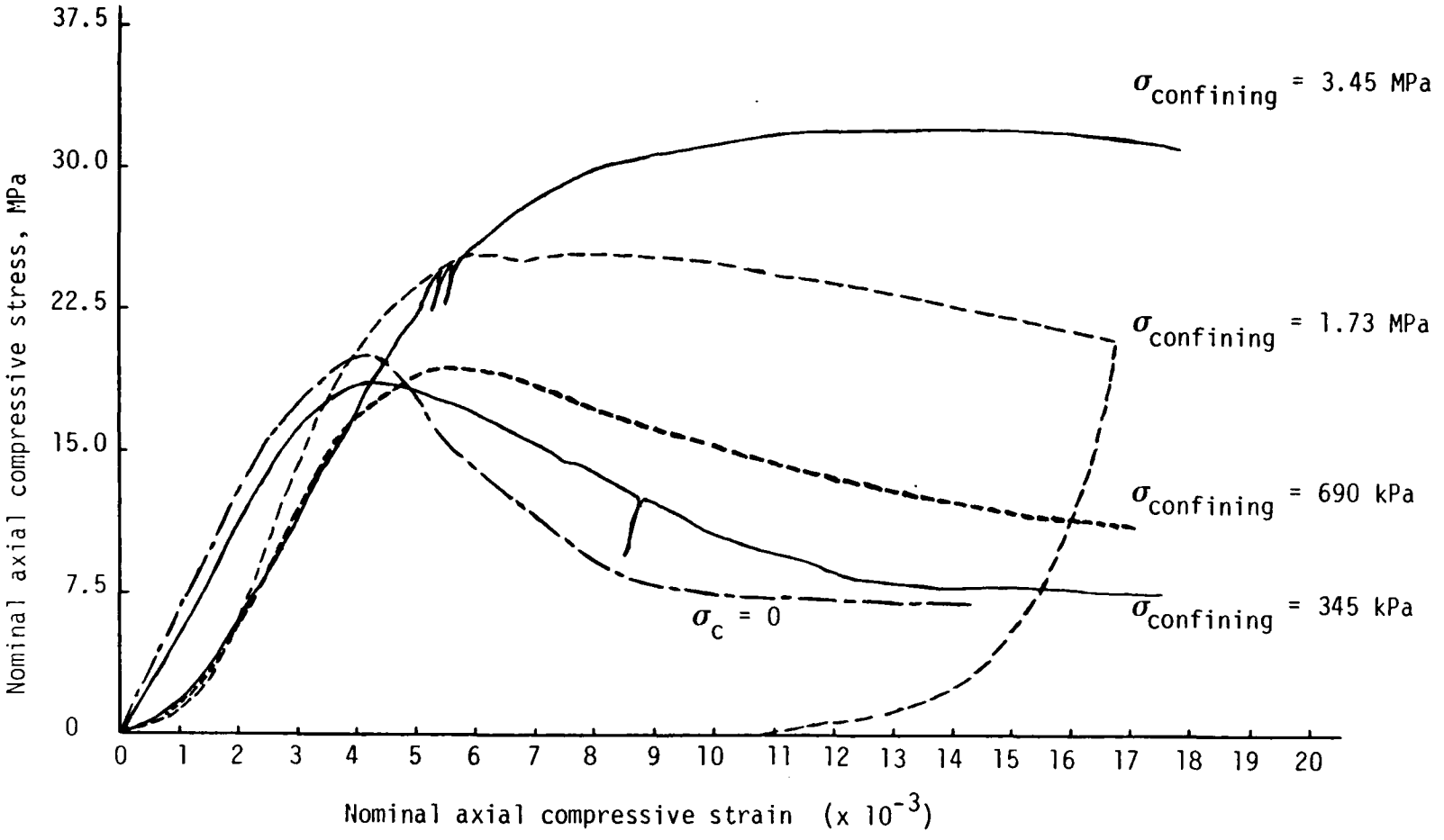

Fig. 3- 4 Stress-strain response curves for concrete. Nominal axial stress vs. nominal axial strain.

pronounced shear fracture with a wide shear band, where cement matrix and aggregate clasts were as large as 0.25 cm (0.1 in.). Tendencies toward a tensile splitting fracture mode of failure were often observed near the specimen ends, and the irregularities in the nominal stress-strain responses near peak strength can be attributed to these occurrences. Shear fracture and subsequent shear gliding motion dominated the behavior at the post-peak strength stage, and strain-softening seemed to be entirely controlled by shear. The transition between pre-peak and post-peak behavior was relatively smooth in all cases. The nominal stress-strain traces for the low confining stress levels exhibit the steepest decending slopes and the transition to the residual strength level was also easy to observe for these tests. Ductility increased in the strain-softening regime as the confining stress inreased and the transition to the residual strength level was also less abrupt. The nature of the fractured material in the shear band often gave an indication of the mean normal stress level during the shearing motion. Relatively large amounts of fines made up the clastic mass at higher confining stress levels whereas several irregularly shaped aggregate-cement matrix pieces having average sizes similar to that of the largest aggregate, were found in the shear zone of the low confining test specimens.

3.3 Direct Shear Experiments

The direct shear translation test has been used in the past often rather indiscriminately to evaluate basic strength properties as well as shear stress-shear displacement response behavior of concrete and geo-

materials. It has generally been assumed that the normal and shear stresses were uniformly distributed on the imposed shear plane. However, it is well established that both strain and stress distributions within initially homogeneous solid test samples were highly nonuniform during the experiment. The magnitude of the principal stress varies nonproportionally in the specimen, and the principal stress directions rotate with respect to the material fabric to unknown extents during the shearing process, resulting in pronounced stress or deformation induced anisotropy. The overall sample response behavior therefore constitutes a combined response of a material that undergoes brittle and ductile fracture in tension and shear gliding. Proper material characterization for the purpose of obtaining basic engineering properties require homogeneous strain and stress states in the test specimen, and these do not exist in the direct shear tests. This test is also highly sensitive to boundary conditions and the manner with which a centric or non-centric tangential shear load is applied with respect to the shear plane. Several authors have discussed the merits of the direct shear test, such as Morgenstern and Tchalenko, [32]; Kutter, [33]; Mandl, De Jong, and Maltha, [34]; Vallejo, [35]; Walters and Thomas [36]. The shear test has been found to be a valuable tool for investigating residual strength characteristics of materials where shear bands or fracture zones already exist. It has also seen successful use for studying interface behavior between soils and structural materials such as steel and concrete. This aspect has been reviewed by Desai and Zaman [37].

In view of these considerations it was decided to adopt the direct

shear test, not as a test for engineering properties, but as a miniature structure test where the boundary conditions can be carefully controlled and where complex states of tensile cracking and shear fracture can be studied. The direct shear structure test constitutes a controlled environment where the entire spectrum of the structure's and its material's responses can be followed through the elastic, hardening plastic, fracture, post-peak, strain-softening, and residual strength states. Investigations of brittle and ductile fracture transitions, progressive damage accumulation and localization of deformation in narrow shear bands in conjunction with degrading stress-strain or load-displacement relationships require a very stable test system.

The general objective in this facet of the research effort was to compare the measured response behavior to the computational predictions and to evaluate the capability of the so-called smeared fracture approach for describing progressive damage and frictional sliding along narrow shear bands. If this could be achieved in the complex environment of the direct shear test, it was asserted that the computational analysis algorithm could model almost any three-dimensional boundary value problem involving brittle and ductile materials. The following sections cover apparatus description and the experimental technique used.

3.3.1 Experimental Apparatus

The experiments were conducted in the high precision direct shear device shown in Fig. 3-5. The apparatus consists of loading actuators, normal and shear load reaction frames, normal and lateral loading

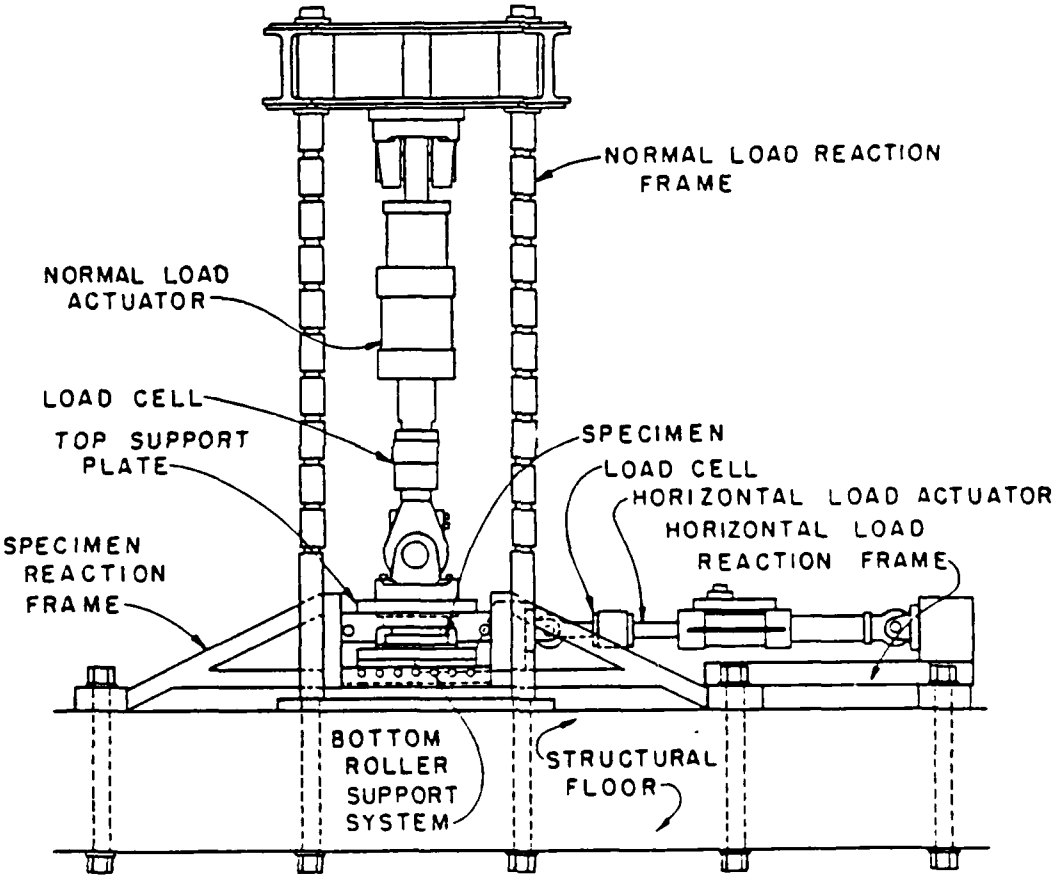

Fig. 3-5 Direct shear apparatus. Side view of shear device and support system.

fixtures also shown in Fig. 3-6. The top and bottom shear box compartments shown in Fig. 3-7 receive 20.3 x 20.3 x 11.4 cm (8 x 8 x 4.5 in.) samples of prismatic shape. In some instances the specimen width was as small as 10.2 cm rather than 20.3 cm. The notched and un-notched specimens were fused to the shear box compartments by means of structural epoxy and conventional sulphur capping compound. In order to minimize a reactive moment about the average shear plane the shear box was positioned in the holding fixtures and apparatus support system so that the applied lateral shear load and restraining action laid in the plane of induced shear failure. The top shear box compartment and holding fixture were restrained in the horizontal direction during shearing, while they were free to translate vertically. This feature facilities observation of dilatancy. The restraining action in the horizontal direction was provided by means of a very stiff horizontal load support frame, which in turn was connected to an extremely stiff structural floor by means by heavy bolts. The top holding fixture together with the top shear box compartment could also undergo small roll and pitch movements in addition to the vertical translation. Only one average vertical displacement was monitored by means of a Linear Variable Differential Transformer (LVDT). It is planned to use three LVDTs at a later stage in order to define the rotational movements of the top portion of the specimen during and after fracture. It is also possible to lock the top entirely against rotations as well as vertical translation. The latter can be achieved through displacement control of the vertical actuator and by fixing the swivel head. Servo-controlled

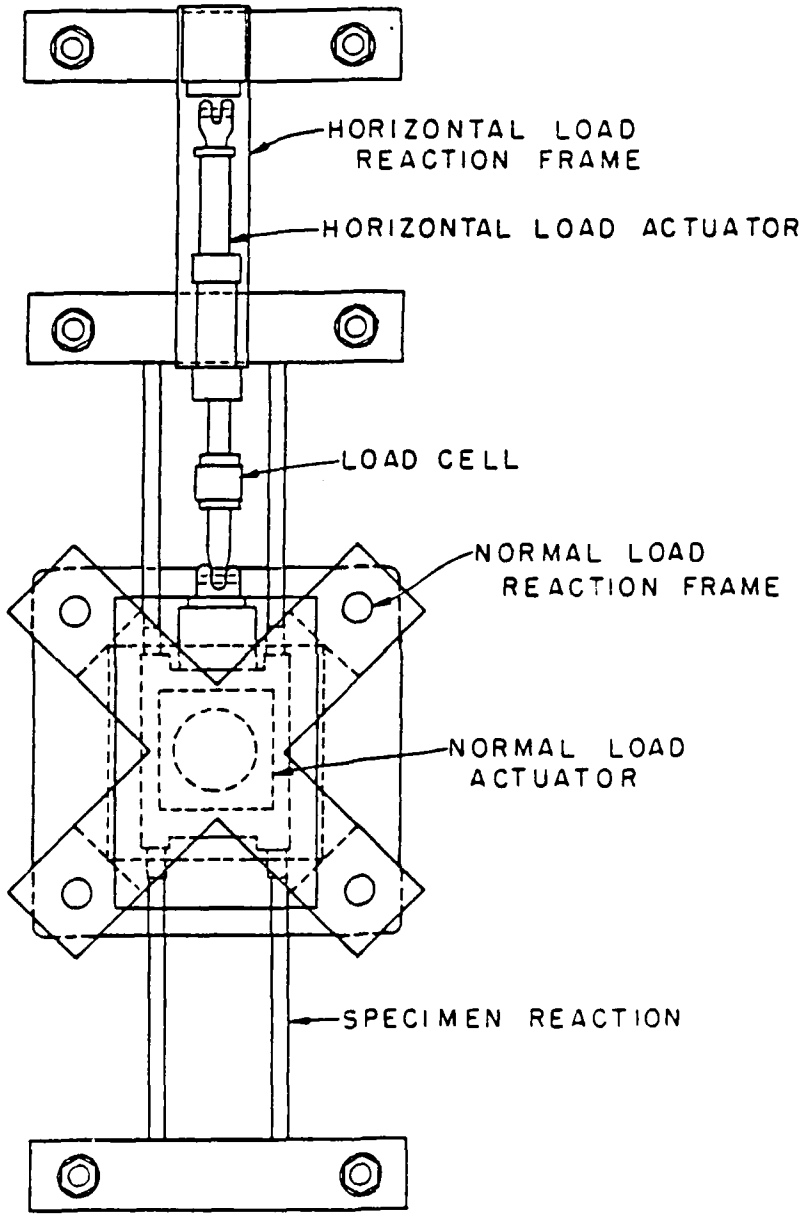

Fig. 3-6 Direct shear apparatus. Top view of shear device and support system.

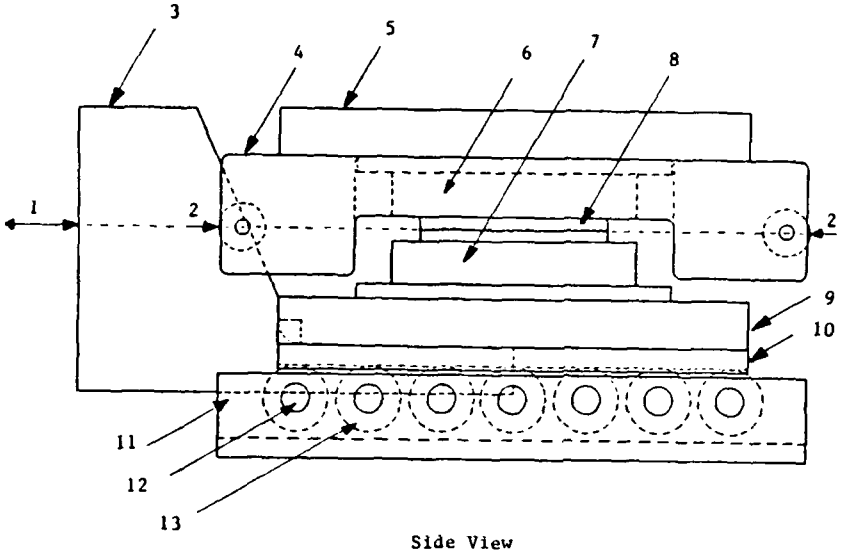

Side View

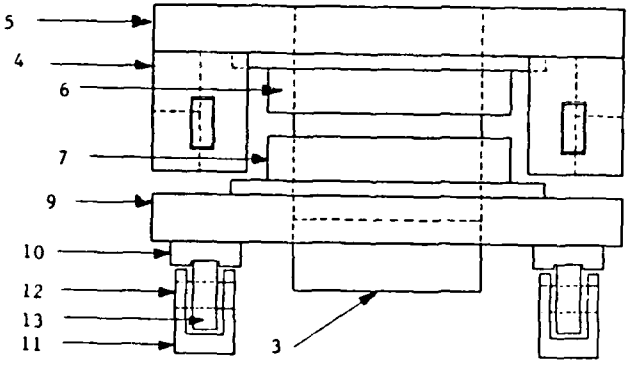

Front View

1 - Applied shear load

2 - Reaction frame load

3 - Shear load transmitting block

4 - Top reaction frame

5 - Top support plate

6 - Upper specimen shear box compartment

7 - Lower specimen shear box compartment

8 - Specimen

9 - Bottom support plate

10 - Roller bearing support guides

11 - Channel housing

12 - Support pins

13 - Roller bearings

Fig. 3-7 Specimen holding fixtures and shear box compartments for the direct shear apparatus

hydraulic MTS-actuators having 735 kN (165 kip) capacity in the normal direction and 156 kN (35 kip) in the tangential direction were used. The bottom shear box compartment and holding fixture had shapes and stiffness properties that were similar to the top components. The bottom shear holding fixture was supported by two rows of heavy roller bearings which allowed translatory motion of several centimeters. The bottom holding fixture was connected to the tangential load actuator by means of a large and stiff load transfer block (Fig. 3-6). The MTS control system can operate the apparatus under very slow or high displacement rates. Figure 3-8 shows a schematic illustration of the MTS and apparatus control system. The two MTS hydraulic actuators were operated independently in separate closed-loop control systems. The Series 204 MTS actuators were equipped with Series 252 servo-valves; Series 661 fatigue-resistent load cells; internal LVDT's; and swivel heads and bases. The control console was equipped with the following components: 430 digital indicator, 436 control unit, 410 digital function generator, and two 406 controllers, which were operated independently. Prior to testing a selection of force or displacement control for each 406 controller were made. Once the mode for operation has been decided, the proper feed-back signal provided by the internal LVDT or load cell was compared with the input signal. If the signals were not equivalent, action was taken by the servo-value to equilibrate the two signals. This is the basic feature of a closed-loop system.

A Hewlett-Packard 3054 A Automatic Data Acquisition/Control System controlled by a HP 9825 T desk top computer was used as the primary

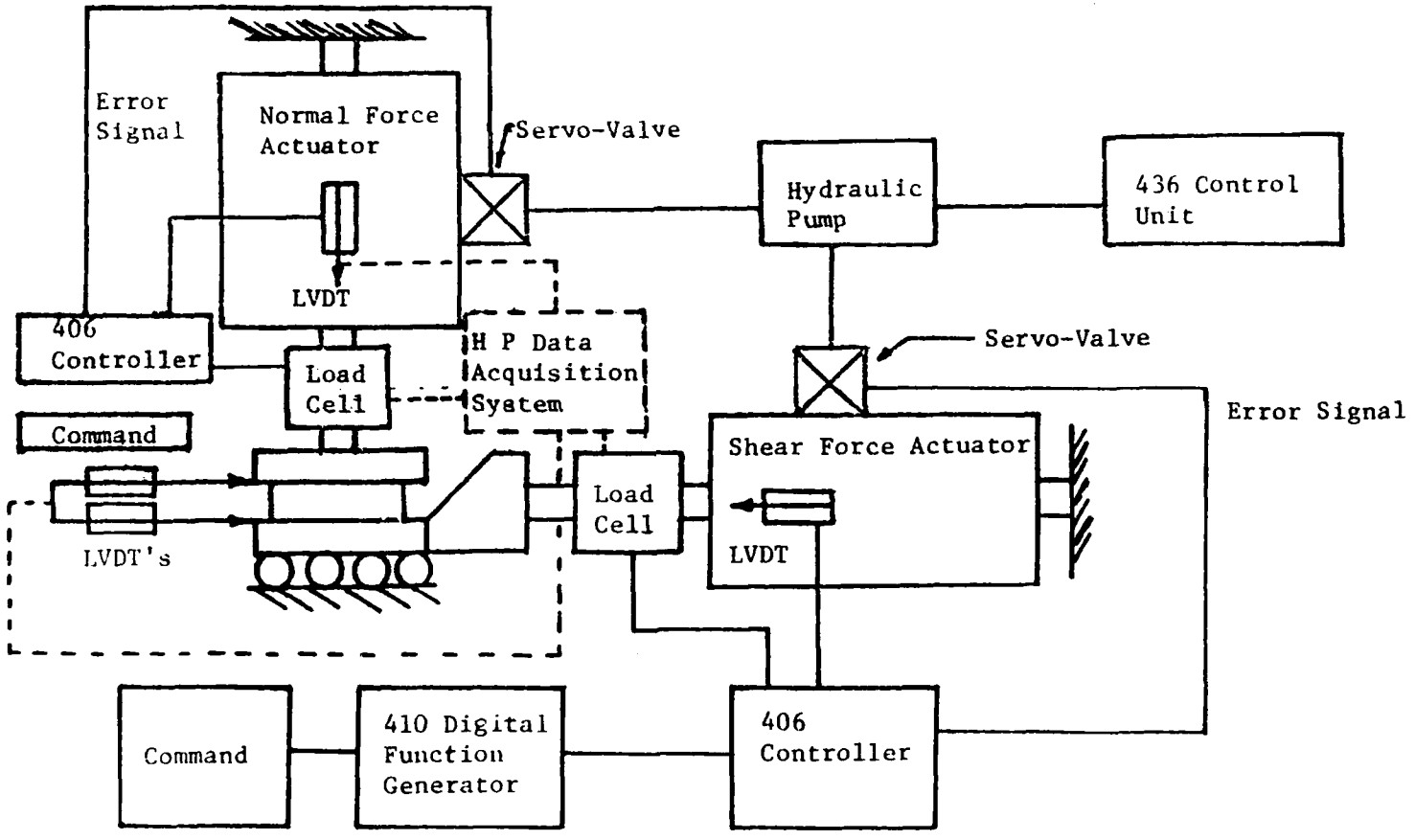

Fig. 3-8 Schematic illustration of direct shear apparatus and control system.

control and data acquisition system. The 3054 A system contains a HP 3437 A System high speed voltmeter and a HP 3497 A Data unit scanner. The data collected by the HP 3054 A system were transmitted to the HP 9825 T computer and stored on tape. Real-time observations of load-deformation and strength behavior was recorded by means of an Esterline Angus x-y' 540 plotter. The relative shear displacement was measured by means of two 500HR-DC Schaevitz LVDTs whose feeler rods were inserted into the sample as depicted in Fig. 3-9. The LVDTs were connected in series.

3.3.2 Experimental Technique and Results

Notched and un-notched plain concrete prismatic specimens having unconfined compressive strengths (f'_c) ranging from 21 MPa to 28 MPa and unconfined tensile strengths (f'_t) ranging from 0.8 MPa to 1.1 MPa were initially subjected to nominal normal stress states that varied between 0.69 MPa and 6.9 MPa (100-1000 psi) prior to shearing. The lateral load was increased in displacement control at a constant rate of 0.05 mm/s. The notched and un-notched specimens' widths varied between 10.2 cm and 20.4 cm (4-8 in.), while lengths and heights were maintained constant at 20.4 cm and 11.4 cm in all tests. All specimens were sawcut to final size from over-size castings. The exterior side faces of the specimens were exposed for visual and photographic observation.Shear displacement measurements were obtained by LVDTs mounted on control rods which were initially embedded in the specimen through ports in the top and bottom shear box compartments but later were attached to the exterior top and bottom base platens of the specimen shear box

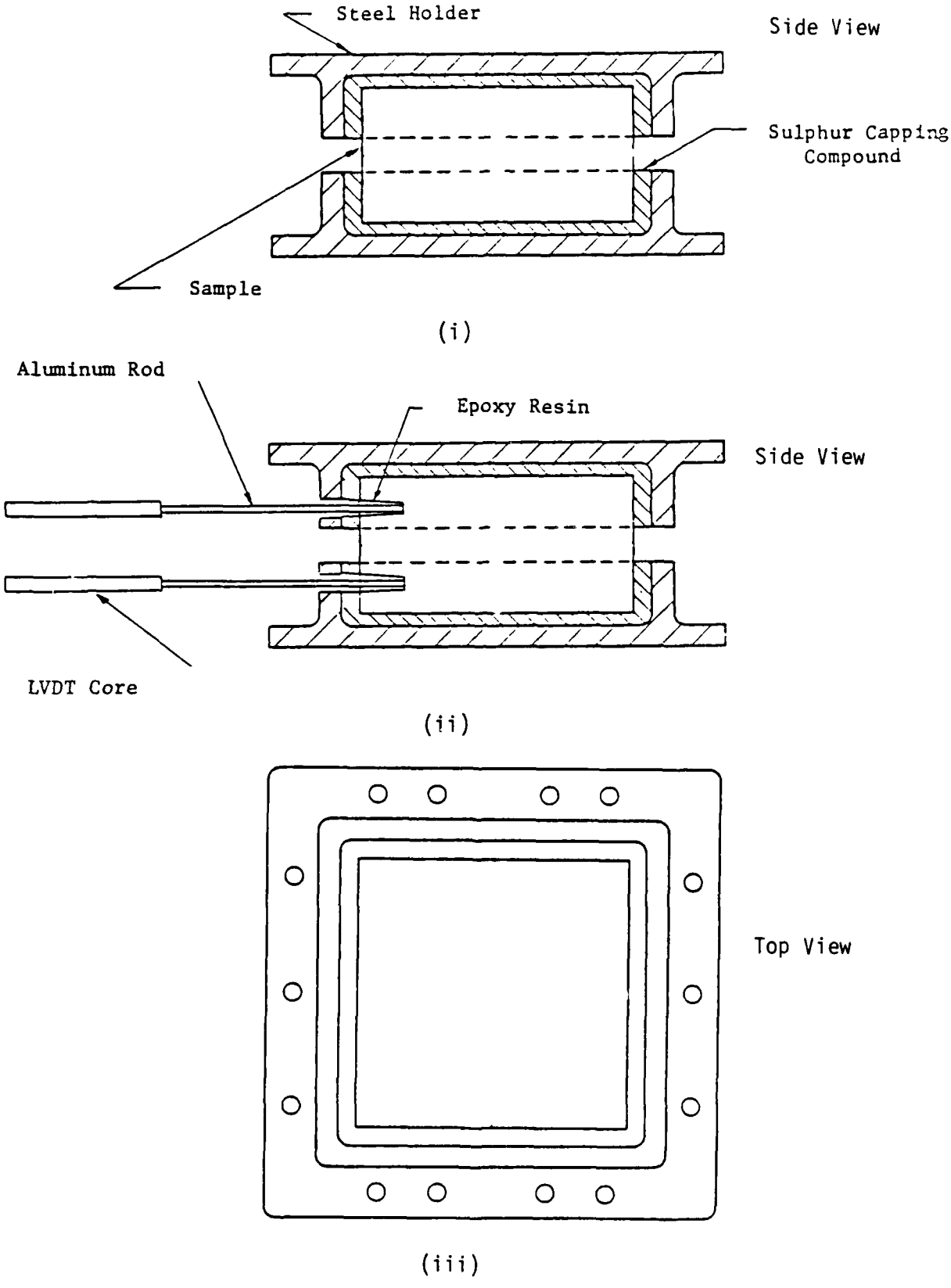

Fig. 3-9a Configuration of shear box compartments for wide specimens, (i, iii) and location of relative displacement LVDT feeler rods in early experiments (ii).

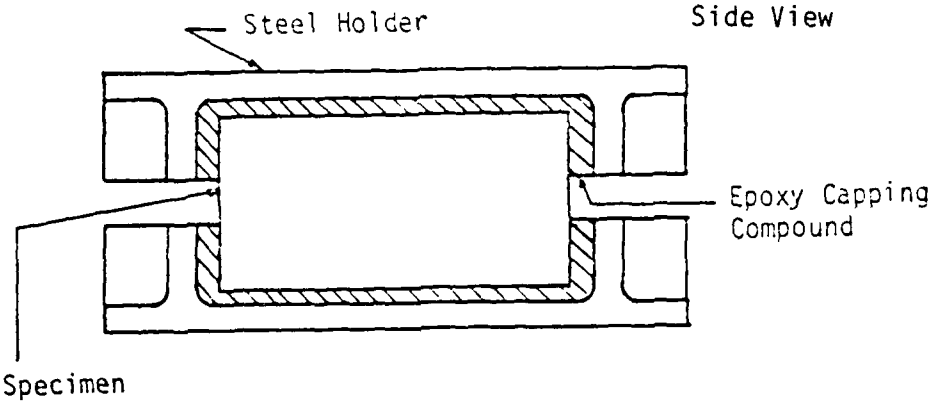

(iv)

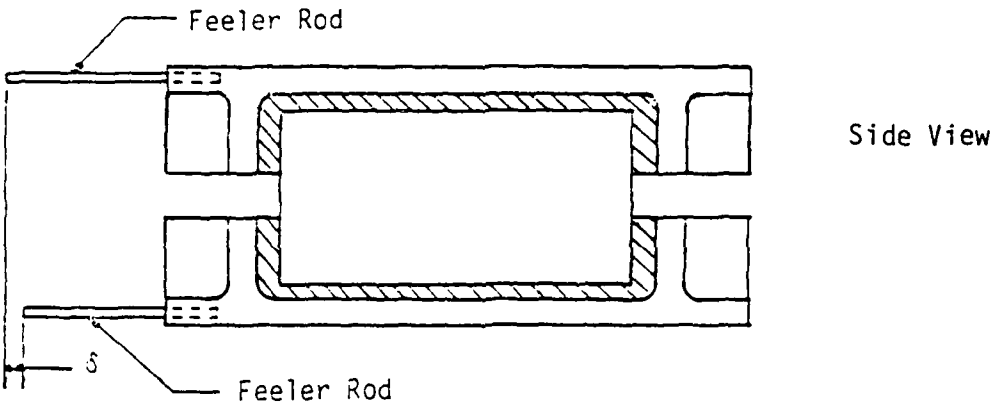

(v)

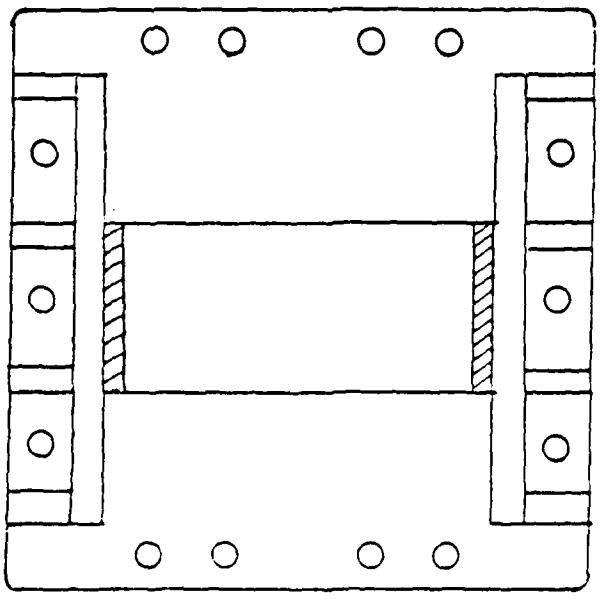

(vi)

Fig. 3-9b Configuration of shear box compartments for narrow specimens, (iv, vi) and location of relative displacement LVDT feeler rods in later experiments (v).

compartments, illustrated in Fig. 3.9. The spacing between the parallel rods thus varied between 3.8 cm and 13.5 cm in the tests. On one occasion the rods penetrated into the tensile fracture zone. Figure 3.9 also shows the notched and un-notched specimens within the shear box compartments. Notched shear specimens were considered during the initial phase of the investigation, and the specimens were notched at two opposite faces with 90° and 1.27 cm (0.5 in.) deep grooves in order to induce high stress concentrations near the ends.

Specimen failure initiated due to tensile cracking rather than shear slip in both the notched and un-notched tests. This happened before any shear band formation. Crack openings were visible before shear failure took place in the center regime. It is of interest to note that cracking took place outside the notches for these particular tests, and fracture propagation from the notch surfaces only took place after significant crack development. Pronounced inclined cleavage cracks later developed across the notched section. These crack development stages were also observed in the regularly shaped prismatic specimens. In both specimen categories the tensile stress state was responsible for ultimate failure, although the nominal compressive stress on the shear surface was much higher in the un-notched case. Tensile cracking occurred under very small relative displacements, while shear fracture and subsequent gliding took place under relatively large displacements. The shear fracture propagation was rather slow in comparison with the tensile cracking events.

No debonding was observed between specimens and shear box compart-

ments after the tests. All experiments exhibited nearly linear elastic behavior before reaching peak strength. The nonlinear shear stress-displacement response was most pronounced in the un-notched specimen. Upon continued shearing the lateral force decreased in the specimens until a residual strength level was reached. The rate of softening and the residual strength levels were quite different due to the large range in nominal normal stress levels applied to the specimens (690 kPa to 6.9 MPa). Figure 3-10 shows three nominal shear-relative displacement response curves that were conducted at the same 690 kPa nominal normal stress level. The comparison is quite good in both the pre-and post-peak strength regimes, and they all appear to converge to a similar residual strength level. One of the tests shows progressive fracture events involving one small brittle instability near peak strength and two major steeply inclined brittle softening traces that depart from the overall softening response. These events can possibly be attributed to aggregate and fracture zone interlock features in conjunction with stress redistributions. Otherwise, the experiments were quite reproducible. Figure 3-11 shows nominal shear stress-relative displacement response curves that were obtained for specimens subjected to various nominal normal stress levels ranging from 0.69 MPa to 6.9 MPa. It is apparent that the normal confining stress level in the shear specimen has a pronounced influence on response behavior. The ductility increases and the relative displacement required to reach the residual strength level increases. The residual strength level is raised with increasing normal pressure.

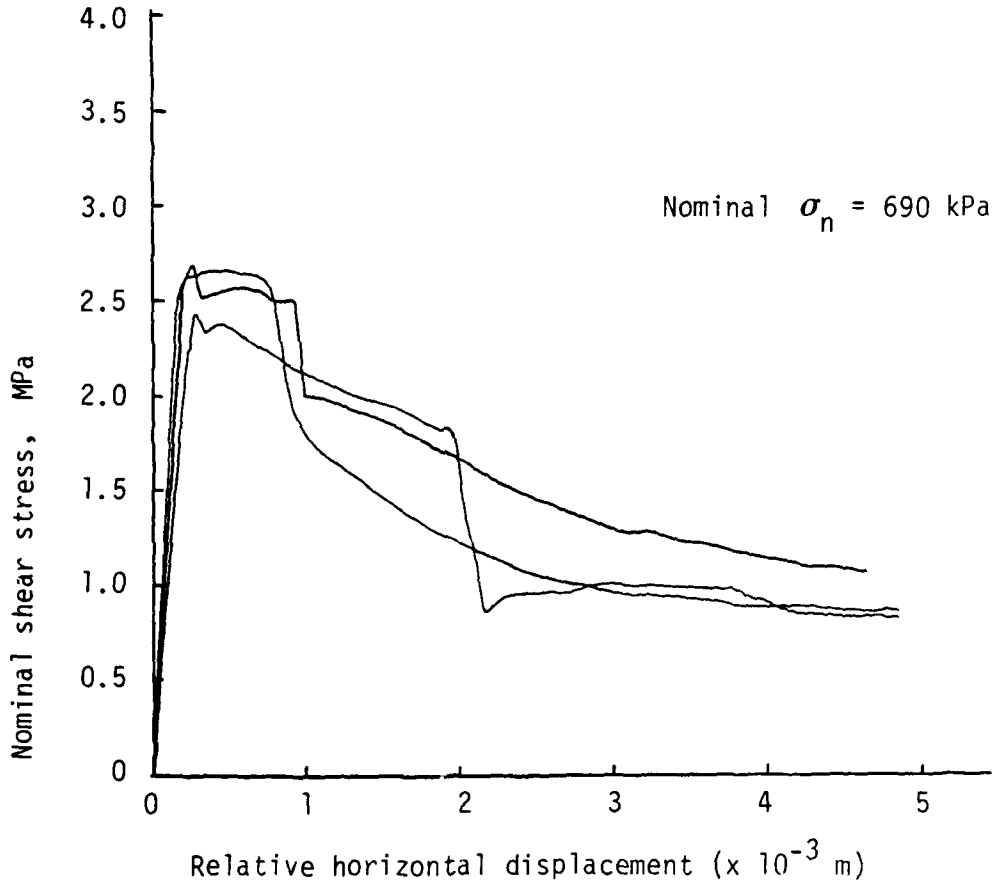

Fig. 3-10 Nominal shear stress-relative displacement response curves for concrete specimens in the direct shear apparatus.

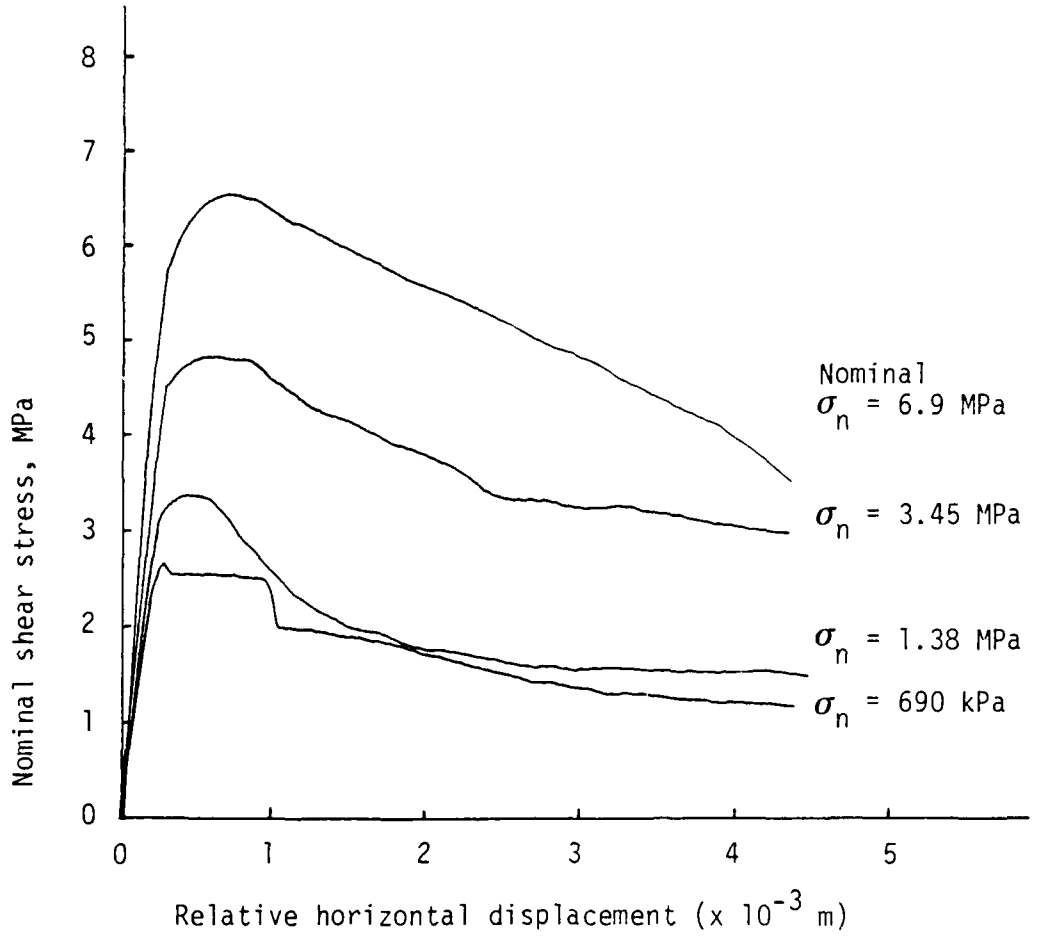

Fig. 3-11 Nominal shear stress-relative displacement response curves for concrete specimens in the direct shear apparatus.

During the 6.9 MPa experiment it was observed that the shear specimen's failure mode took on definite three-dimensional characteristics. Instead of forming a planar shear fracture surface through the thickness of the specimen, as occurred in the low normal stress level tests, the final failure surface was vee shaped as depicted in Fig. 3-12. The apparent implication is that high nominal normal stress levels relative to the material strength are not compatible with the plane strain assumption utilized in the associated computational modeling effort.

The residual friction angle ($\emptyset$) in all cases was found to be 35° with little or no residual cohesion.

Figure 3-13 shows typical nominal shear stress-relative displacement as well as vertical displacement response curves for a specimen which was subjected to a nominal normal stress of 1.38 MPa. The specimen initially compressed during the shearing motion and it subsequently dilated as shear fracture processes became dominant. Upon large relative displacement the specimen again appeared to compress as the clasts comprising fractured concrete mortar and aggregate pieces, underwent intense crushing and densification.

One specimen was sheared at a much higher displacement rate (8.5×10^{-4} m/sec.), and the nominal shear stress vs. relative displacement response curve is shown in Fig. 3-14. The behavior was quite similar to that observed in the earlier experiments, and thus negligible rate effects were encountered in this test.

The apparatus and test specimen configuration was essentially

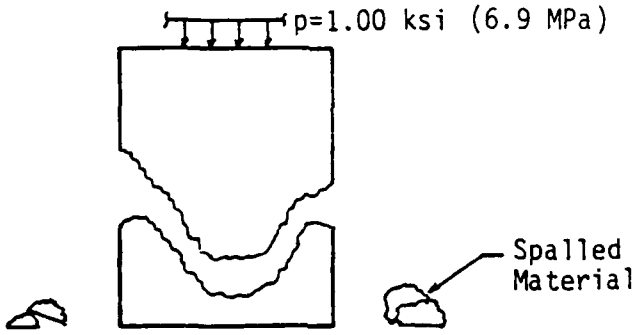

Cross Sectional Views

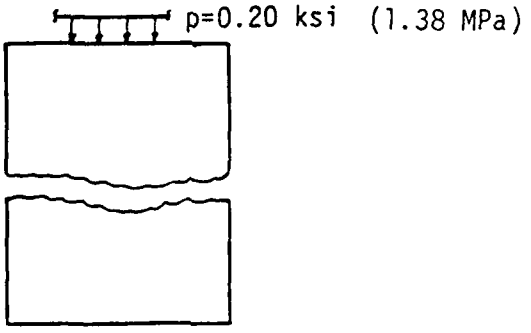

Fig. 3-12 Failure modes in the transverse direction in the direct shear experiments at high and low nominal normal stress levels.

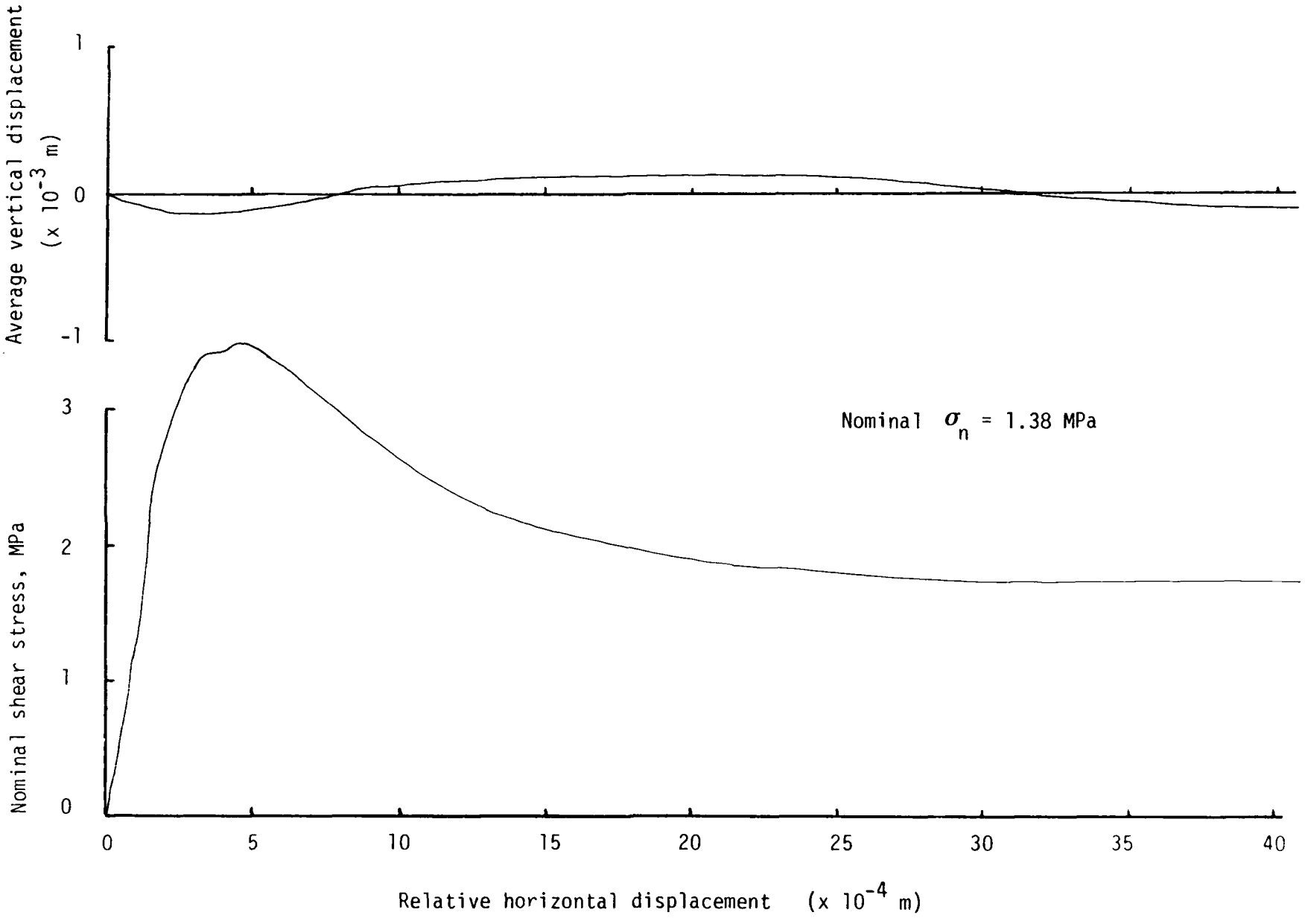

Fig. 3-13 Nominal shear stress and average vertical displacement vs. relative displacement response curves for concrete specimens in the direct shear apparatus.

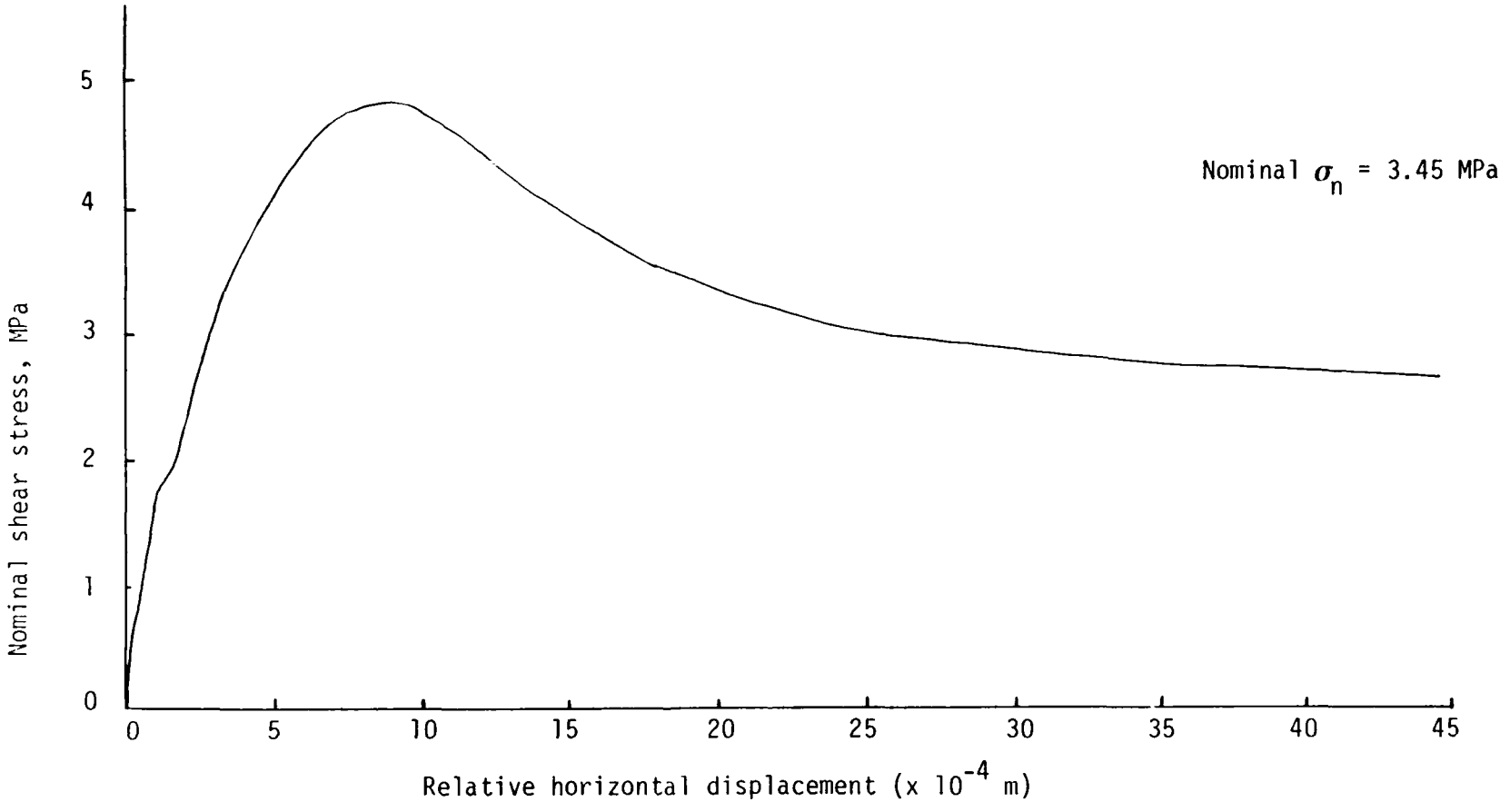

Fig. 3-14 Nominal shear stress-relative displacement response curve for concrete specimen in the direct shear apparatus.

stable throughout the shearing process, although spontaneous energy releases in the post-peak strain-softening branch of the nominal shear stress-displacement response diagrams indicate small rate increases. Real-time xyy' plots of the events also gave this impression. Nevertheless, it is maintained that the strain-softening branches in Figs. 3-10, 3-11, and 3-13 represent the behavior of the concrete miniature structure subjected to well-defined boundary conditions.

3.4 Direct Tension Tests

Direct tension experiments on NX-size and prismatic 10 cm x 4.5 cm x 5.4 cm specimens were conducted to establish the unconfined tensile strength and the strain-softening parameters of the concrete in tension. The prismatic specimens were attached to aluminum brush platen loading devices by means of a high strength structural epoxy (Sikadur Hi-Mod GeL and Lv). The brushes served to reduce the lateral restraint normally imposed by solid loading platens on the specimen. No post-peak strength or strain-softening information was provided by the load-controlled experiments. The tensile failures were quite violent and unstable. Two successfully completed direct tension tests in the strain-softening regime were conducted on the NX-size specimens under displacement control. These specimens were glued "in place" with the same epoxy to specially prepared solid loading platens, which in turn were rigidly connected to the MTS loading frame. Axial load and displacement of the specimen were recorded by MTS internal load cell and LVDT, and the load-displacement responses were also in these cases continously recorded by an x-y plotter. Figure 3-15 shows nominal axial

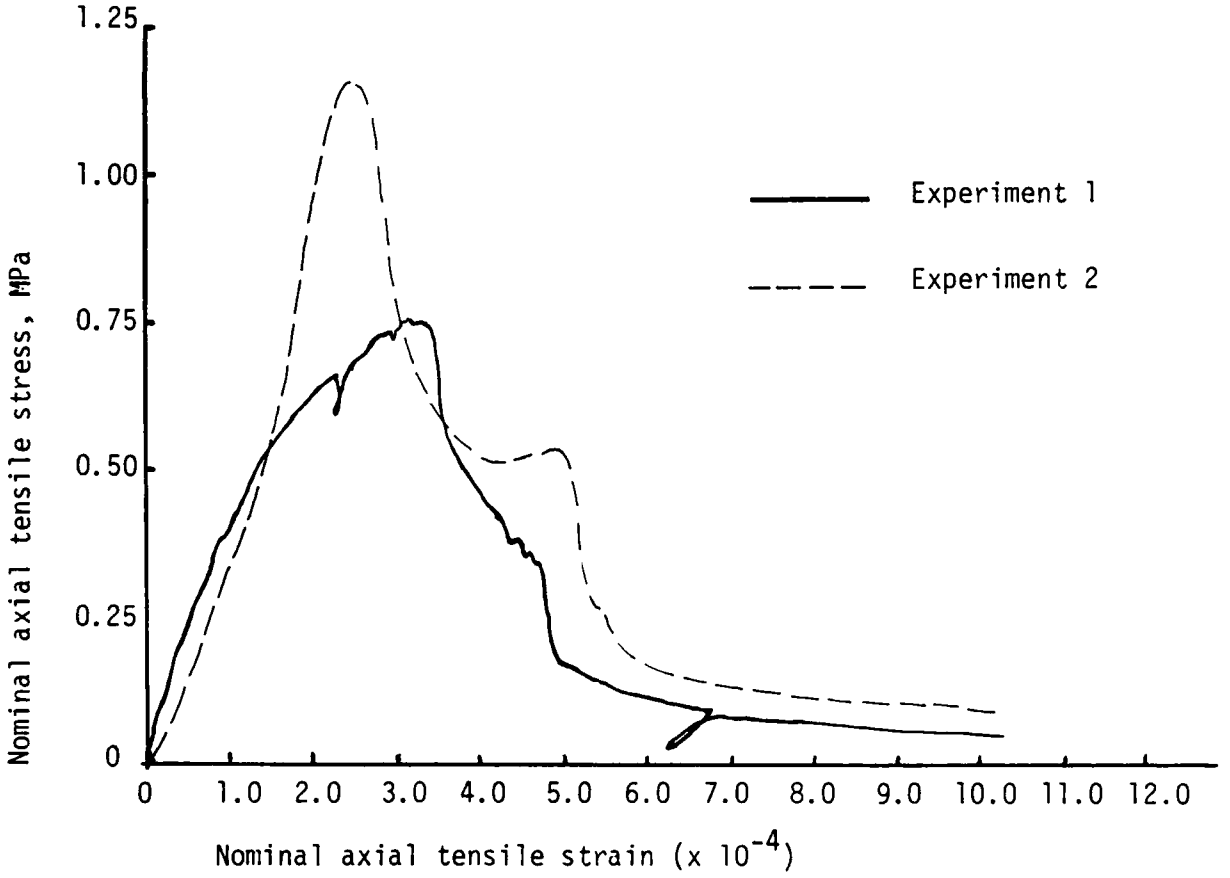

Fig. 3-15 Uniaxial tensile stress-nominal axial tensile strain response curves for concrete.

tensile stress vs. nominal axial strain response curves for one of the two NX-size specimens. The displacement rates were maintained constant at 1.4×10^{-8} in/sec. No visible tensile crack bands were observed at peak strength or during strain-softening descent in any of the specimens. A very narrow, nearly planar and jagged hairline crack band was observed almost simultaneously around the periphery of the sample at near mid-height, when the load-displacement response trace reached the residual strength near zero load level. When it was first observed the tension crack was not larger than 2.5×10^{-5} m (0.001 in.) wide, and it subsequently increased in width in proportion with the constant displacement rate. It is believed that tensile cracking started to form within the specimen and that it propagated from the interior to the exterior surface.

The momentary hesitations that are observed in the strain-softening branches can possibly be attributed to aggregate interlock mechanisms in conjunction with a nonuniform axial stress distribution. Significant flexural stresses may arise due to the fracture process, which in turn may produce minor compressive stress states in certain regions that in turn may provide momentarily stabilizing responses.

Post-experiment inspection of the specimen revealed that the tensile fracture intersected the large aggregates (0.6 cm size) that were present in the fracture zone. A fine dust layer originating from the cement matrix in the fracture zone was uniformly distributed and the amount was less than 0.05 g. No fissures or delaminations were uncovered near or at the epoxided contact regions, and no other visible

fractures were discovered within the specimen. The intact specimen parts were quite competent and did not crumble during manipulation. It is therefore asserted that the entire strain-softening response was attributed to the very narrow tensile fracture zone.

The specimen exhibiting lower strength was preloaded in compression to an unknown extent during the specimen preparation phase, and the nominal stress at failure is therefore not a precise assessment of strength. The other experiment was started at a nearly zero initial stress level, and it is therefore believed that this tensile strength is representative of the concrete.

4. COMPUTATIONAL ASPECTS OF SOFTENING MODEL

Computational finite element predictions of the softening behavior using the "smeared" approach imply an "equivalent" continuum discription of the properties of fractured solids. It has been demonstrated in sections 1 and 2, that softening behavior is only possible if a damage zone of finite dimensions exists. Therefore the constitutive model for strain-softening computations should include this geometric effect.

The distinction is made between the two possible fracture mechanisms - tensile cracking and shear slip on the corresponding planes of incipient fracture. At this stage, shear and tensile softening mechanisms are treated separately, in order to control the overall rate of shear and tensile strength degradation of the "equivalent" continuum which is developed using energy balance arguments during the fracturing process.

4.1 Composite Damage Model for Localized Strain Softening Behavior

The computational investigation is based on a composite damage model for elastic-fracturing behavior, where fracture is confined to the localized damage zone. In order to be able to model localized fracture bands within the "smeared crack" approach it is assumed that the finite element volume V_t is composed of two parts, the intact elastic volume V_e and the volume of localized damage V_d, see Fig. 4-1.

$$V_t = V_e + V_d \tag{4.1}$$

The behavior within the volume of localized damage V_d follows the damage zone material law, whereas the material within the intact volume

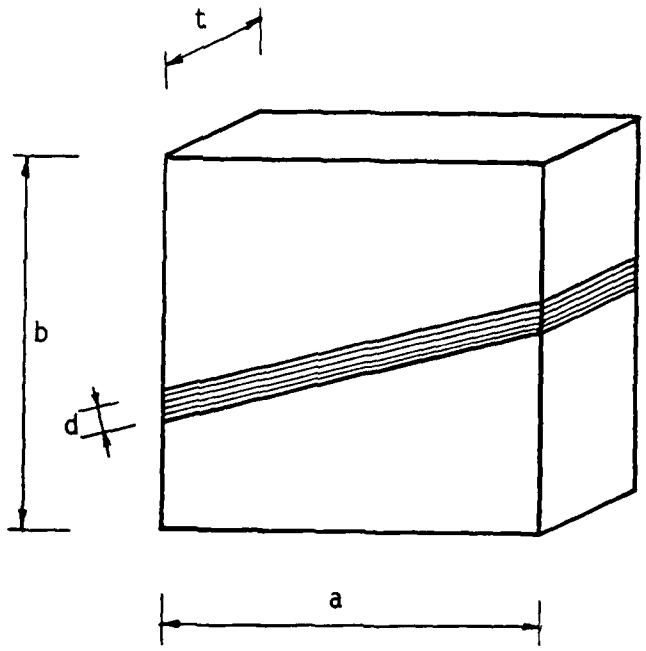

$V = a\ b\ t$

$V_d = d\sqrt{a\ b}\ t$ Localized damage volume

$V_e = V - V_d$

$\sqrt{a\ b}$ Equivalent square element side for unit thickness

$\alpha = V_d / V$ Damage volume fraction

Fig 4-1 Composite damage element

is assumed to remain linear elastic. The orientation of the localization will be neglected in this scalar representation of damage.

Two distinct localized damage mechanisms, tensile cracking and shear slip, will be examined separately. In both cases the fracture energy absorption capacity of the equivalent continuum element is assumed to equal the fracture energy absorption capacity of the damage zone in the composite element.

4.1.1 Tensile Cracking

Let us assume for simplicity that the material in the tensile damage zone $V_{d,t}$ follows a linear elastic/linear softening law. The slope of the softening branch in the fracture strain description of the damage zone law is denoted by $E_d^E = \eta_t E$, see Fig. 4-2. At rupture the total strain in the damage zone ε_r^D equals the fracture strain in the damage zone, $\bar{\varepsilon}_r^D$.

The axial displacement of the comoposite element at rupture is therefore

$$u^{CE} = L_{d,t}\, \varepsilon_r^D \tag{4.2}$$

As a result of the material law of the equivalent continuum element follows the linear elastic/linear softening law, whereby E_s denotes the softening slope normally used in the smeared approach. If the deformations of the composite and the continuum element are to be compatible, the axial displacement must be the same, i.e., $u^{CE} = u^{EQ}$. This, in turn, implies that the total strain at rupture of the equivalent element must be

$$\varepsilon_r = \alpha_t \varepsilon^D{}_r \tag{4.3}$$

where

$$V_{d,t} = L_{d,t}\, A$$

$$V = L\, A$$

$$d_t = \frac{V_{d,t}}{V} = \frac{L_{d,t}}{L}$$

From this relation we can extract the softening slope of the equivalent continuum element as

$$E_s = \frac{\sigma_f}{\varepsilon_r - \varepsilon_f} = \frac{\sigma_f}{\alpha_t \varepsilon_r^D - \varepsilon_f} \tag{4.4}$$

Recalling that at rupture $\varepsilon_r^D = \bar{\varepsilon}_r^D = \frac{\sigma_f}{E_d^D} = \frac{\sigma_f}{n_t E}$

We can write

$$E_s = \frac{\sigma_f}{\alpha_t \frac{\sigma_f}{n_t E} - \frac{\sigma_f}{E}} = E\left(\frac{n_t}{\alpha_t - n_t}\right) \tag{4.5}$$

Note that this expression defines E_s in terms of the material law E_d^D in the damage zone and the size effect $L_{d,t}$ of the damage zone. It is interesting to note that the same expression arises from the fracture energy equivalence in the damage volume of the composite element $V_{d,t}$ and the total volume V of the equivalent continuum element, see Fig. 4-2.

$$U_{dis}^{EQ} = \frac{1}{2}\left(\frac{\sigma_f}{E} + \frac{\sigma_f}{E_s}\right) \sigma_f\, V_d \tag{4.6}$$

$$U_{dis}^{CE} = \frac{1}{2}\left(\frac{\sigma_f}{E_d^D}\right) \sigma_f \quad V_{d,t} \tag{4.7}$$

DAMAGE ZONE MATERIAL LAW

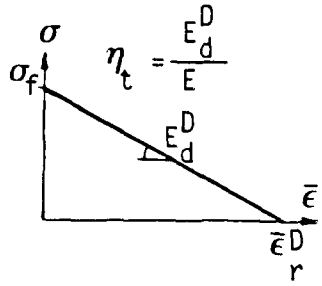

COMPOSITE DAMAGE ELEMENT

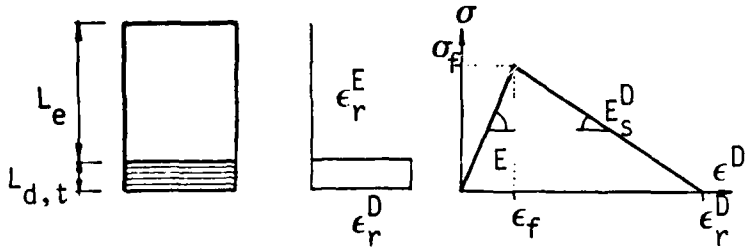

strain distribution at rupture

stress/strain law in tensile damage zone

EQUIVALENT CONTINUUM ELEMENT

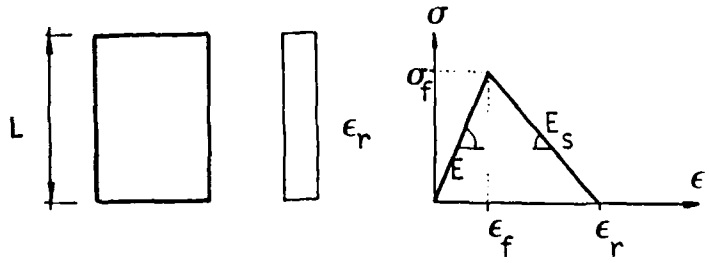

strain distribution at rupture

stress/strain law in equivalent continuum element

Fig 4-2 Fracture energy equivalence for the composite damage model in tension

from $U_{dis}^{EQ} = U_{dis}^{CE}$, it follows that

$$E_s = E \left(\frac{\eta_t}{\alpha_t - \eta_t}\right) \tag{4.8}$$

It should be noted that both the material law E_d^D and the size of the damage zone $V_{d,t}$ influence the softening slope in the equivalent continuum element.

In fact, this formulation provides the missing link between the usual softening approach for continuous distribution of microdefects [24], and the crack band approach of localized fracture [28].

In the usual continuous softening approach the softening modulus E_s is assumed to be a material property, in the same way as the elastic modulus E. This approach is recovered in the composite damage model for $\alpha_t = 1.0$, i.e. $L_{d,t} = L$, hence the equivalent element behaves according to the damage zone law, $E_d^D = \eta_t E$. If we change from one finite element idealization to another then $\alpha_t = 1.0$ will keep the fracture energy density constant but not the total fracture energy release because of the different volume.

On the other hand, if the size and the law of the damage zone are assumed to be constant, the crack band model is recovered in our composite damage model. Varying the mesh size, $L_j \neq L_i$, the equivalent softening modulus E changes, since $\alpha_{t_i} = \frac{d_t}{L_i}$ is different from $\alpha_{t_j} = \frac{d_t}{L_j}$. As a result, the variable softening modulus E_s for different meshes implies that the fracture energy content is kept constant independently of the mesh size.

It is expected that the former fomulation will perform better in the case of distributed fracture, whereas the latter will lead to less mesh sensitivity in the cases of highly localized fracture.

The identification of both the material law and the size of the damage zone from only one direct tension test presents an underdetermined problem. We have to predefine the material law in the damage zone to be able to identify the damage zone size, or vice versa - we can predefine the damage zone size, and identify the material law within the damage zone. One way of reducing the number of free damage parameters would be to define the material law as a function of the damage zone size, i.e.

$$\eta_t = f(\alpha_t) \tag{4.9}$$

The softening slope of the equivalent element will then be controlled only by the size of the damage zone. Figure 4-3 illustrates several possibilities for the equivalent softening moduli, E_s, depending on the choice of $\eta_t = f(\alpha_t)$.

4.1.2 Shear Slip

In analogy with the development of the composite damage model in tension, let us assume that the material in the shear damage volume $V_{d,s}$ follows the linear elastic linear softening law, including the residual shear strength, see Fig. 4-4.

At the state of straining corresponding to the residual shear strength level, the shear slip strain equals

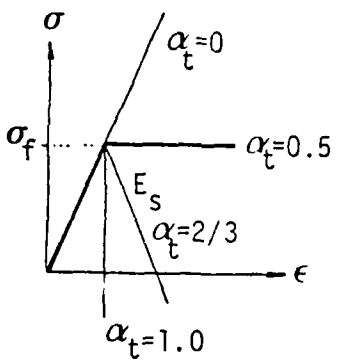

$\eta_t = 2\alpha_t - 1$

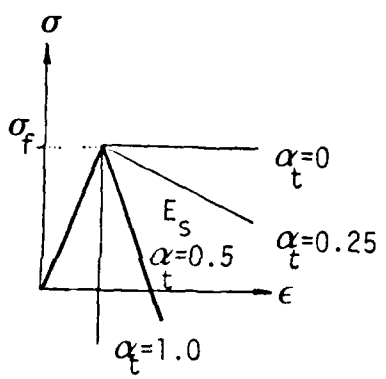

$\eta_t = \alpha_t^2$

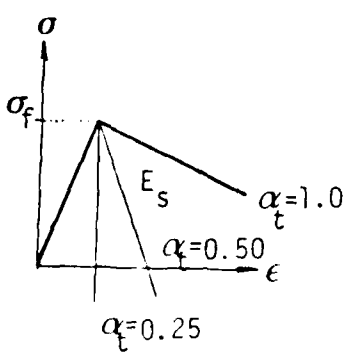

$\eta_t = 0.25$

Fig 4-3 Equivalent softening moduli for three different $\eta_t = f(\alpha_t)$

DAMAGE ZONE MATERIAL LAW

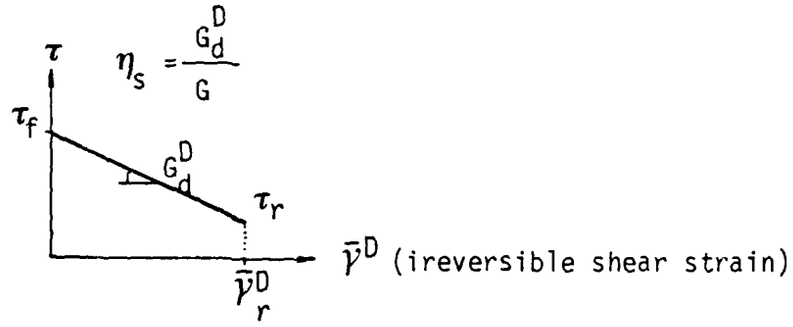

COMPOSITE DAMAGE ELEMENT

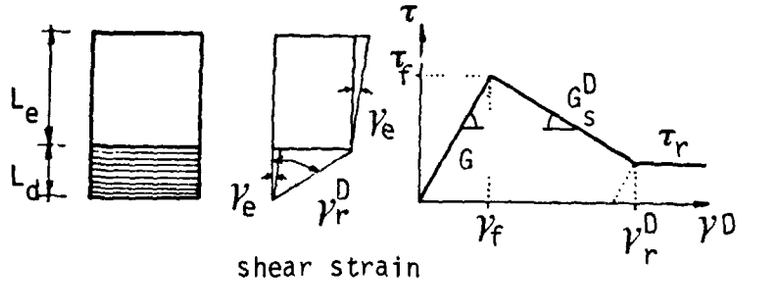

shear strain distribution at residual level

shear stress/strain law in the damage zone

EQUIVALENT CONTINUUM ELEMENT

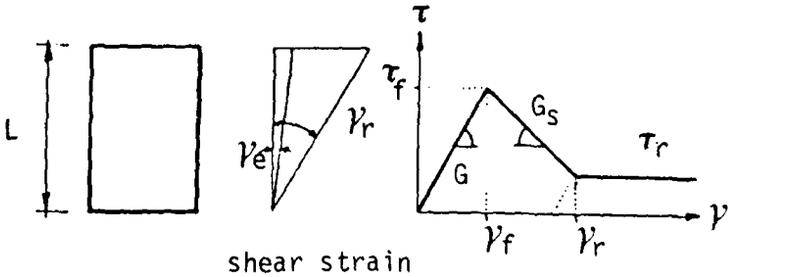

shear strain distribution at residual level

shear stress/strain law in the equivalent element

Fig 4-4 Fracture energy equivalence for the composite damage element in shear

$$\gamma_r^D = \frac{\tau_{ult} - \tau_{res}}{G_d^D} = \frac{\tau_{ult} - \tau_{res}}{\eta_s G} \qquad (4.10)$$

The shear displacement of the composite element at that stage is therefore

$$\Delta^{CE} = L_{d,s}\, \gamma_r^D + L_e \frac{\tau_{res}}{G} \qquad (4.11)$$

As a result, the linear elastic/linear softening law of the equivalent continuum element with the softening slope G_s, derives from the equivalence of shear displacement, i.e. $\Delta^{CE} = \Delta^{EQ}$ leads, in analogy to Eq. 4.3, to

$$\gamma_r = \alpha_s\, \gamma_r^D \qquad (4.12)$$

Therefore we can recast the softening slope G_s of the equivalent continuum element in terms of the elastic shear modulus, the damage volume fraction α_s and the ratio of composite moduli η_s.

$$G_s = G \left(\frac{\eta_s}{\alpha_s - \eta_s}\right) \qquad (4.13)$$

where $$\eta_s = \frac{G_d^D}{G}$$

and $$\alpha_s = \frac{V_{d,s}}{V} = \frac{L_{d,s}}{L}$$

Note that this expression is equivalent to the Eq. 4.4 and involves again the material law as well as the size of the damage zone.

Again the model allows the transition from the usual continuum description ($\alpha_s = 1.0$, η_s = const) to the constant shear band model ($d_s = V_{d,s}$ = const, η_s const). For various meshes,

the first formulation keeps the shear fracture energy density constant, while the second keeps the total shear fracture energy constant independently of the element mesh.

The identification of both damage volume material and damage volume size from experiment presents again an underdetermined problem. If we want to control the softening slope of the equivalent continuum element only by the size of the damage zone an additional assumption has to be made for the material law in the damage volume. Fig. 4-5 illustrates several possibilities for the equivalent softening shear moduli, G_s, depending on the choice of

$$\eta_s = f(\alpha_s) \tag{4.14}$$

4.2 Nonlinear Finite Element Solution Procedure

The composite damage model for softening behavior, described earlier, both for shear slip as well as tensile cracking represents an alternative description to the traditional strain softening stress/strain relation used in the smeared cracking approaches. In our case the smearing of localized damage is accomplished by the damage volume fractions α_t and α_s within the equivalent element.

The finite element displacement formulation is adopted, for the incremental solution of the nonlinear boundary value problem which satisfies the constitutive constraints in the small, and equilibrium in the large

$$K_r \Delta r = \Delta R \tag{4.15}$$

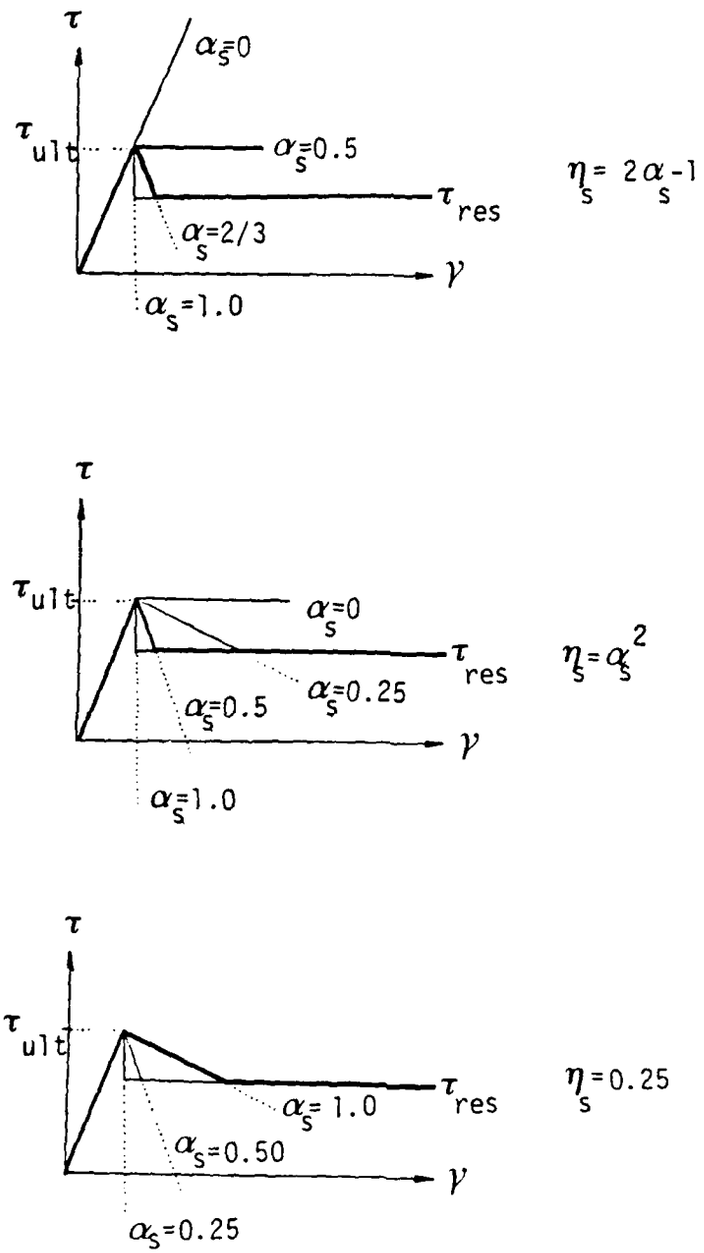

Fig 4-5 Equivalent shear softening moduli for three different $\eta_s = f(\alpha_s)$

For simplicity of implementation, $K_r = K_0$ has been adopted, which requires an iterative improvement within each loading step,

$$\Delta r_i = K_0^{-1} \Delta R_i \tag{4.16}$$

until convergence corresponding to the criterion of stable fracture propagation is satisfied.

The triaxial concrete strength is represented using the Mohr-Coulomb fracture surface augmented with a tension cut-off condition, which provides a simple and realistic model of triaxial material strength in the range of interest. The geometric interpretation of the fracture surface is shown in principal stress space in Fig. 4-6. Since, in the planar case, these criteria do not take into account the intermediate principal stress, the surface can be easily represented in the biaxial stress space, or in Mohr's diagram. The main reasons for choosing the Mohr-Coulomb failure surface with tension cut off over some of the other possible surfaces are as follows:

1. The Mohr-Coulomb model has been widely used in geotechnical applications for over 200 years and has been shown to provide realistic shear slip conditions for geomaterials. The extension to concrete is quite reasonable when the tension cut-off condition is included.
2. These two traditional strength criteria provide a basis for a simple engineering fracture theory capable of separate predictions of tensile cracking

and shear slip. In this light, the discontinuous surface is also able to determine the direction of the associated failure planes of tensile cracking and frictional slip.

3. The identification of the fracture surface requires only three parameters, which can be found from standard laboratory tests.
4. The straight line approximation of the Mohr-Coulomb surface is easily incorporated into existing finite element computer codes. To utilize the Mohr-Coulomb failure criterion for concrete, only three material parameters - the angle of internal friction, the internal cohesion and tension cut-off-are required.

In the view of the linear softening model, two sets of parameters have to be provided; one set corresponding to the initial fracture criterion, and the other corresponding to the residual fracture strength e.g. due to internal friction. In the post-peak regime the linear rate of degradation of the fracture surface from the initial to the residual level is controlled by the tangential softening moduli E_s and G_s see Fig. 4-7.

The analysis is carried out by taking suitable load steps for piecewise linearization of the structural response curve. For each load step the algorithm involves initial load iterations until equilibrium as well as fracture conditions are satisfied. During each iteration loop element nodal stresses are compared to the initial fracture criteria, to

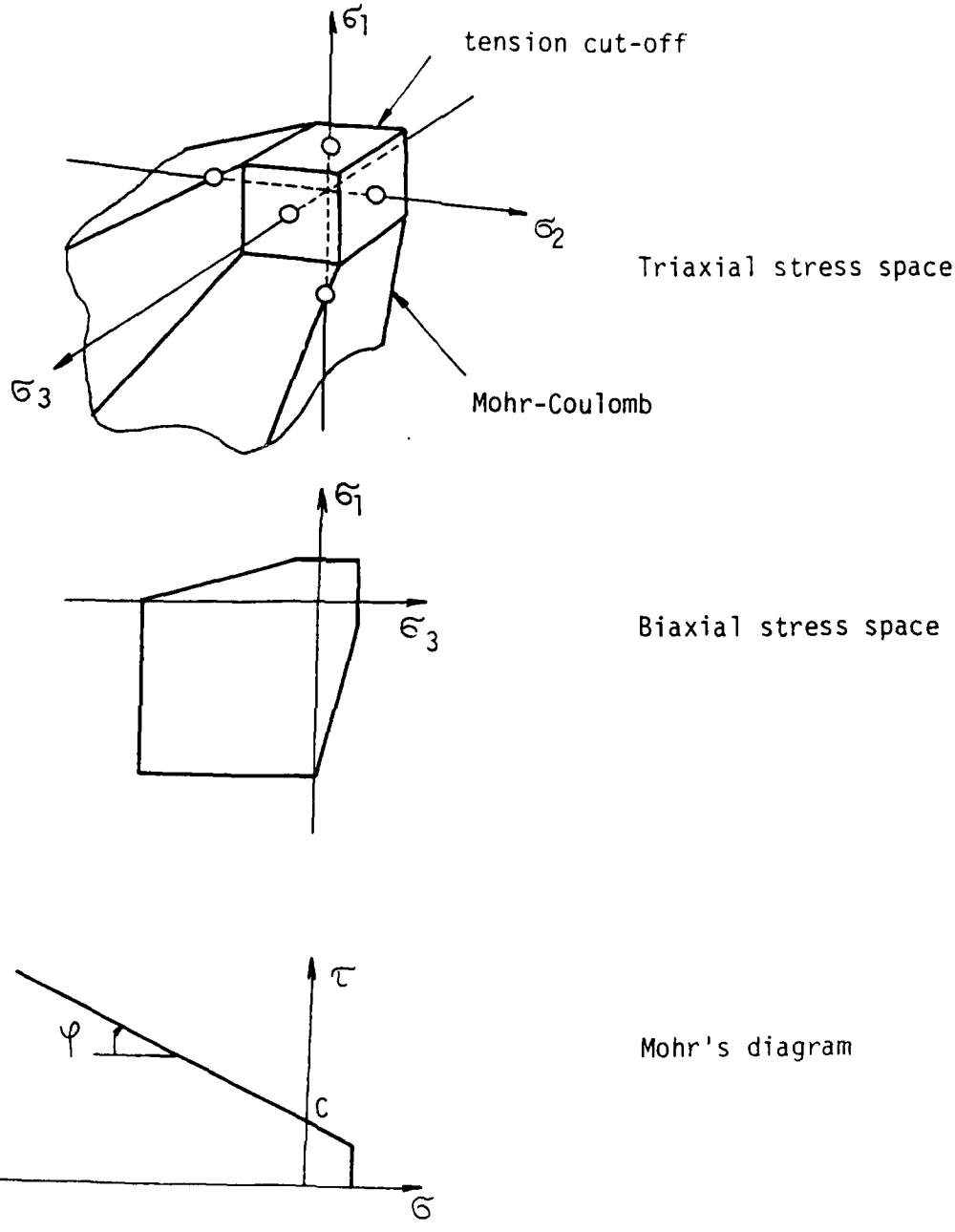

Fig 4-6 Different representations of Mohr-Coulomb with tension cut-off fracture surface

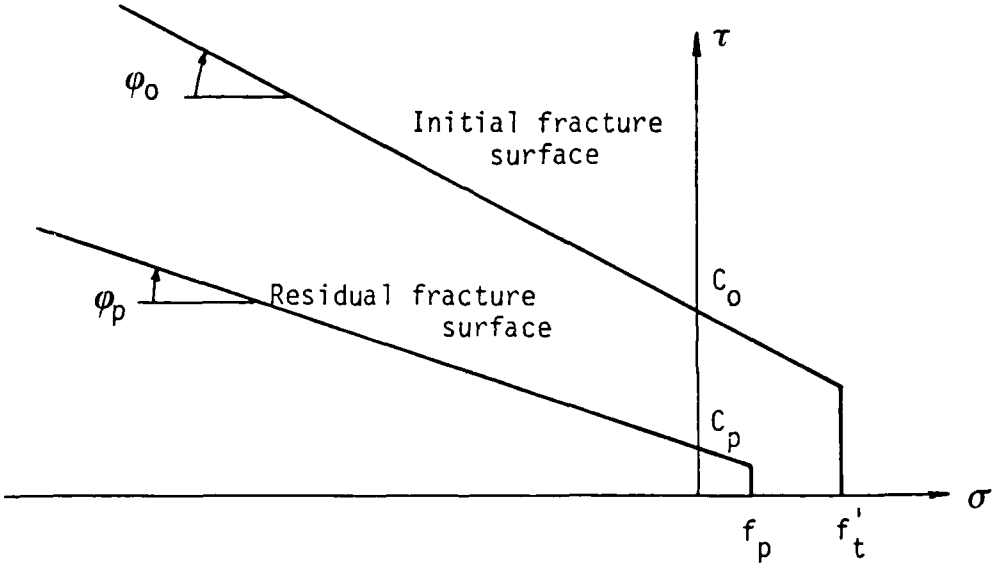

Fig 4-7 Parameters defining the initial and residual fracture surfaces

establish possible formation of either tensile cracks or shear slip planes.

If the state of stress at a point violates the momentary fracture criteria, the excess stress is redistributed to other parts of the finite element mesh, i.e. nodal forces equivalent to the excess stress are used to enforce a solution where the fracture criteria will be satisfied. The stresses which have to be distributed depend on the fracture mode (tensile cracking or shear slip), and will be discussed later in detail. Once defined, the redistributed stresses, or stress increments, are used to compute initial loads for the iteration using the initial stiffness $\mathbf{K}_o$. The iterations for each load step are performed in the following sequence.

1. The redistribution stress increments are rotated from their principal directions into Cartesian directions:

$$\Delta\boldsymbol{\sigma}_c = \mathbf{T}^{-1}\ \Delta\boldsymbol{\sigma}_p \tag{4.17}$$

2. The incremental Cartesian stresses are converted into incremental initial strains via the material matrix:

$$\Delta\boldsymbol{\varepsilon}_o = \mathbf{E}^{-1}\ \Delta\boldsymbol{\sigma}_c \tag{4.18}$$

3. The incremental strains are used to compute the initial incremental element nodal loads:

$$\Delta\mathbf{P}_o = \int_{V_e} \mathbf{B}^t\mathbf{E}\Delta\boldsymbol{\varepsilon}_o dV \tag{4.19}$$

4. The incremental element nodal loads are added to the current nodal loads R_i, and assembled into the global load vector, R_{i+1}:

$$R_{i+1} = R_i + \sum_e a^t \Delta P_o \tag{4.20}$$

5. The global load vector and the initial structural stiffness matrix are used to solve for the new incremental displacements r_{i+1}:

$$r_{i+1} = K_o^{-1} R_{i+1} \tag{4.21}$$

This iteration procedure is repeated during each load step, until the convergence is achieved, or the maximum number of iterations is exceeded. The convergence norm is defined as relative error norm of the displacment increment

$$\sum_{j=1}^{NOP} \left| \frac{u_{j,i+1} - u_{j,i}}{u_{max}} \right| \leq \delta \tag{4.22}$$

When the calculated error norm is less than or equal to the convergence threshold δ, the iteration is terminated. Incremental displacements r_{i+1} are added to the existing displacements to form new total displacements. The stresses and strains are updated during the looping, so no further correction is required.

4.3 Stress Redistribution Strategies

The dual Mohr-Coulomb with tension cut-off criterion clearly distinguishes between shear and tensile failure. Depending on the nature of failure, different stress redistribution strategies have to be employed.

4.3.1 Tension Cut-Off Criterion and Stress Transfer

Tensile cracking is initiated when the principal tensile stress exceeds the initial tension cut-off value, f_t'.

$$\sigma_1 > f_t' \tag{4.23}$$

When this criterion is satisfied, the stress in excess of the post-peak tension cut-off is redistributed according to the normality rule so that the momentary post-peak strength criterion f_s is met. The amount of st ..s (Fig. 4-8) to be redistributed is

$$\Delta\sigma_1 = \sigma_1 - f_s \tag{4.24}$$

For the tensile softening model, the controlling parameter is a function of the principal strain quantities ε_1, ε_2 and ε_2 where $\varepsilon_3 = 0$ for plane strain conditions.

Starting with the material law the stress-strain relation for plane strain case can be written as

$$\begin{bmatrix} \sigma_1 \\ \sigma_2 \end{bmatrix} = \begin{bmatrix} E_{11} & E_{12} \\ E_{12} & E_{22} \end{bmatrix} \begin{bmatrix} \varepsilon_1 \\ \varepsilon_2 \end{bmatrix}$$

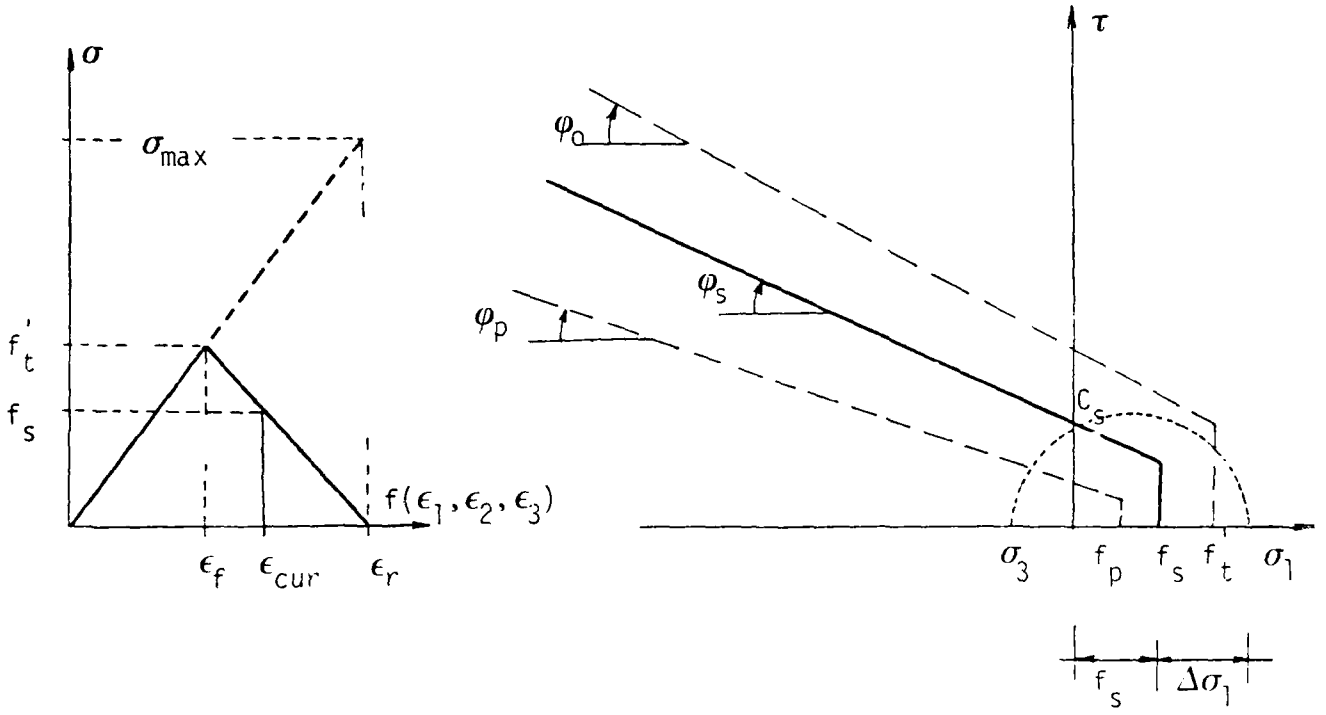

Fig 4-8 Parameters for the current post-peak fracture surface

AD-A141 866 IDENTIFICATION OF STRAIN-SOFTENING PROPERTIES AND COMPUTATIONAL PREEICTIO.. (U) COLORADO UNIV AT BOULDER DEPT OF CIVIL ENVIRONMENTAL AND ARCH.. 2/2

UNCLASSIFIED K J WILLAM ET AL. 01 MAR 84 F/G 11/2 NL

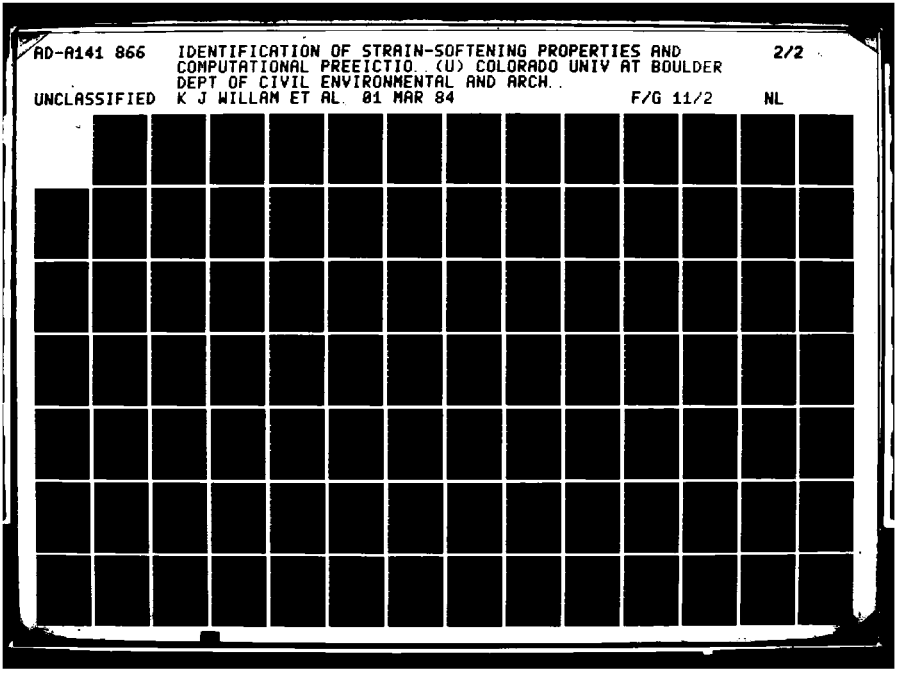

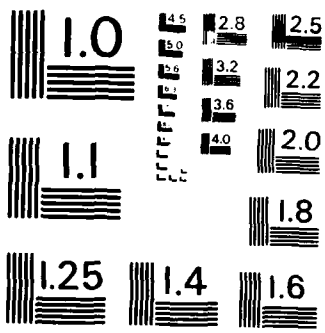

Then:

$$\sigma_1 = E_{11}\,\varepsilon_1 + E_{12}\,\varepsilon_2 \qquad (4.25a)$$

It should be noted that for axisymmetric conditions $\varepsilon_3 \neq 0$ and appropriate modification of σ_1 leads to

$$\sigma_1 = E_{11}\,\varepsilon_1 + E_{12}\,(\varepsilon_2 + \varepsilon_3) \qquad (4.25b)$$

With reference to Fig. 4-8, the tensile strength is reduced according to the linear softening model when

$$\sigma_1 > f_t'$$

and residual tensile strength is equal to zero when $\varepsilon > \varepsilon_r$.

For the linear softening, the post-peak strength, f_s, can be determined in terms of a fictitions strength value σ_{max}, such that:

$$f_s = 0.0$$

if

$$E_{11}\,\varepsilon_1 + E_{12}\,(\varepsilon_2 + \varepsilon_3) > \sigma_{max} \qquad (4.25c)$$

Using the relation between the softening modulus E_s and the initial elasticity modulus E, Eq. 4.4, the fictitious stress σ_{max} can be written as

$$\sigma_{max} = f_t'\,(1 + \frac{E}{E_s}) = f_t'(1 + (\frac{1-\alpha_t}{1-2\alpha_t})) \qquad (4.26)$$

The instantaneous post-peak strength f_s, corresponding to current state of cartesian strain ε_c can then be written as

$$f_s = \frac{\sigma_f}{(\sigma_f - \sigma_{max})} (E_{11}\ \varepsilon_1 + E_{12}\ \varepsilon_2 + E_{12}\ \varepsilon_3 - \sigma_{max}) \qquad (4.27)$$

which is used for the computation of tensile stress redistribution $\Delta\sigma_1$.

4.3.2 Shear Slip and Excess Shear Stress Redistribution Strategies

Shear slip is initiated when the standard Mohr-Coulomb criterion

$$\left|\tau_\theta\right| = C_o - \frac{(\sigma_1+\sigma_3)}{2}\tan\phi_o \qquad (4.28)$$

is violated. Fracture according to this criterion results in the formation of two slip planes, the orientation of these slip planes being

$$\theta = \frac{\pi}{4} + \frac{\phi_o}{2}$$

These crack orientations are kept constant during subsequent computations so that the post-peak strength criteria can be enforced at the initial slip planes. When the shear criterion is exceeded, the excess shear stress has to be redistributed so that the post-peak criteria are met. Unlike the case of the tensile cracking in which the stress redistribution is uniquely defined, several possibilities exist in the case of excess shear redistribution. The Mohr-Coulomb criterion implies that the intermediate principal stress does not play any role. Thus the stress increments required to transfer the stress point onto the instantaneous fracture surface involve the increments of the major and the minor principal stresses $\Delta\sigma_1$ and $\Delta\sigma_3$.

Different redistribution strategies similar to the non-associated flow rules of plasticity can be employed (Fig. 4-9), each of them leading to different development of resulting fracture strains. Four different sets of stress increments $\Delta\sigma_1$ and $\Delta\sigma_3$ associated with the four possible redistribution strategies are illustrated in Fig. 4-9. Two of the redistribution strategies involve the increments of only one of the principal stresses $\Delta\sigma_1$ or $\Delta\sigma_3$, whereas the other two involve increments of both $\Delta\sigma_1$ and $\Delta\sigma_3$ to comply to the current Mohr-Coulomb fracture surface. It has been suggested in Ref. [6] that the strategies or "fracture rules" S1C and SNC do not seem to reproduce the actual fracture mechanism, since they involve significantly longer stress redistribution paths than strategies SMC and S3C. It should be noted that the strategy SMC corresponds to no volume change due to the underlying fracture rule.

The constant volume approach, SMC, which holds the mean pressure constant during the redistribution, is used mainly within this study, although the effects of other strategies will be discussed in Section 5.1. The SMC transfer strategy corresponds to the non-associated Tresca flow rule in plasticity with no plastic volume change during the plastic flow process. The amount of stress to be redistributed after a shear type failure is then given by

$$\Delta\sigma_1 = (\sigma_f - \frac{\sigma_1 + \sigma_3}{2}); \quad \Delta\sigma_3 = -\Delta\sigma_1 \tag{4.29}$$

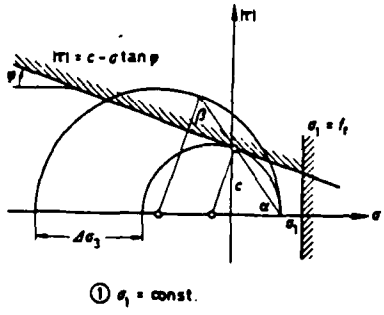

strategy S1C

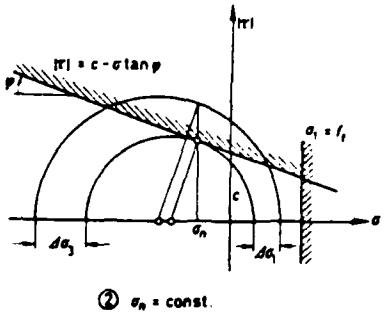

strategy SNC

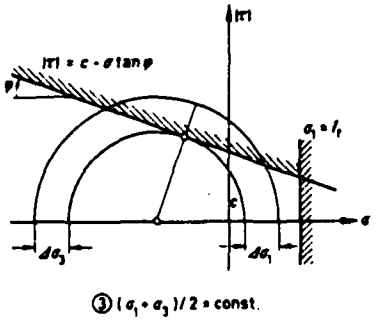

strategy SMC

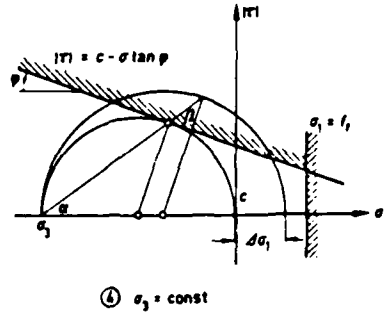

strategy S3C

Fig 4-9 Four stress transfer strategies for excess shear stress

where

$$\sigma_f = \sin\phi_p \left(C_p \cos\phi_p - \frac{\sigma_1 + \sigma_3}{2}\right)$$

The shear stress-strain relation used for the linear softening model is described

for $\gamma_\theta \leq \gamma_{cr}$

$$\tau_\theta = G\gamma_\theta \tag{4.30}$$

for $\gamma_{cr} < \gamma_\theta < \gamma_{res}$:

$$\tau_\theta = G_s (\gamma_\theta - \gamma_{cr}) + \tau_{ult} \tag{4.31}$$

for $\gamma_\theta \geq \gamma_{res}$:

$$\tau_\theta = \tau_{res} \tag{4.32}$$

where the softening slope G_s, is given by

$$G_s = \frac{\tau_{ult} - \tau_{res}}{\gamma_{cr} - \gamma_{res}} \tag{4.33}$$

The ultimate shear strength level is calculated from the initial fracture parameters,

$$\tau_{ult} = \left| \cos\phi_o \left(C_o \cos\phi_o - \frac{\sigma_1 + \sigma_3}{2} \sin\phi_o \right) \right| \tag{4.34}$$

The shear strain at the moment of incipient shear slip can now be written as

$$\gamma_{ult} = \tau_{ult}/G \tag{4.35}$$

The residual shear strength is determined from the residual strength parameters

$$\tau_{res} = \left| \cos\phi_{res} \left(C_{res} \cos\phi_{res} - \frac{\sigma_1 + \sigma_3}{2} \sin\phi_{res} \right) \right| \tag{4.36}$$

The crucial step for the shear softening formulation is the calculation of γ_{res} and G_s, respectively. The composite damage model resorts to fracture energy considerations for shear slip which furnishes the required relationship in terms of damage volume ratio α_s, see Section 4.4.

$$G_s = \frac{1 - 2\alpha_s}{1 - \alpha_s} \tag{4.37}$$

Once the values of τ_{ult}, γ_{ult}, τ_{res} and γ_{res} have been calculated for the given stress state, the post-peak value of τ_θ can be determined depending on the current value of γ_θ. Before the onset of shear fracture, the shear strength depends only on initial values of the internal cohesion, C_o, and the internal friction angle, ϕ_o.

After shear fracture has been initiated, but before the residual strain level is reached, the current shear stress, τ_θ, also determines the cohesion and friction angle during softening, C_p and ϕ_p. Implying linear relation between ϕ and C during softening (Fig. 4-7) leads to

$$C_p = \frac{\tau_\theta}{\cos^2\phi_p} + \frac{\sigma_1 + \sigma_3}{2} \tan\phi_p \qquad (4.38)$$

where

$$\phi_p = \frac{(\phi_o - \phi_{res})}{(C_o - C_{res})}(C_p - C_o) + \phi_o \qquad (4.39)$$

To avoid direct solution for C_p and ϕ_p from these two equations, an iterative trial and error procedure is employed until both equations are satisfied.

When γ_θ exceeds the residual strain level, τ_θ is set equal to τ_{res} corresponding to the residual strength criteria.

$$C_p = C_{res} \qquad (4.40)$$
$$\phi_p = \phi_{res}$$

4.4 Localization Parameters d_t and d_s

It has been stated in Section 4.1 that for the particular choice of the softening law in the damage zone, the softening slope of the equivalent continuum element is controlled only by the size of the

damage zone. In the remaining part of this report we shall adopt the following relation for the damage zone law in tension

$$\eta_t = 2\alpha_t - 1 \tag{4.41}$$

This assumption leads to an expression for the softening modulus of the equivalent continuum element in terms of a single fracture parameter, the damage volume fraction α_t.

$$E_s = E\left(\frac{1 - 2\alpha_t}{1 - \alpha_t}\right) \tag{4.42}$$

A similar approach for frictional slip expresses the shear damage zone law

$$\eta_s = 2\alpha_s - 1 \tag{4.43}$$

which leads to the softening shear modulus of the equivalent continuum element

$$G_s = G\left(\frac{1 - 2\alpha_s}{1 - \alpha_s}\right) \tag{4.44}$$

Examination of Eq. 4.42 indicates that tensile softening is possible only for $\alpha_t > 0.5$, i.e., $V_{d,t} > 0.5\ V_t$.

Therefore, the damage volume $V_{d,t}$ will be decomposed into a hardening and a softening volume

$$V_{d,t} = V^H_{d,t} + V^S_{d,t} \tag{4.45}$$

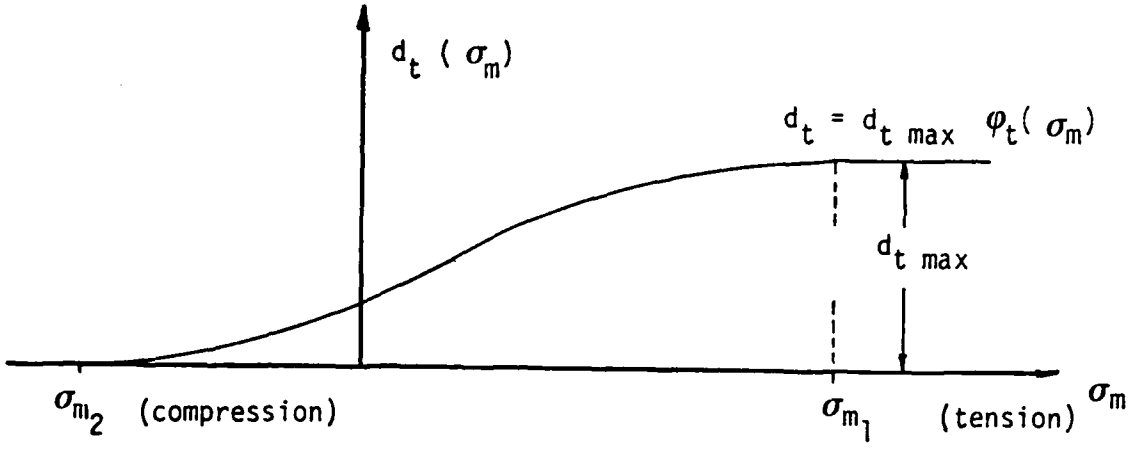

Fig 4-10 Localization function for the tensile crack width vs mean stress

As the main interest of this investigation is related to modelling of softening as localized phenomenon. Thus, it will be assumed that $V_{d,t}^{H} = 0.50\ V_t$ within this formulation, and that the tensile damage volume for softening is described in terms of the localization parameter d_t, which can be interpreted as width of the tensile crack process zone

$$V_{d,t}^{s} = d_t \sqrt{ab}\ \ t \tag{4.46}$$

Therefore, for unit thickness, t=1, the damage volume in tension

$$V_{d,t} = 0.5\ ab + d_t \sqrt{ab}\ , \tag{4.47}$$

and the damage volume fraction in tension

$$\alpha_t = (0.5 + \frac{d_t}{\sqrt{ab}}) \tag{4.48}$$

For generality, it will be assumed that d_t depends on the confinement level described in terms of the mean stress σ_m through the localization function $\phi_t\ (\sigma_m)$

$$d_t(\sigma_m) = d_{t_{max}}\ \phi_t(\sigma_m) \tag{4.49}$$

This pressure sensitivity of the localization parameter allows for increasingly ductile behavior under increasing confining pressure. A third order parabola between two limiting mean stress levels σ_{m_1} and σ_{m_2} is adopted for describing the localization function shown in Fig. 4-10. It should be noted that the damage volume fraction α_t in Eq.

4.42 controls the softening slope E_s of the equivalent continuum. Since V_t is a measure of the actual mesh size, only $V_{d,t}$ or the crack width d_t determines the softening slope of the equivalent element E_s and thus the release of fracture energy during crack propagation.

For shear slip, the damage volume $V_{d,s}$ is decomposed into a hardening and softening contributions

$$V_{d,s} = V^H_{d,s} + V^S_{d,s} \qquad (4.50$$

The damage volume for hardening is again $V_{d_H,s} = 0.50\ V_t$ because of our focus on shear softening. The damage volume for softening, $V_{d,s}$, is expressed in terms of the shear localization parameter d_s, which defines the width of the shear slip band

$$V^s_{d,s} = d_s \sqrt{ab}\ t \qquad (4.51)$$

In analogy to tensile cracking, we can rewrite for the damage volume in shear for the unit thickness t = 1

$$V_{d,s} = 0.50\ ab + d_s \sqrt{ab}\ , \qquad (4.52)$$

The damage volume fraction in shear is then

$$\alpha_s = (0.50 + \frac{d_s}{\sqrt{ab}}) \qquad (4.53)$$

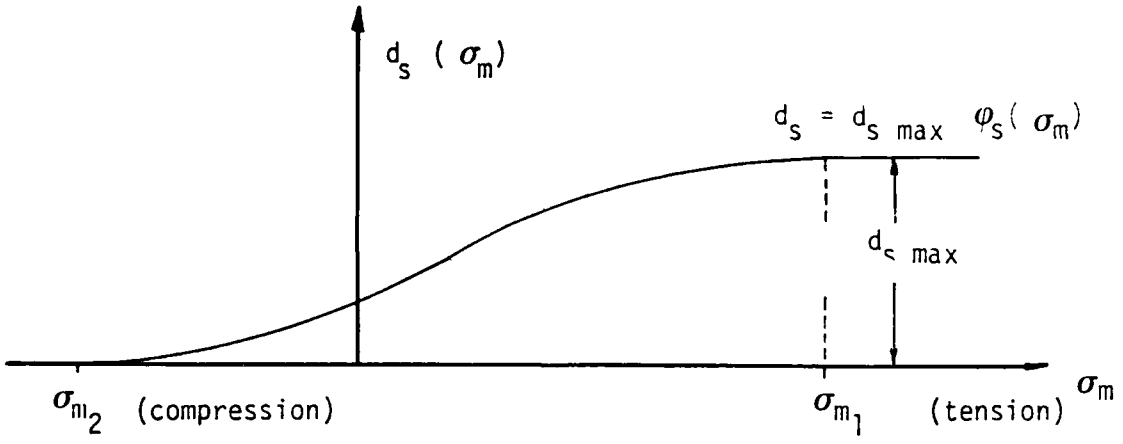

Fig 4-11 Localization function for the shear slip band vs mean stress

The rate of shear softening clearly depends on the hydrostatic confinement. Therefore pressure sensitivity of d_s is included in the form of

$$d_s\ (\sigma_m) = d_{s_{max}}\ \phi_s(\sigma_m) \tag{4.54}$$

where $\phi_s(\sigma_m)$ is the shear localization function allowing for increasingly ductile behavior for increasing confinement. The third order parabola, shown in Figure 4-11, is adopted for $\phi_s(\sigma_m)$ between two limiting mean stress levels similar to the functional variation for tensile cracking.

Again, the presence of α_s in Eq. 4.44 controls the shear softening slope G_s, whereby the width d_s of the shear slip band is defined by

$$d_s = (0.50 + \alpha_s \sqrt{ab}) \tag{4.55}$$

5. CALIBRATION OF LOCALIZATION PARAMETERS FOR TENSILE CRACKING AND FRICTIONAL SLIP

To identify the localization parameters d_t and d_s within the proposed softening model, a series of triaxial compression and direct tension tests have been performed. The experimental setup and results were described in detail in Chapter 3 of this report; here, the calibration of structural softening will be attempted. The procedure involves the computational solution of several inverse problems. First, different localization parameters are assumed and numerical predictions, using these assumptions, are compared with experimental results.

The model parameters for the linear elastic behavior and the Mohr-Coulomb fracture surface (including tension cut-off) are kept constant throughout the calibration procedure for the localization parameters. Based on the experimental results from the first series of tests, the following values were adopted

C_o = 3.28 GPa = 0.476 ksi

ϕ_o = 41.3°

E = 6.9 GPa = 1000 ksi

ν = 0.2

f_t' = 1.59 GPa = 0.230 ksi

It was also assumed that softening only leads to a degradation of cohesion and tensile strength, through the choice of residual fracture parameters

C_p = 0.0

ϕ_p = 41.3°

f_p = 0.0

The calibration procedure involved only the variation of the localiza-

tion parameters d_s and d_t to match experimental results and numerical predictions.

5.1 The Effects of Shear Stress Transfer Strategy

Before attempting the calibration study, the shear stress transfer strategy had to be decided upon. As it has been indicated earlier in Chapter 4, the choice of particular "fracture rule" is not unique, and the effects of different strategies may be different for various applications. To investigate those effects, several numerical predictions of the triaxial Hoek cell test for the confining pressure σ_c = 0.69 MPa (100 psi) were conducted using four different shear stress transfer strategies:

(a) major principal stress (σ_1) remains constant (strategy S1C)

(b) minor principal stress (σ_3) remains constant (strategy S3C)

(c) mean stress $\frac{\sigma_1+\sigma_3}{2}$ remains constant (strategy SMC)

(d) normal stress on fracture plane (σ_n) remains constant (strategy SNC)

In all four cases a 4 * 4 elements mesh of nine noded biquadratic axisymmetric elements has been employed, for the idealization of the quater of the cylindrical specimen. The softening parameters were adjusted to give the rates of softening

G_s = -G in shear

E_s = -E in tension

for all states of stresses. In this case the localization function ϕ was kept constant for all σ_m. Figs. 5-1a,b,c - 5-4a,b,c illustrate the overall force/displacement response curves, the deformed specimen geometries, and the principal stress distributions in the softening

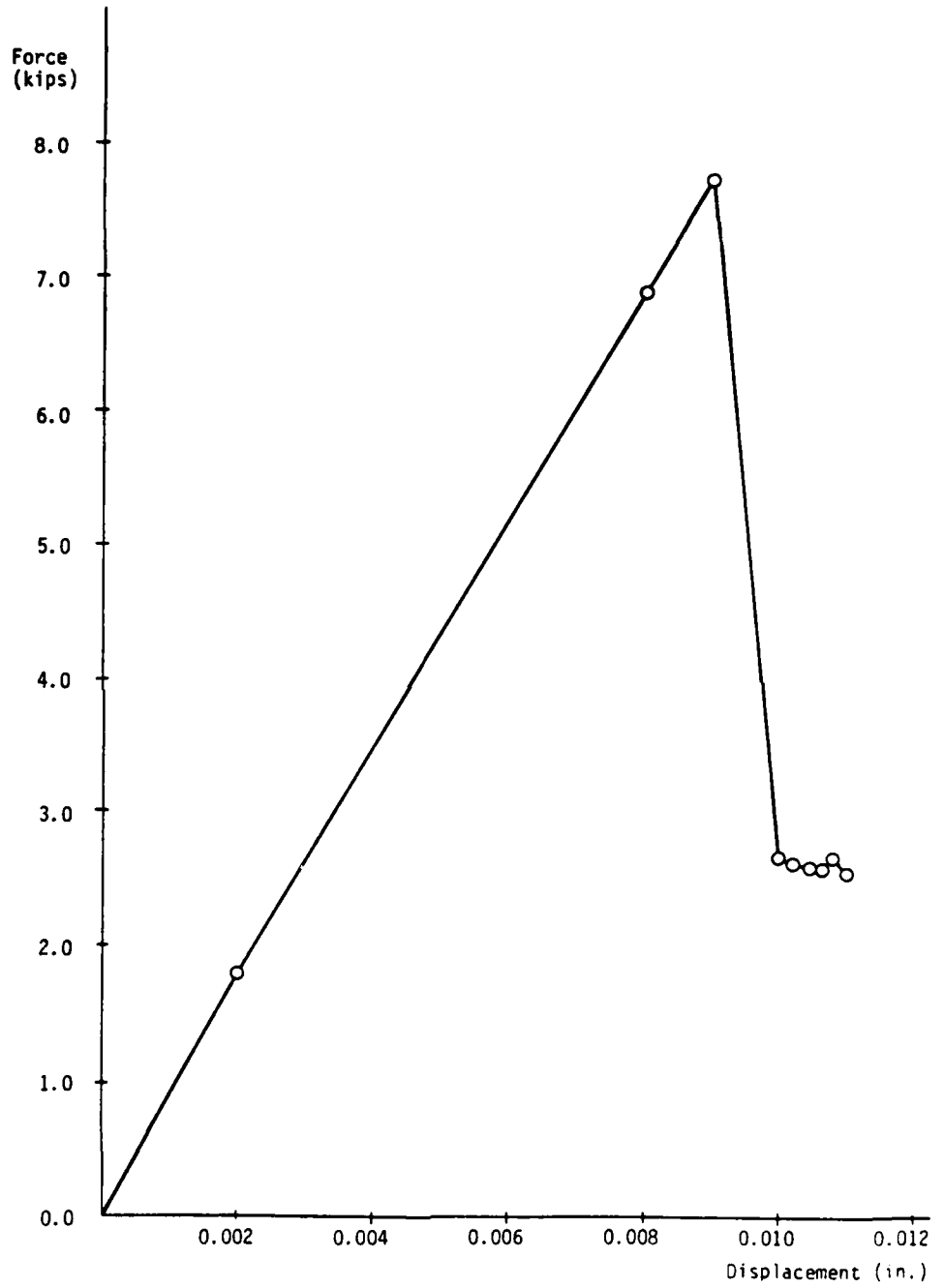

Fig 5-1-a Force-displacement response curve for strategy S1C

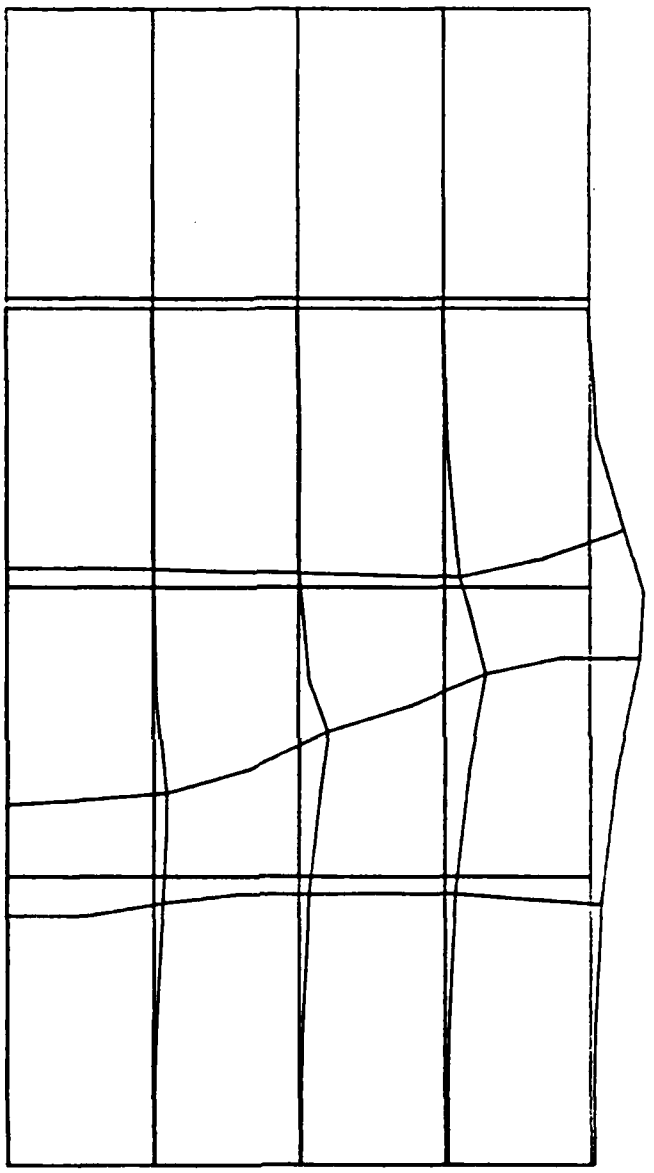

100 PSI

$V_d = V_e$

LOAD STEP NO. 8 ——— = 2.E-1 INCHES GEOM.

——————————— = 1.E-2 INCHES DISP.

Fig 5-1-b Deformed shape (strategy S1C)

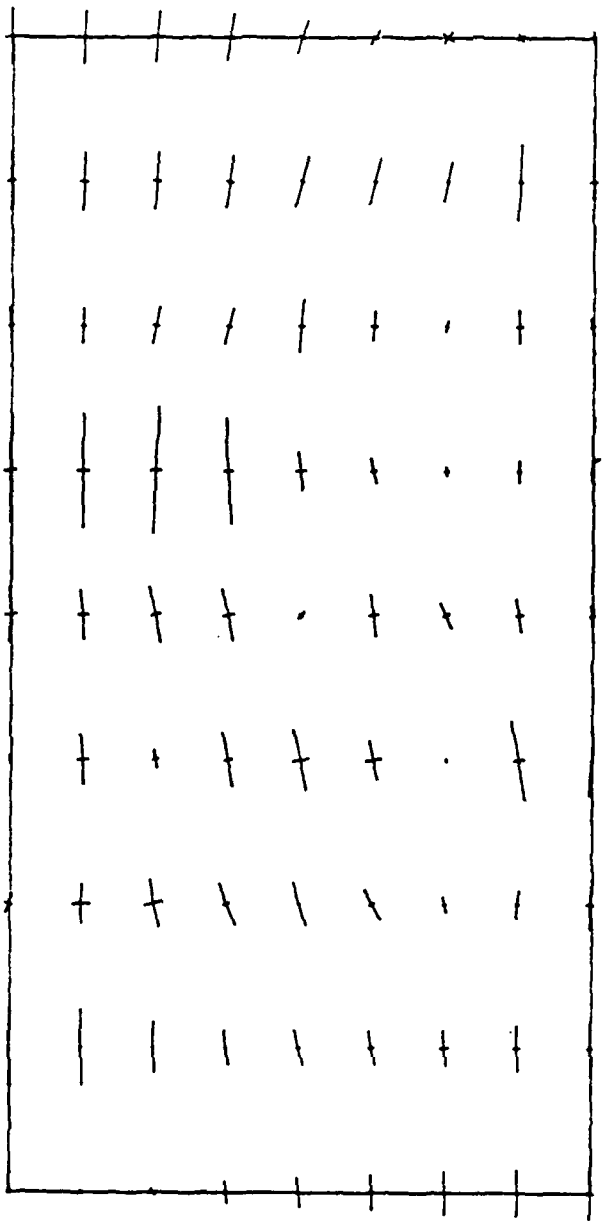

LOAD STEP NO. 8 ····· EQUALS 2 KSI TEN.
——— EQUALS 2 KSI COMP.

Fig 5-1-c Principal stress distribution (strategy S1C)

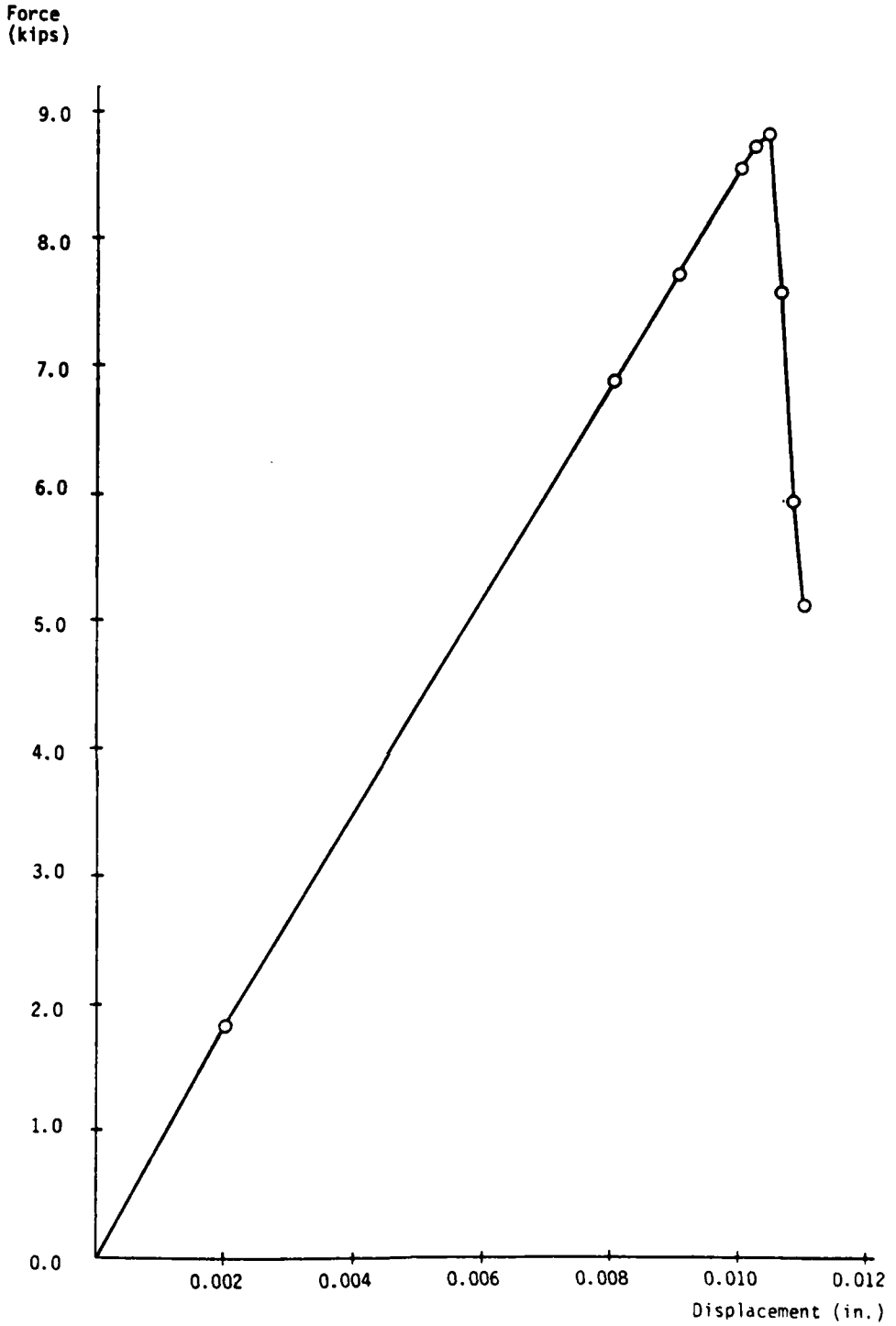

Fig 5-2-a Force-displacement response curve for strategy S3C

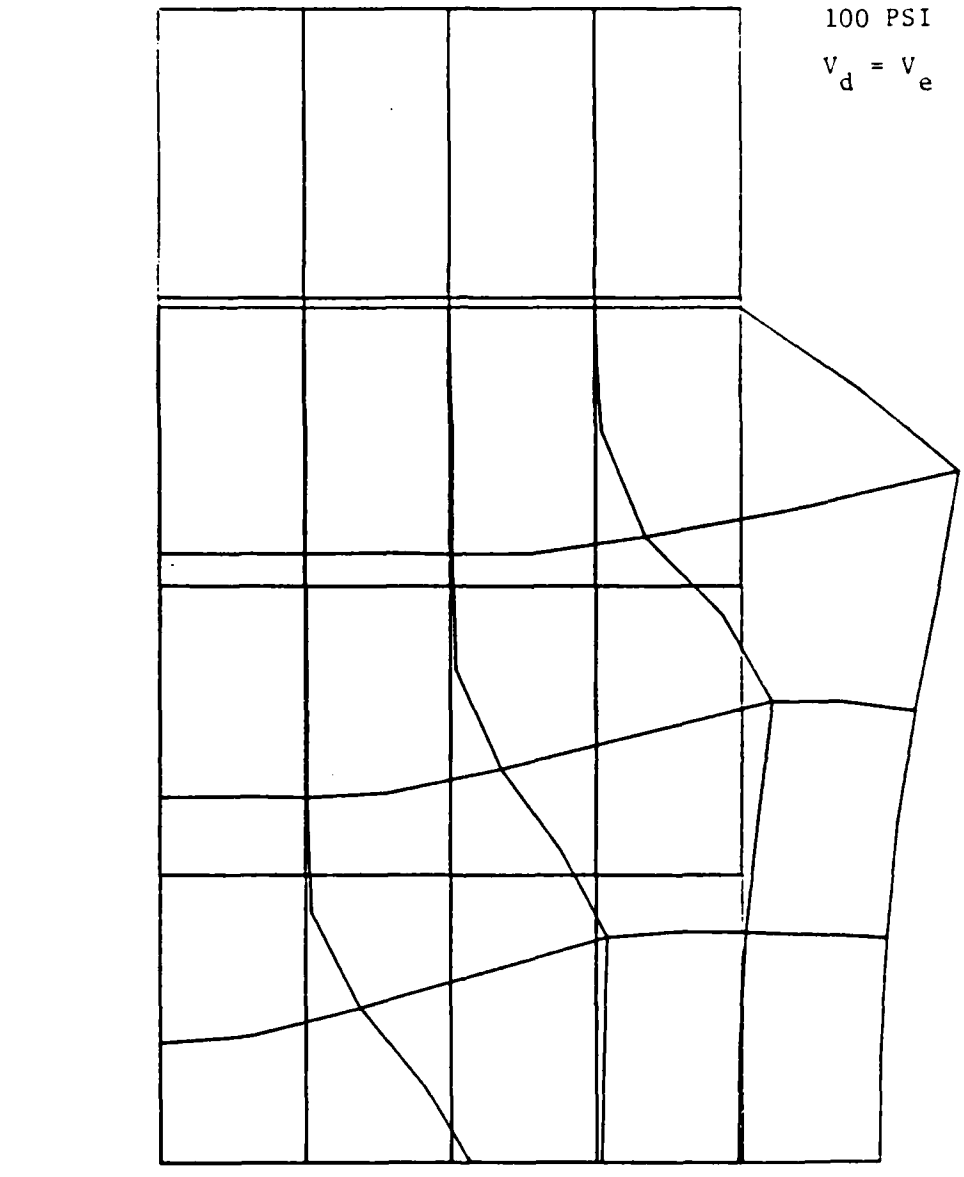

Fig 5-2-b Deformed shape (strategy S3C)

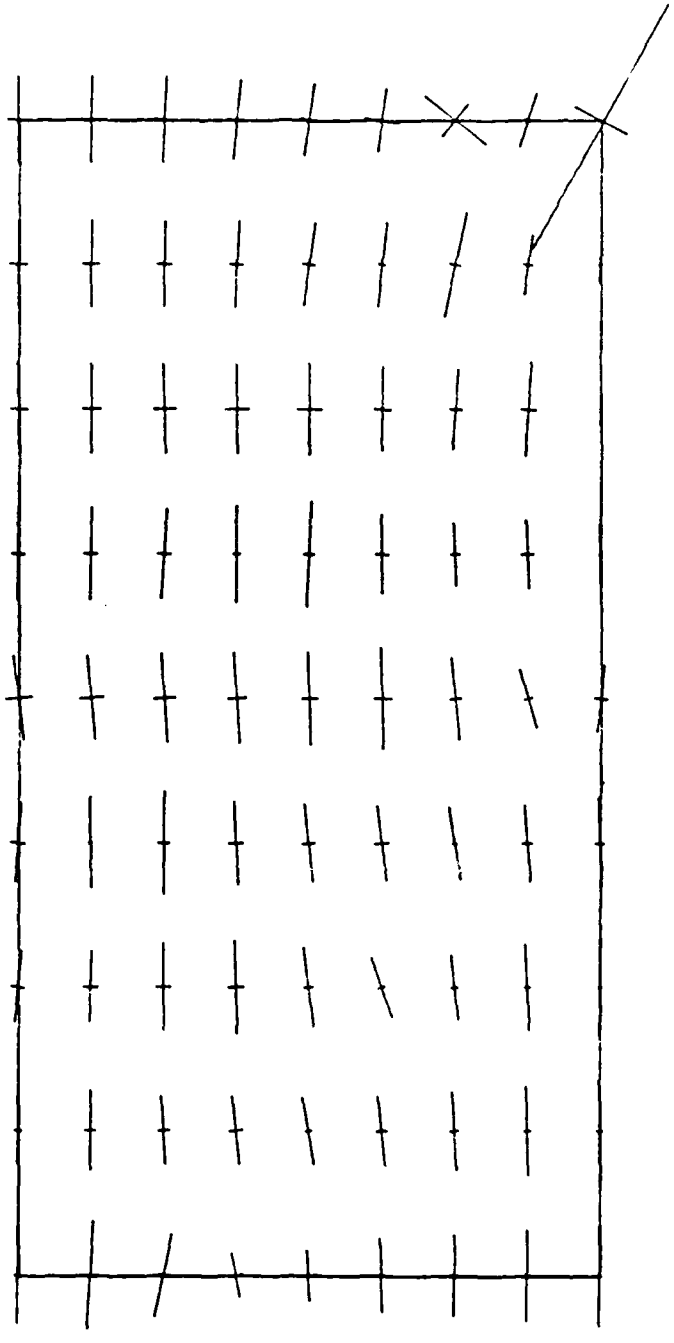

Fig 5-2-c Principal stress distribution (strategy S3C)

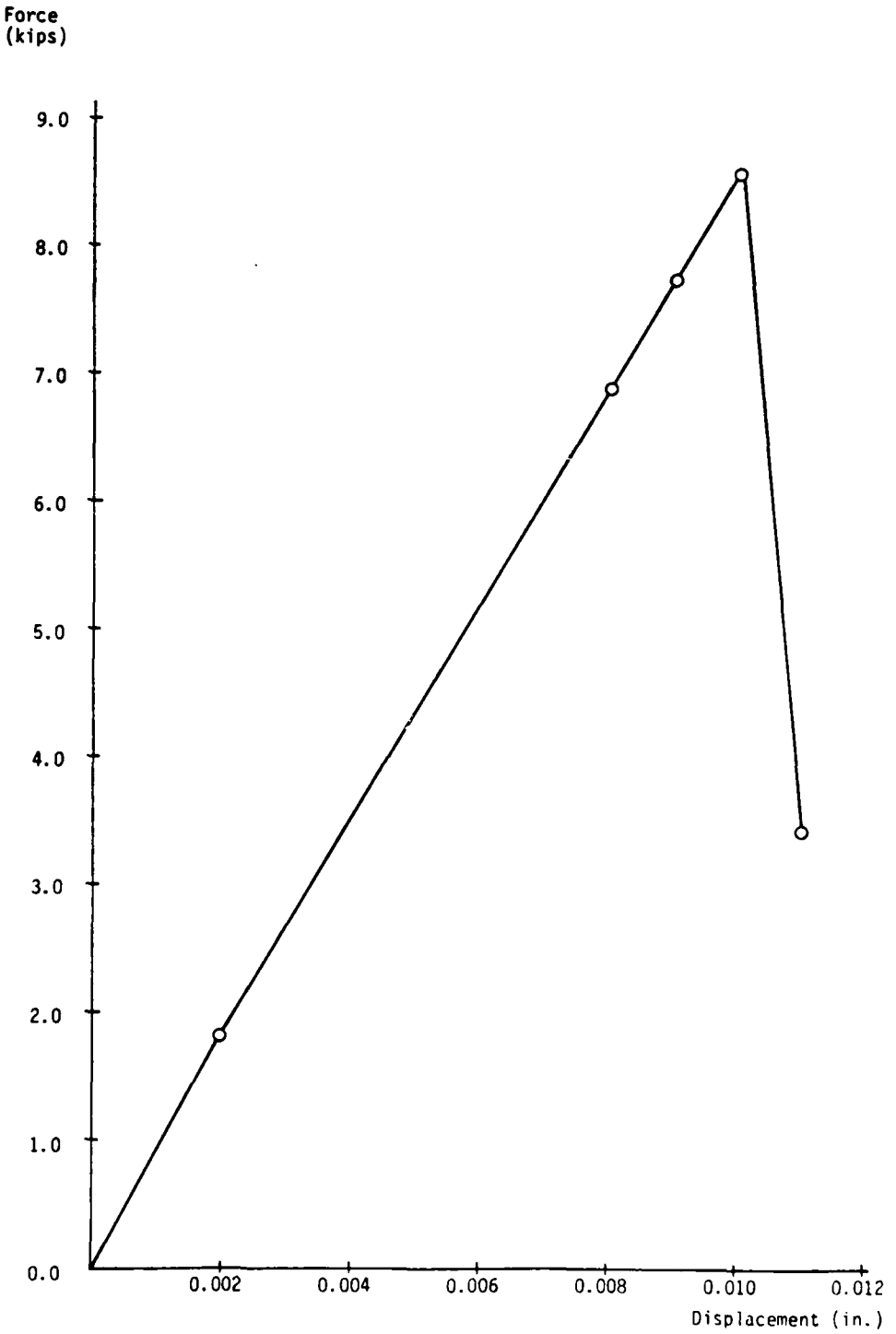

Fig 5-3-a Force-displacement response curve for strategy SMC

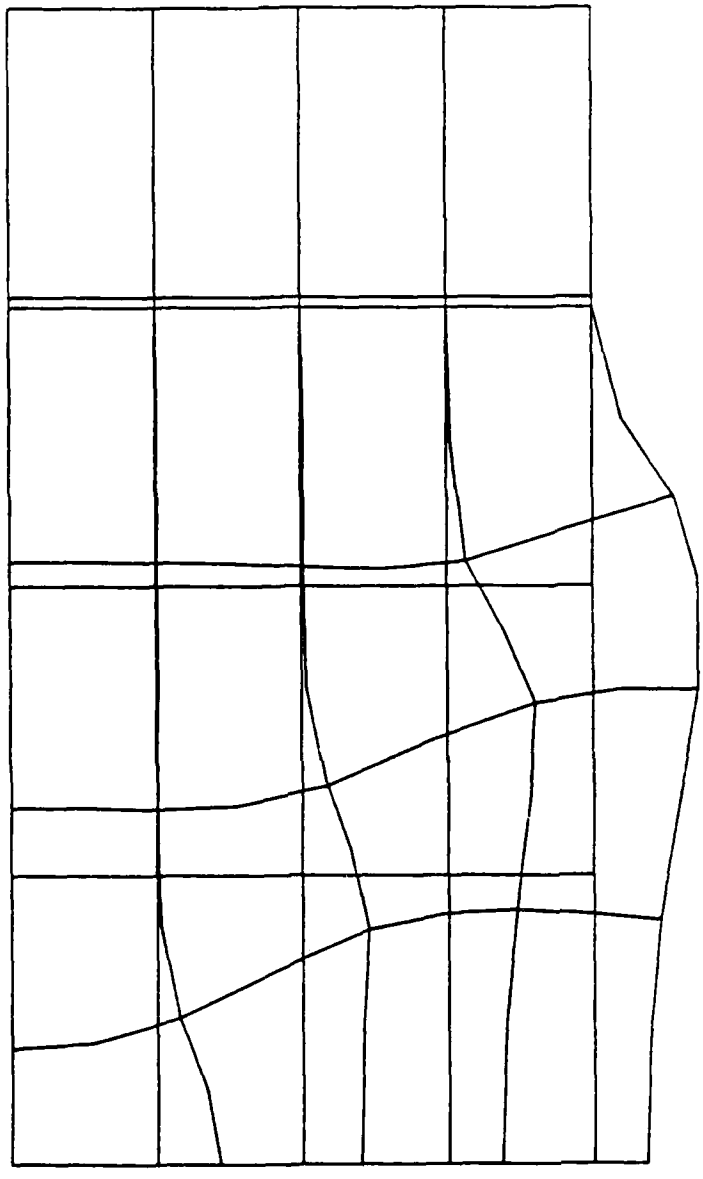

Fig 5-3-b Deformed shape (strategy SMC)

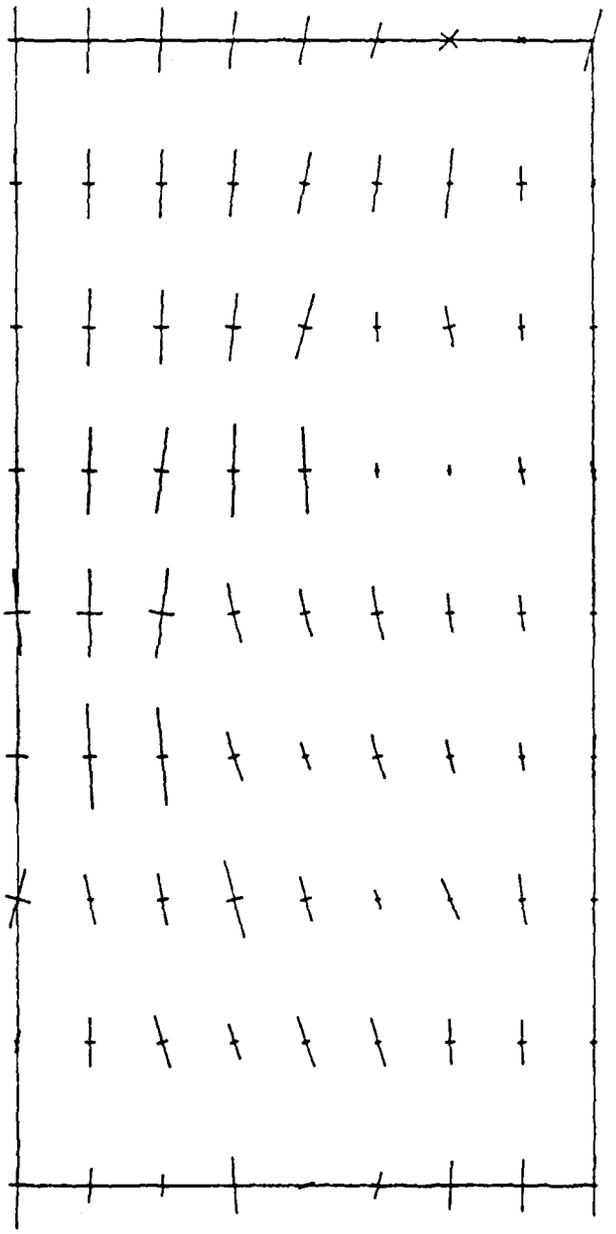

LOAD STEP NO. 8

..... EQUALS 2 KSI TEN.

——— EQUALS 2 KSI COMP.

Fig 5-3-c Principal stress distribution (strategy SMC)

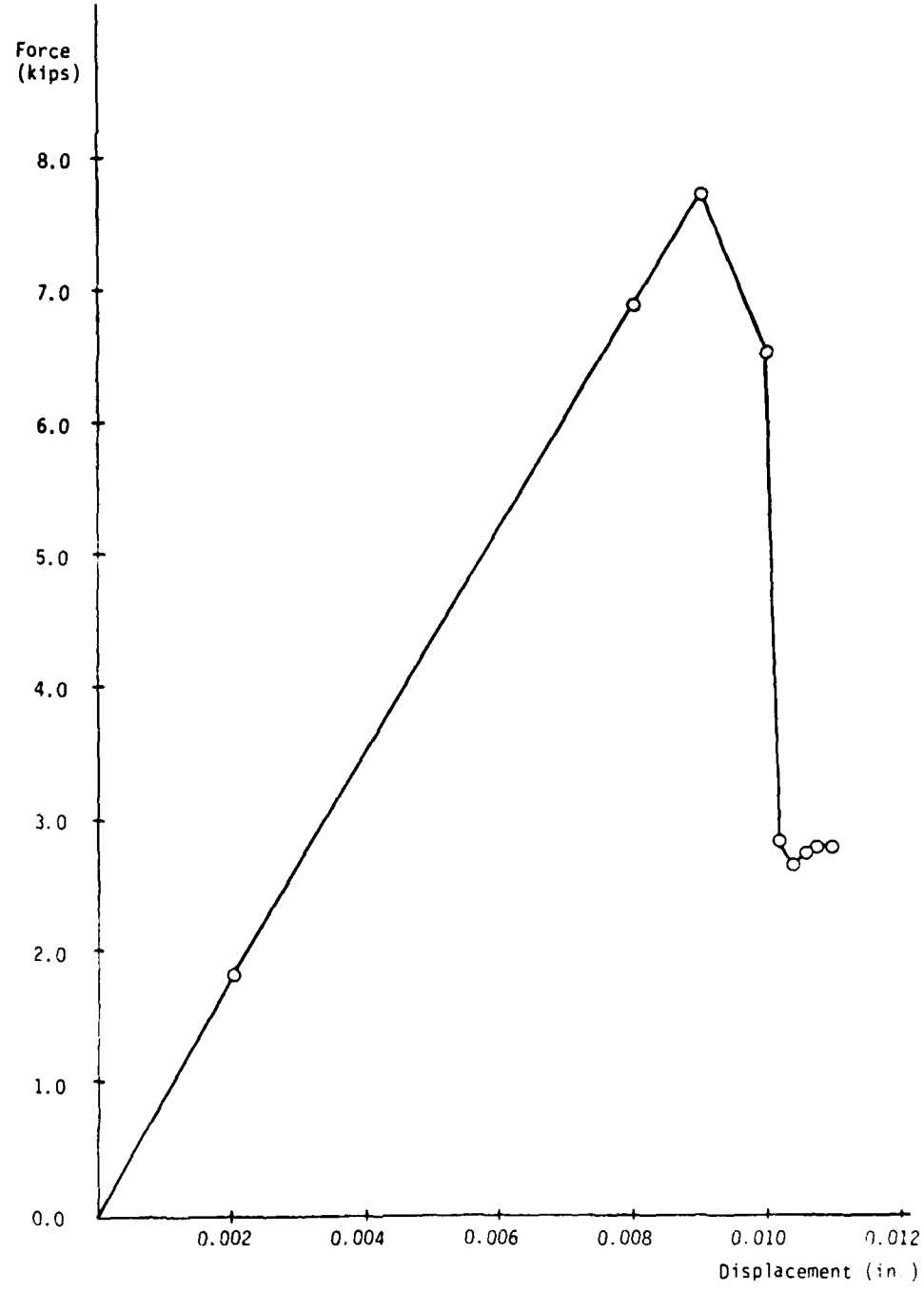

Fig 5-4-a Force-displacement response curve for strategy SNC

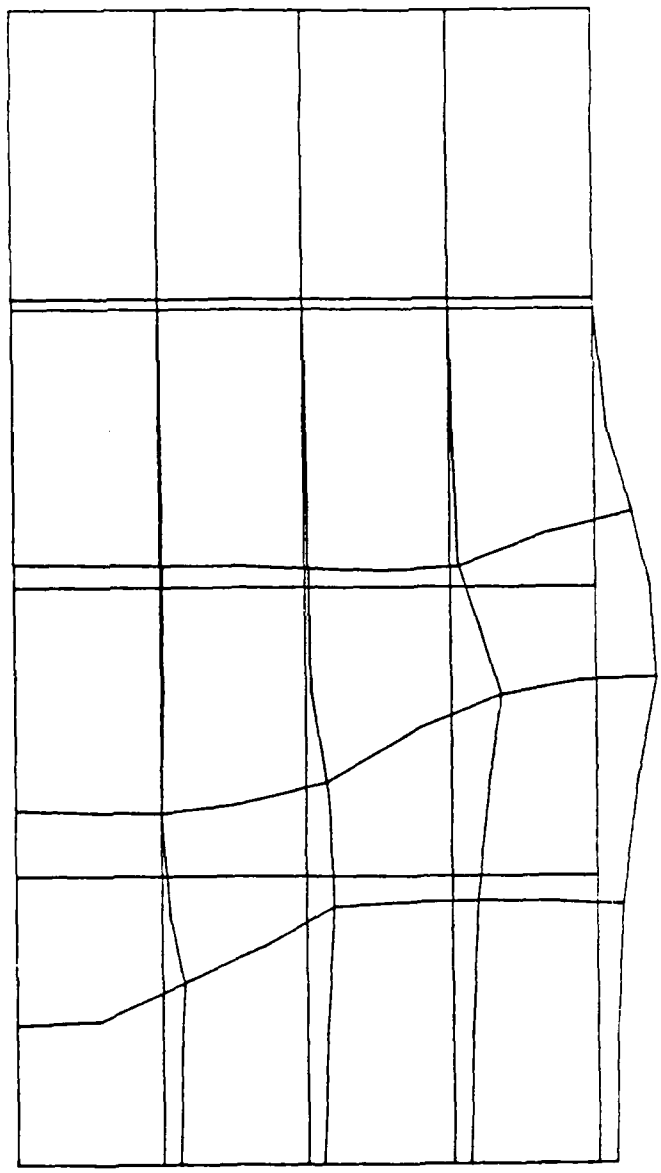

100 PSI

$V_d = V_e$

LOAD STEP NO. 8 ——— = 2.E-1 INCHES GEOM.

——————————— = 1.E-2 INCHES DISP.

Fig 5-4-b Deformed shape (strategy SNC)

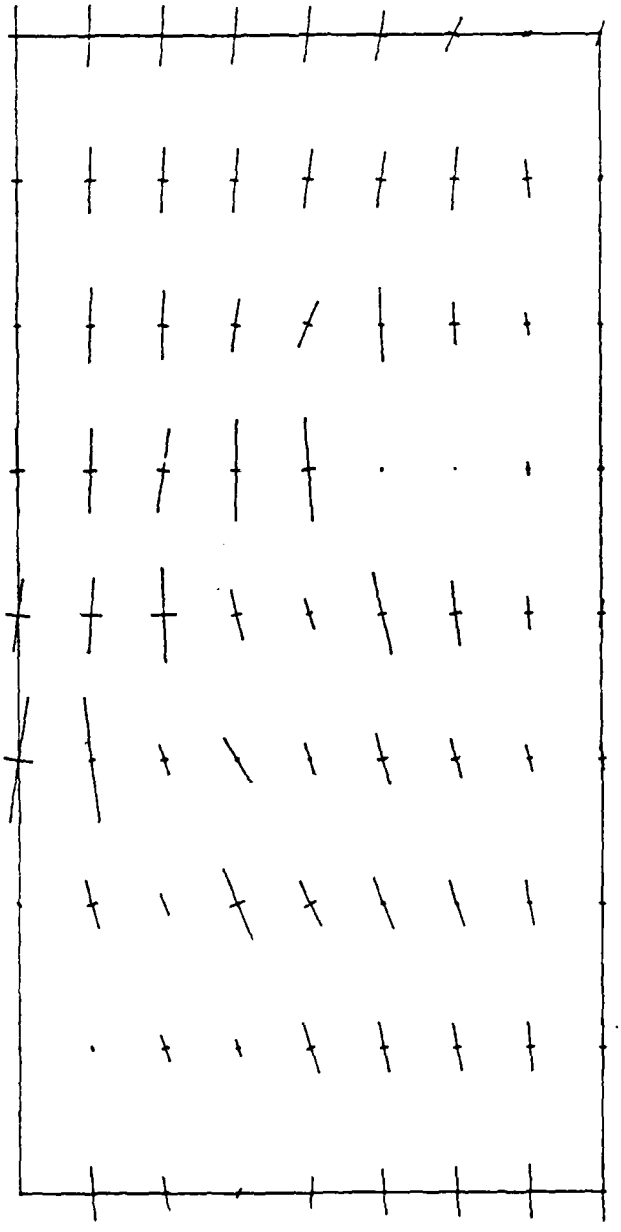

Fig 5-4-c Principal stress distribution (strategy SNC)

range as predicted by the four different strategies respectively.

As expected, strategies S3C and SMC led to the largest total volume changes, as they involve relatively large increments of major principal stress during fracture. Plots of the principal stresses indicate different resulting load transfer mechanisms. It should be noted, however, that the plots of principal stresses correspond to the point on the softening branch in overall load/displacement diagram with unstable fracture propagation still present. (Not all material points comply to the instantaneous fracture surface, as convergence within the load step was not reached in the adopted number of maximum iterations.)

The convergence properties of different shear stress transfer strategies are illustrated on Fig. 5-5-a,b,c,d where the change of error norm during iteration cycles within various load steps is shown. The numerical procedure within each load step allowed for a maximum of twenty iterations within this study and if convergence criterion was not reached, the remaining "defect" was included in the next load step.

The apparent divergence in terms of the global convergence criterion within successive iterations stems from the fact that the violation of the fracture surface on one material point leads to the stress redistribution increments, which may in turn induce the violation of the fracture surface on some other point. Gradual convergence is always present, if no new violations of fracture surface are initiated due to the stress redistribution increments.

As a conclusion of this preliminary investigation, the SMC strategy was chosen for transfering excess shear stress for the subsequent calibration studies and prediction analyses. This strategy corresponds to no volume change during shear slip and shows the least "noisy"

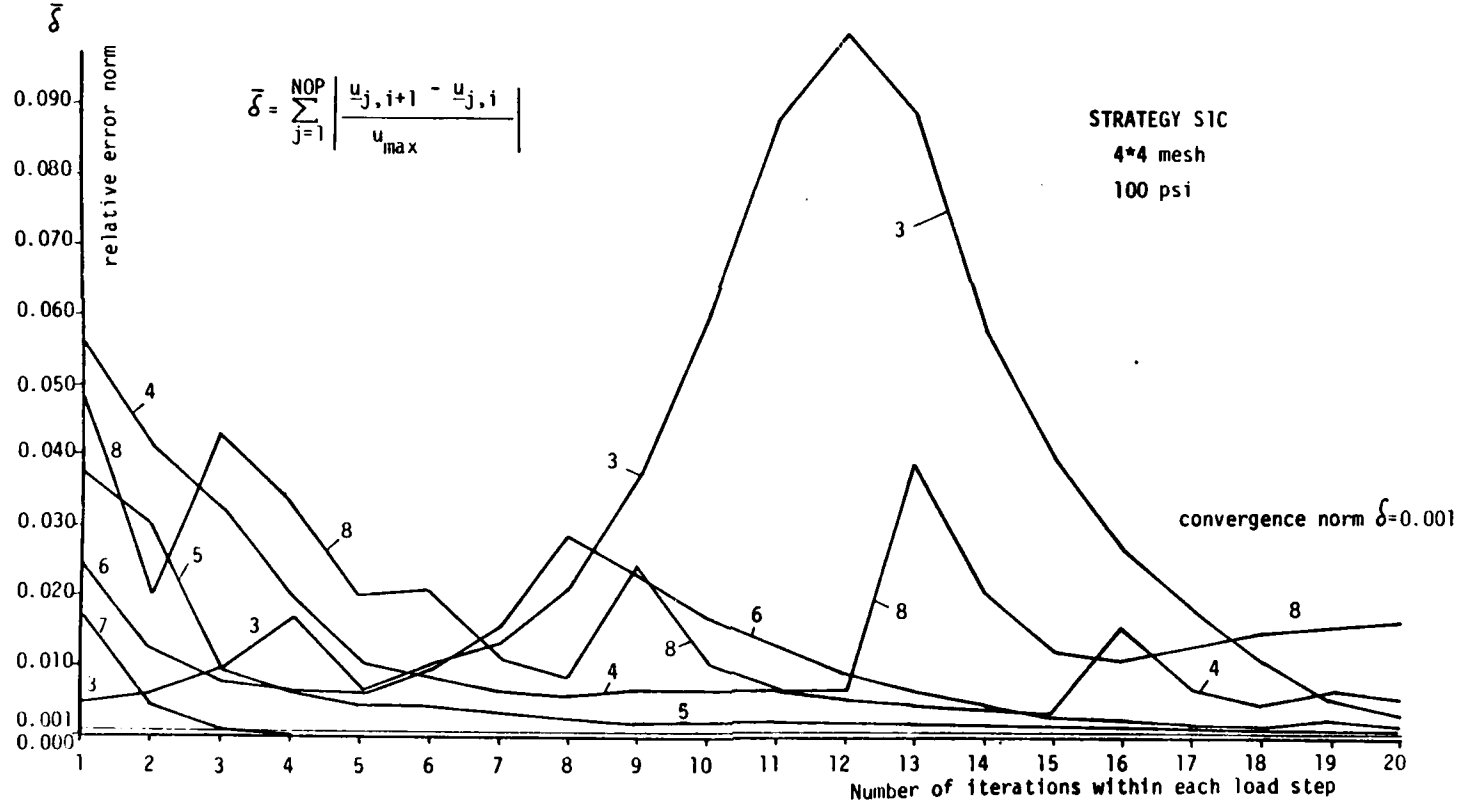

Fig 5-5-a Change of the relative error norm within iterations (strategy S1C)

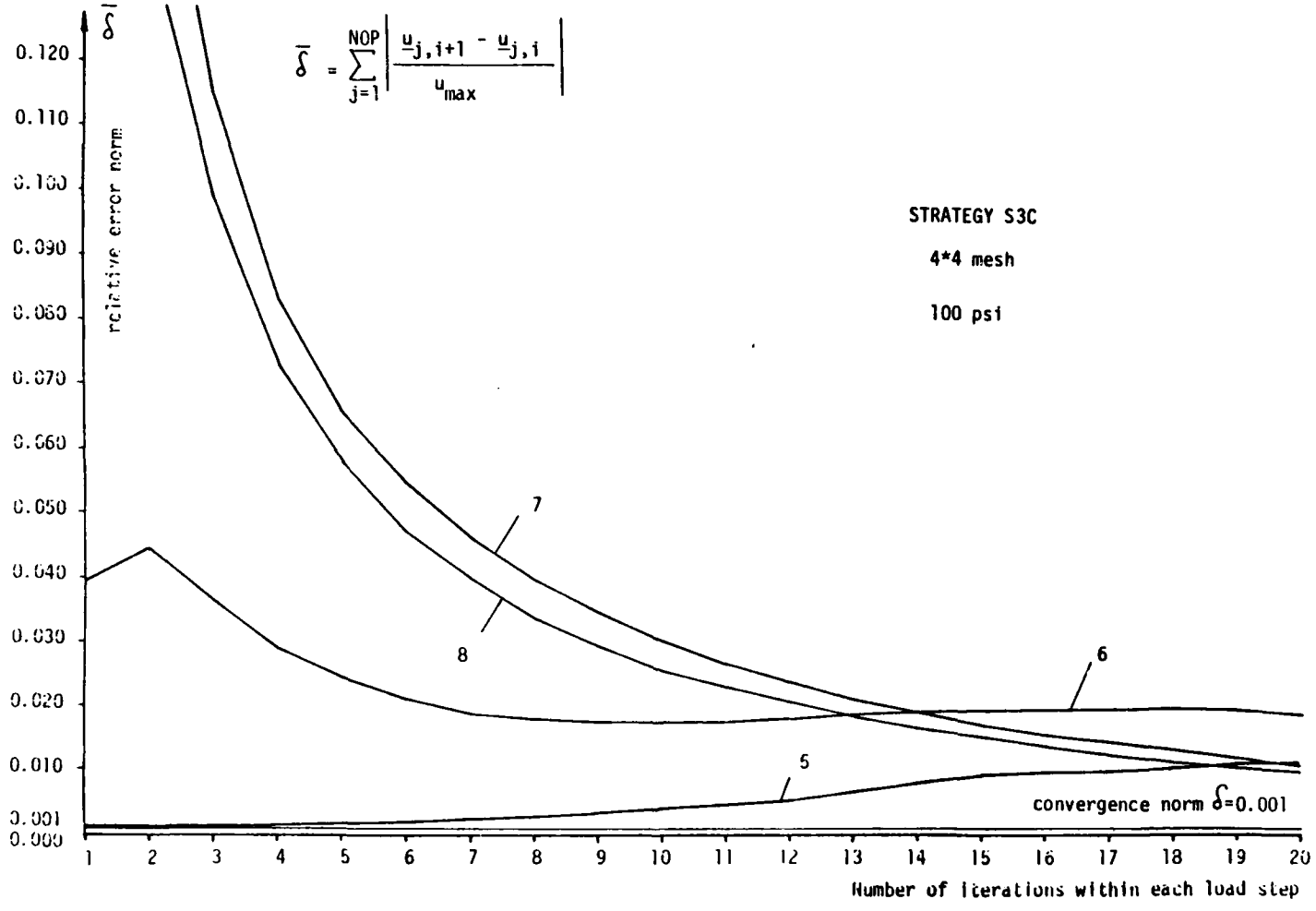

Fig 5-5-b Change of the relative error norm within iterations (strategy S3C)

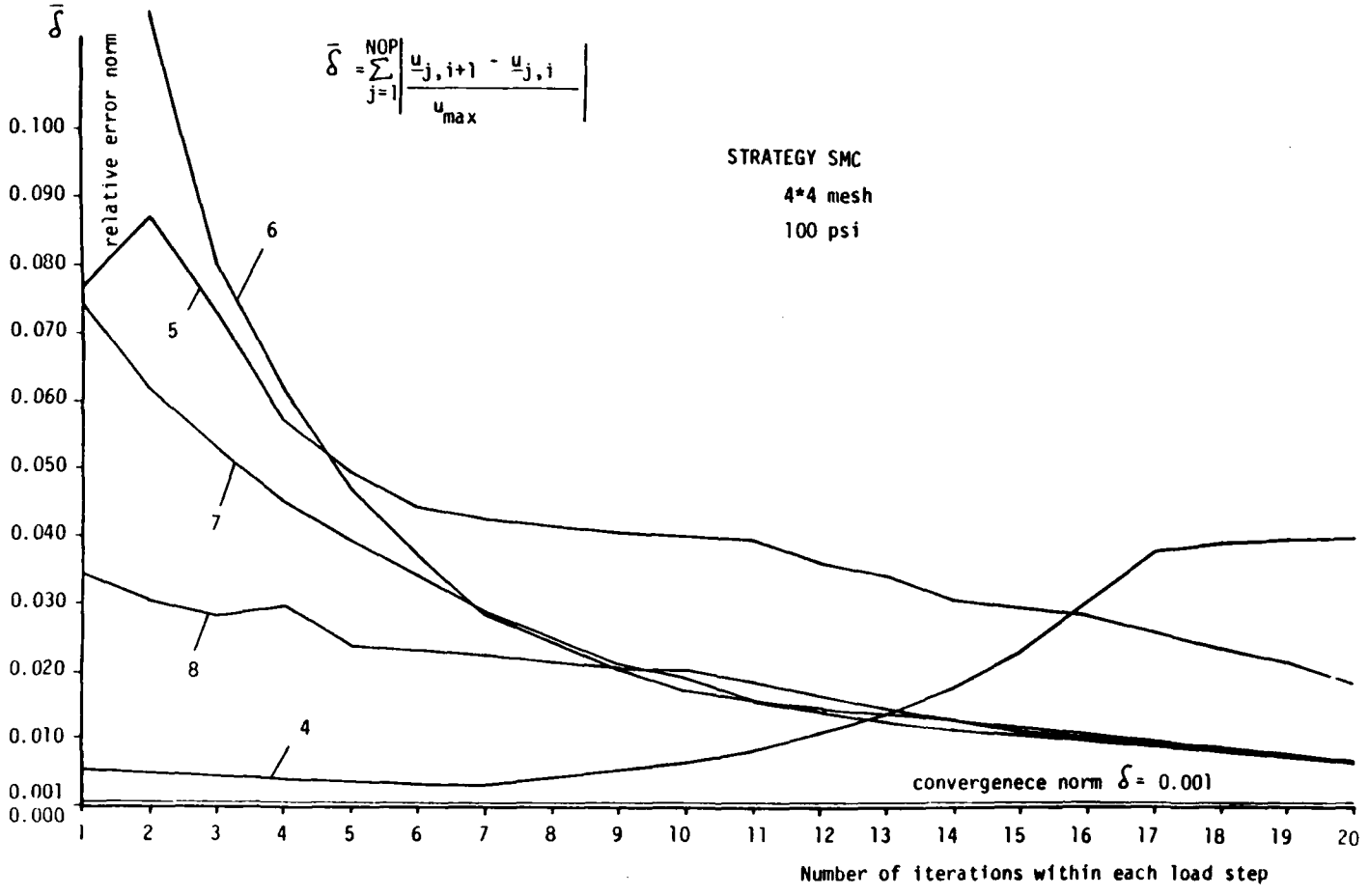

Fig 5-5-c Change of the relative error norm within iterations (strategy SMC)

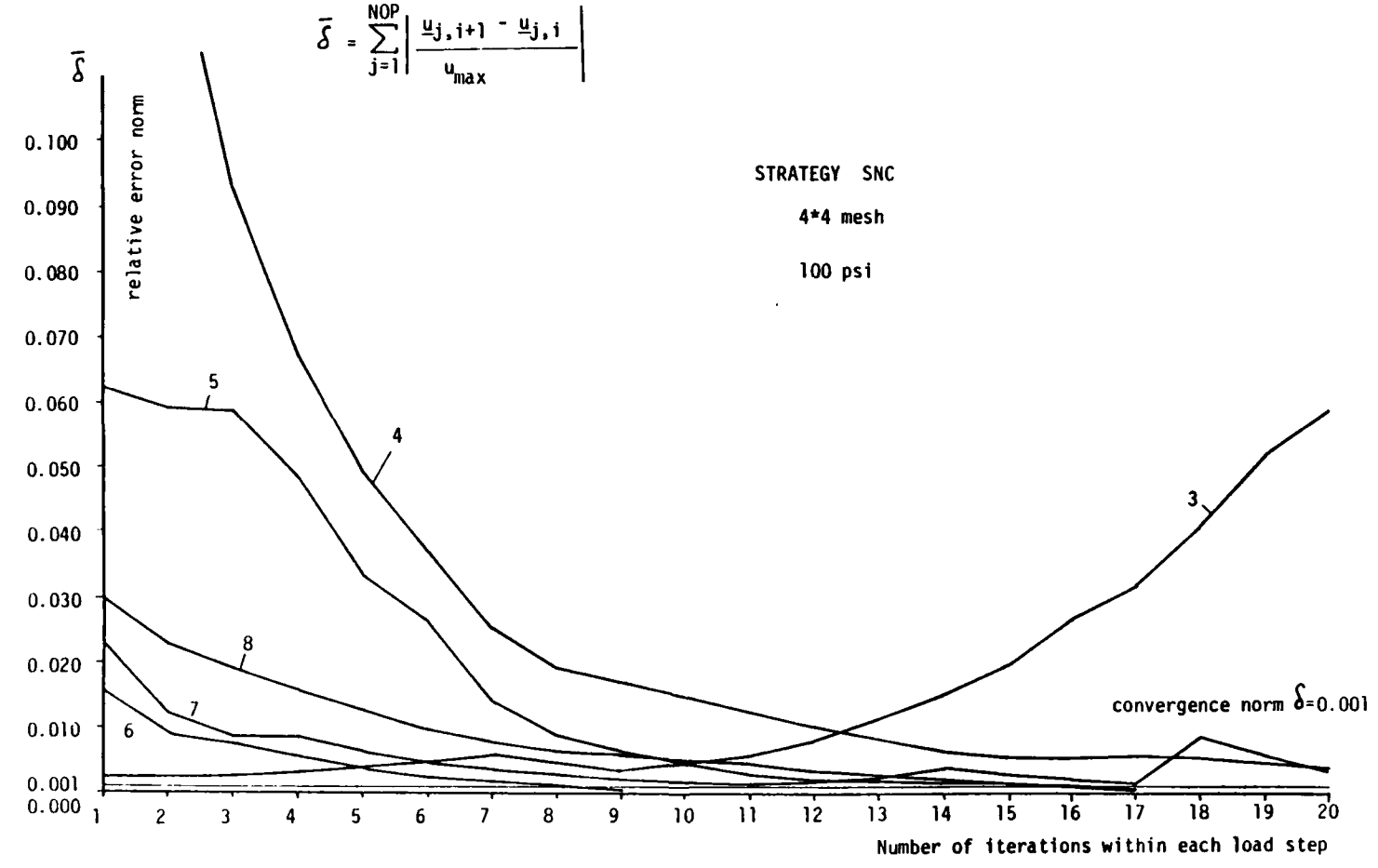

Fig 5-5-d Change of the relative error norm within iterations (strategy SNC)

oscillations of the convergence norm during iterations within the softening range.

5.2 Calibration of the Shear Localization Parameter d_s

The finite element 4 * 4 mesh was adopted for the calibration study of d_s. First, limiting cases of $V_d \approx 0.5\ V_t$ corresponding to ductile response and $V_d = V_t$ corresponding to brittle response behavior have been analyzed for three different confining pressures, 0, 0.69 and 3.45 MPa (0, 100 and 500 psi.). This "bracketing" results, when compared with the experimental results, indicated that V_d should be a function of confining pressure in order to capture the ductile response for highly confined situations and brittle behavior under low or no confinement. Fig 5-6 illustrates the limiting bracketing responses for the three different confining pressures, where V_d was kept constant throughout the analysis.

Starting point for the calibration of the damage localization function $\phi_s(\sigma_m)$ (variation of the damage localization volume as a function of mean stress) is the choice of mean stress level corresponding to ductile post peak behavior σ_{m2}. The value of

$$\sigma_{m_2} = 1.50 \text{ ksi}$$

was chosen, because of the continuous hardening behavior of all triaxial test specimens with confining pressure larger than $\sigma_c > 250$ psi.

Four different damage localization functions, illustrated in Fig. 5-7, were used for the response predictions shown in Fig. 5-8a,b,c,d.

In these four cases, the mean stress level corresponding to brittle post-peak behavior σ_{m1} has been set to 0.0, 6.90, 13.80 and 20.70 MPa

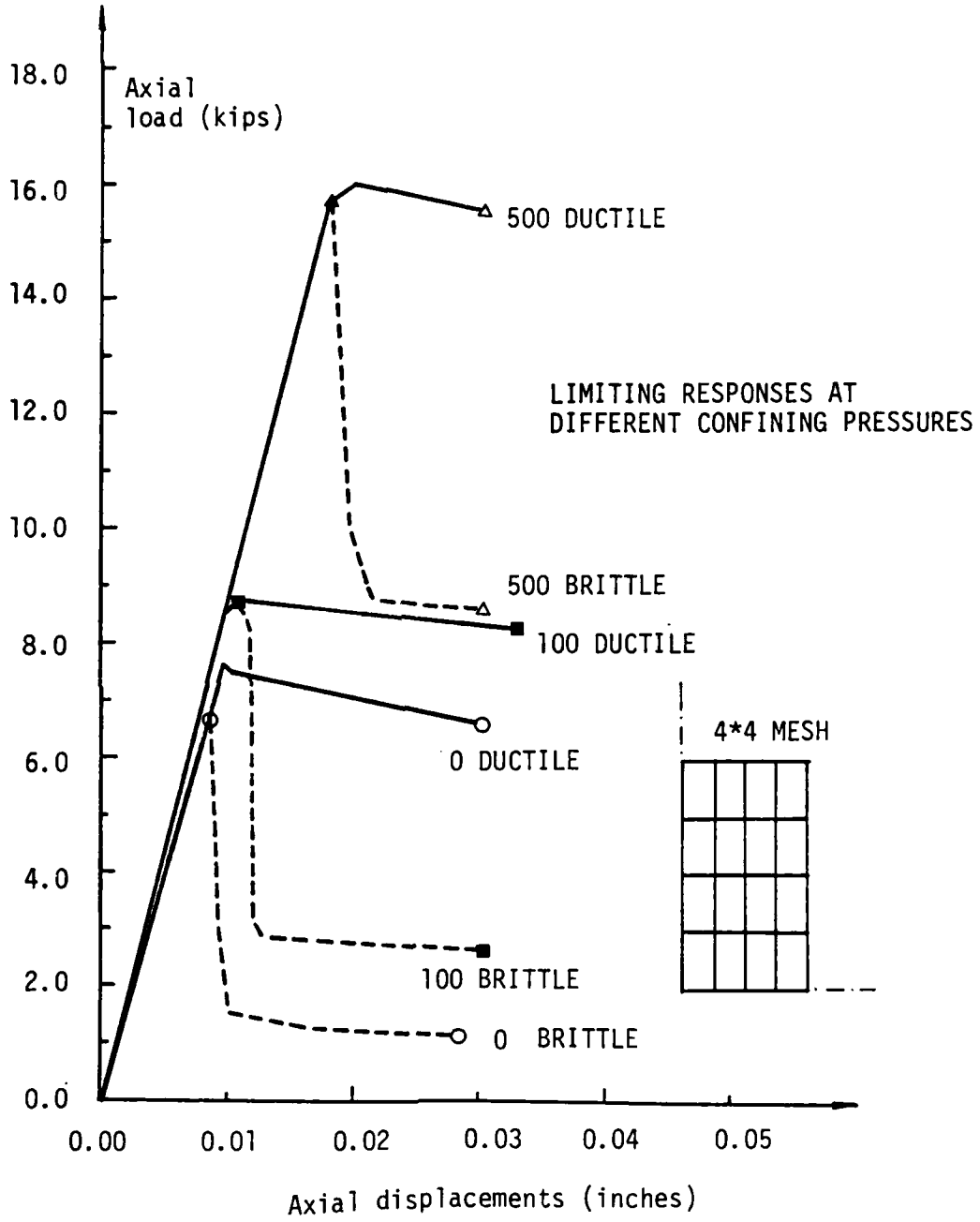

Fig 5-6 Finite element predictions for limiting responses (ductile and brittle) at different confining pressures

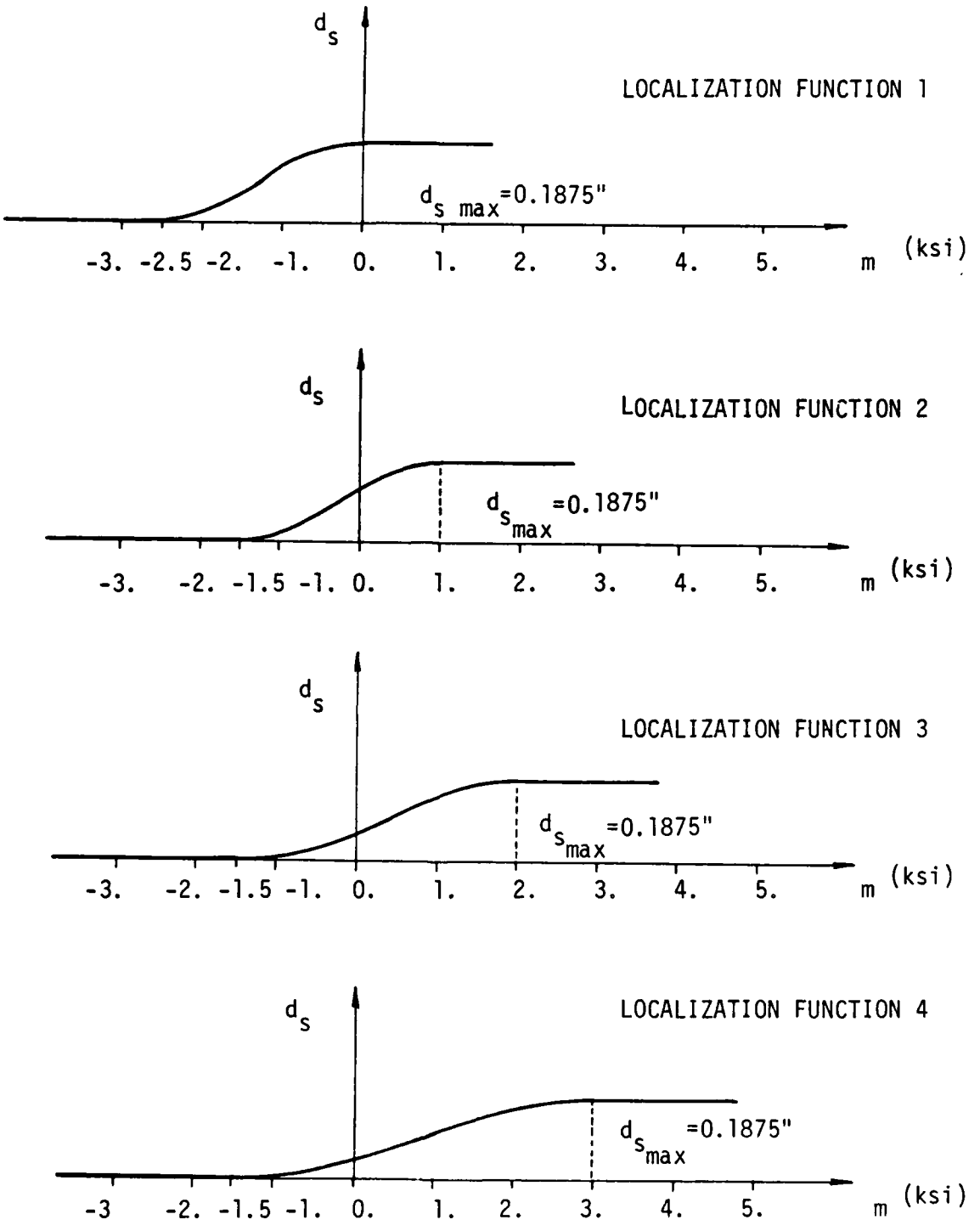

Fig 5-7 Four different shear damage localization functions

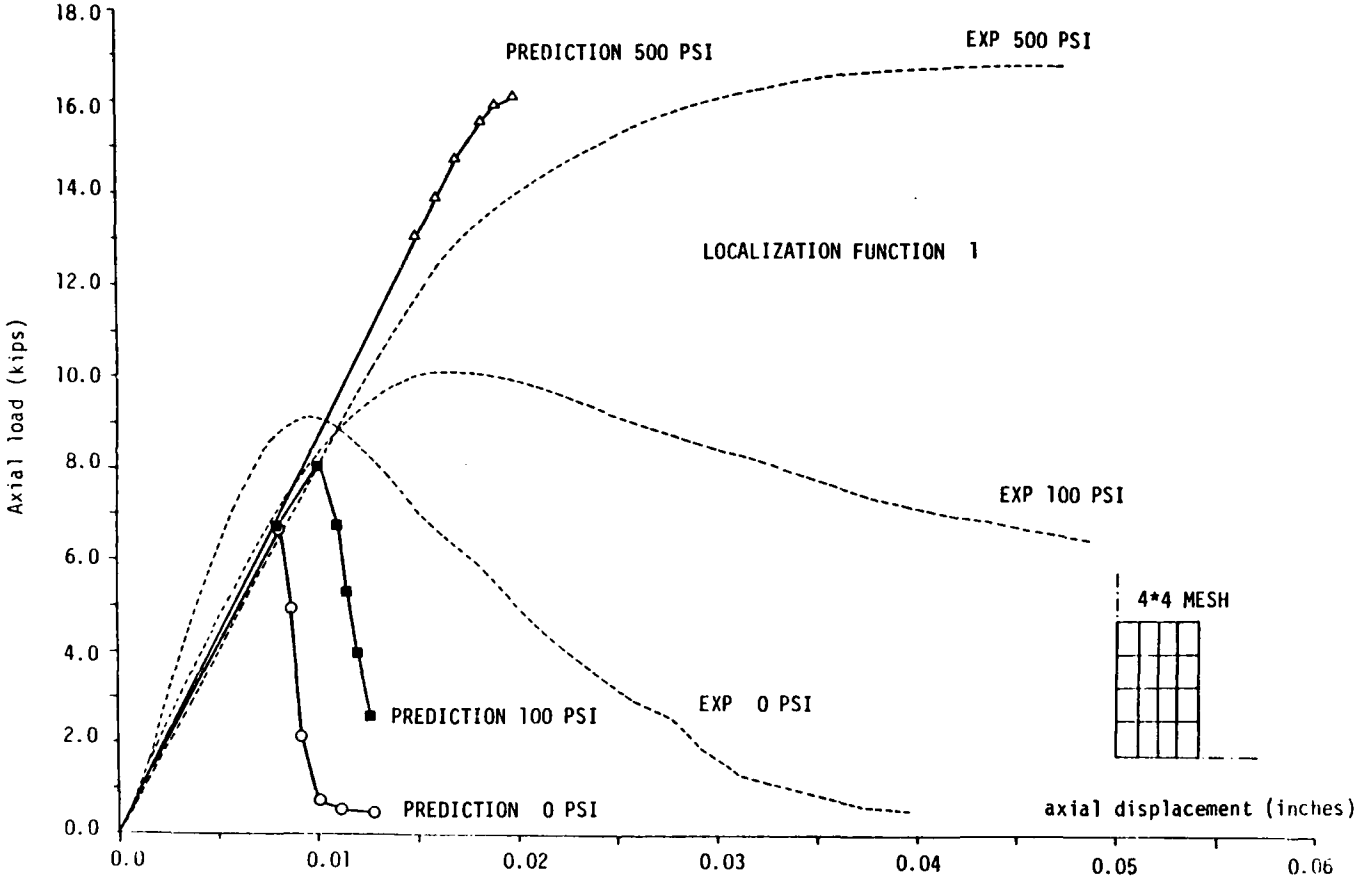

Fig 5-8-a Prediction analyses for compression test (localization function 1)

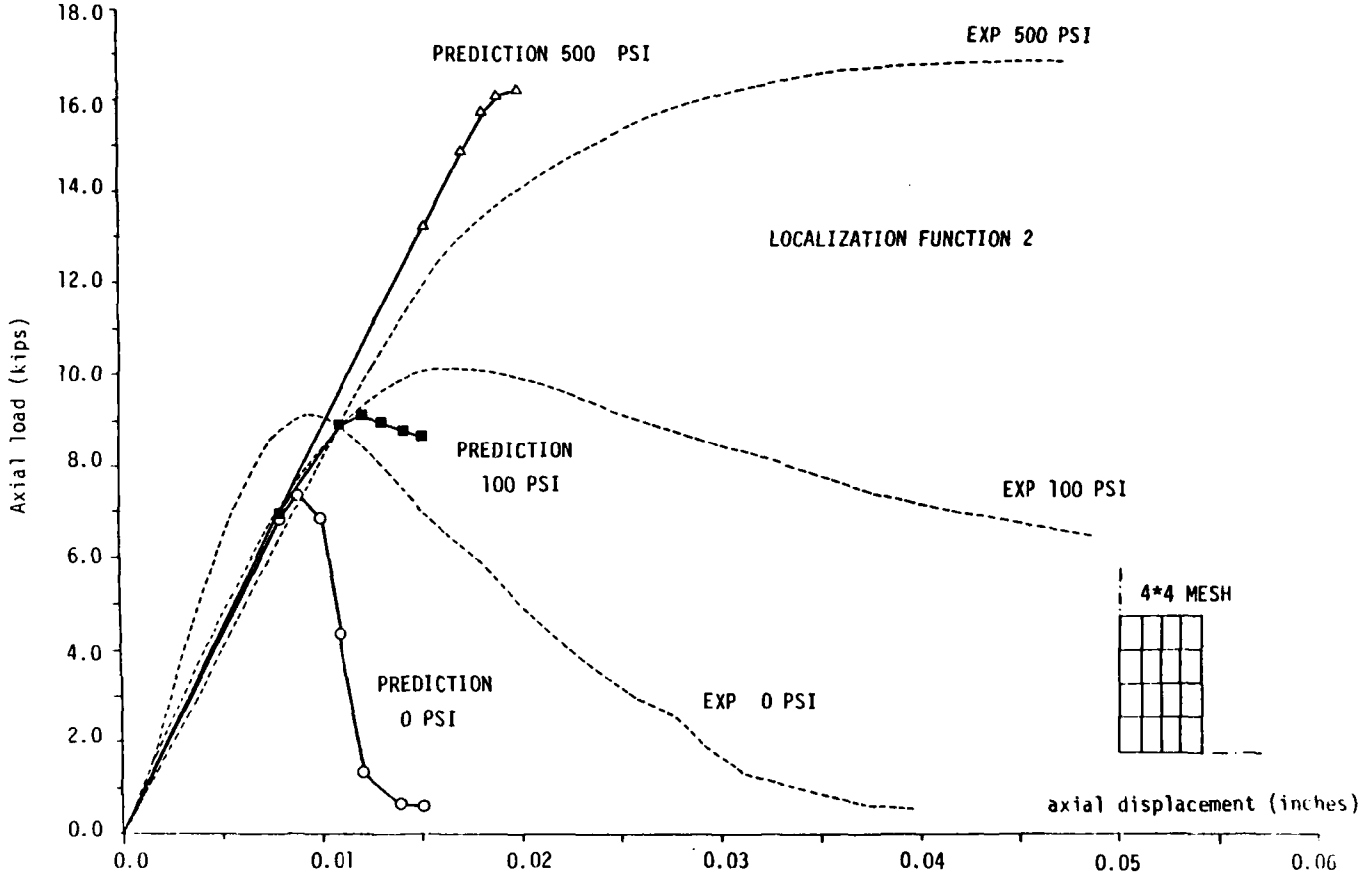

Fig 5-8-b Prediction analyses for compression test (localization function 2)

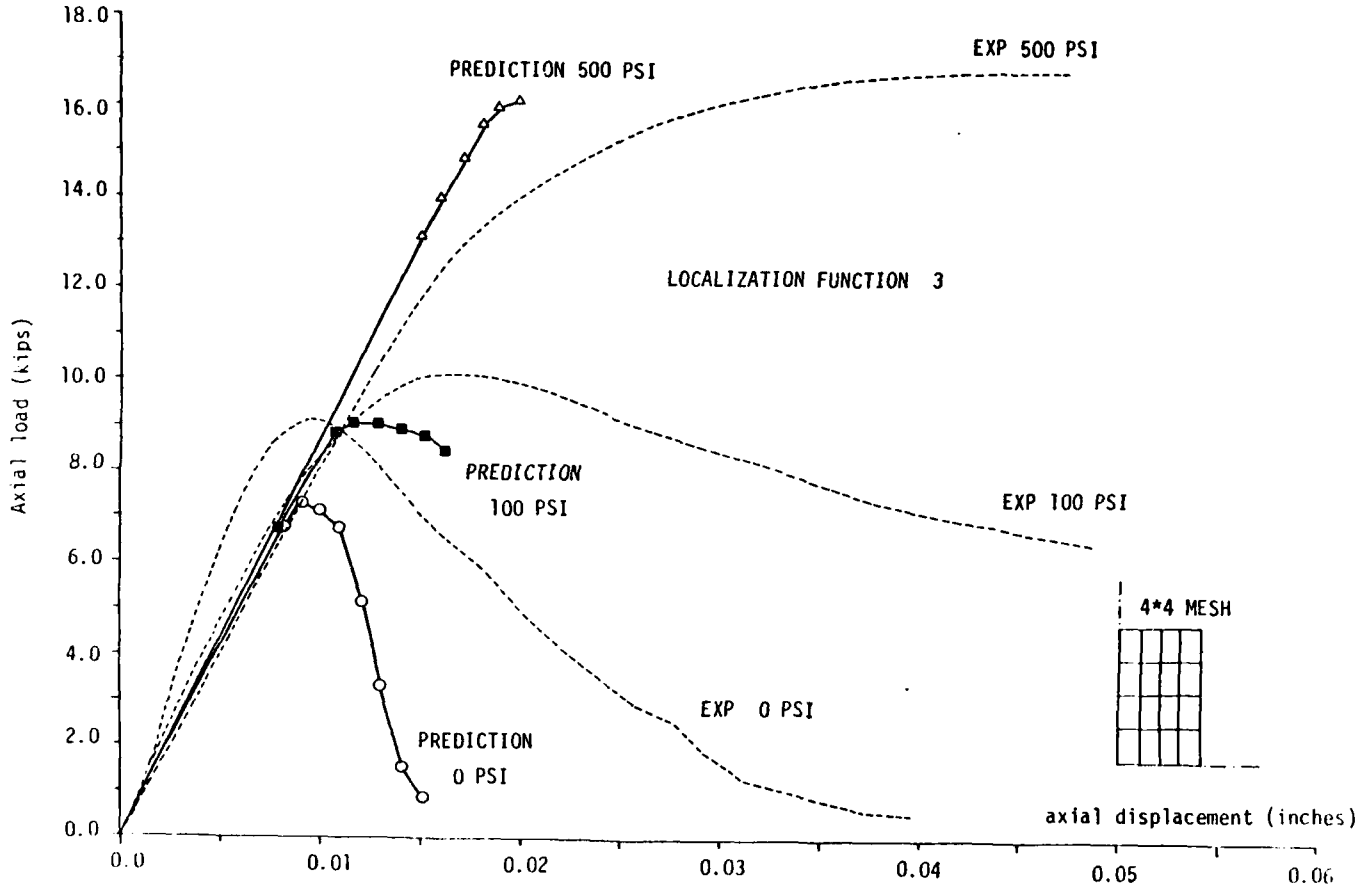

Fig 5-8-c Prediction analyses for compression test (localization function 3)

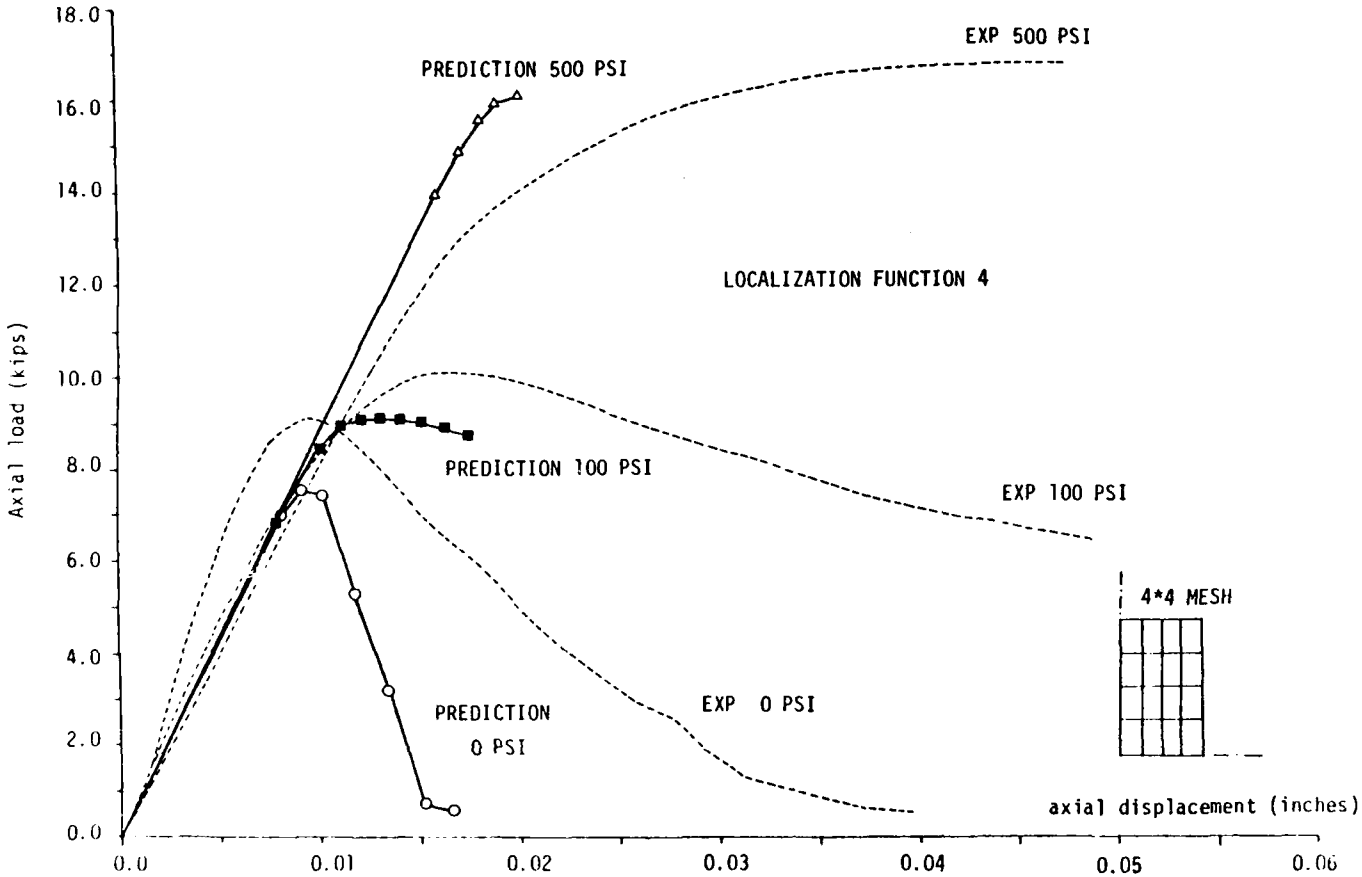

Fig 5-8-d Prediction analyses for compression test (localization function 4)

(0.0, 1.0, 2.0 and 3.0 ksi), and predictions were compared to the experimental results for 0, 100 and 500 psi confining pressures.

The response curves using the damage localization function ϕ_4 (σ_{m_1} = 3.0, σ_{m_2} = -1.5) showed the best agreement with experimental results. Thus ϕ_4 was thereafter used to analyze, the triaxial Hoek cell specimens for other confining pressures (50 and 250 psi).

5.2.1 Mesh Size Effects

To investigate the mesh size effect within this softening formulation, the 4 * 4 finite element mesh predictions for the compression Hoek cell test with confinement 100 psi was adopted as control test problem. The main objective of the investigation was to find out whether the damage volume V_d or damage volume fraction V_d/V_t could be regarded as material property. Table 5.1 summarizes the computational predictions using a coarse 2*2 element mesh and fine 6*6 element mesh. For each case, two different damage volumes were employed, corresponding to constant V_d and constant V_d/V_t fraction.

Fig. 5-9-a illustrates the response curves for all five predictions. The mesh size effect should be studied with reference to the control prediction, 4C. For both coarser and finer mesh subdivisions, the predictions with constant damage volume fraction (i.e. predictions 2CR and 6CR) show considerably better agreement with the control prediction response curve. Only the detailed portions of the response curves are depicted in Fig. 5-9-b to illustrate the nature of softening slope in the overall force/displacement response curve.

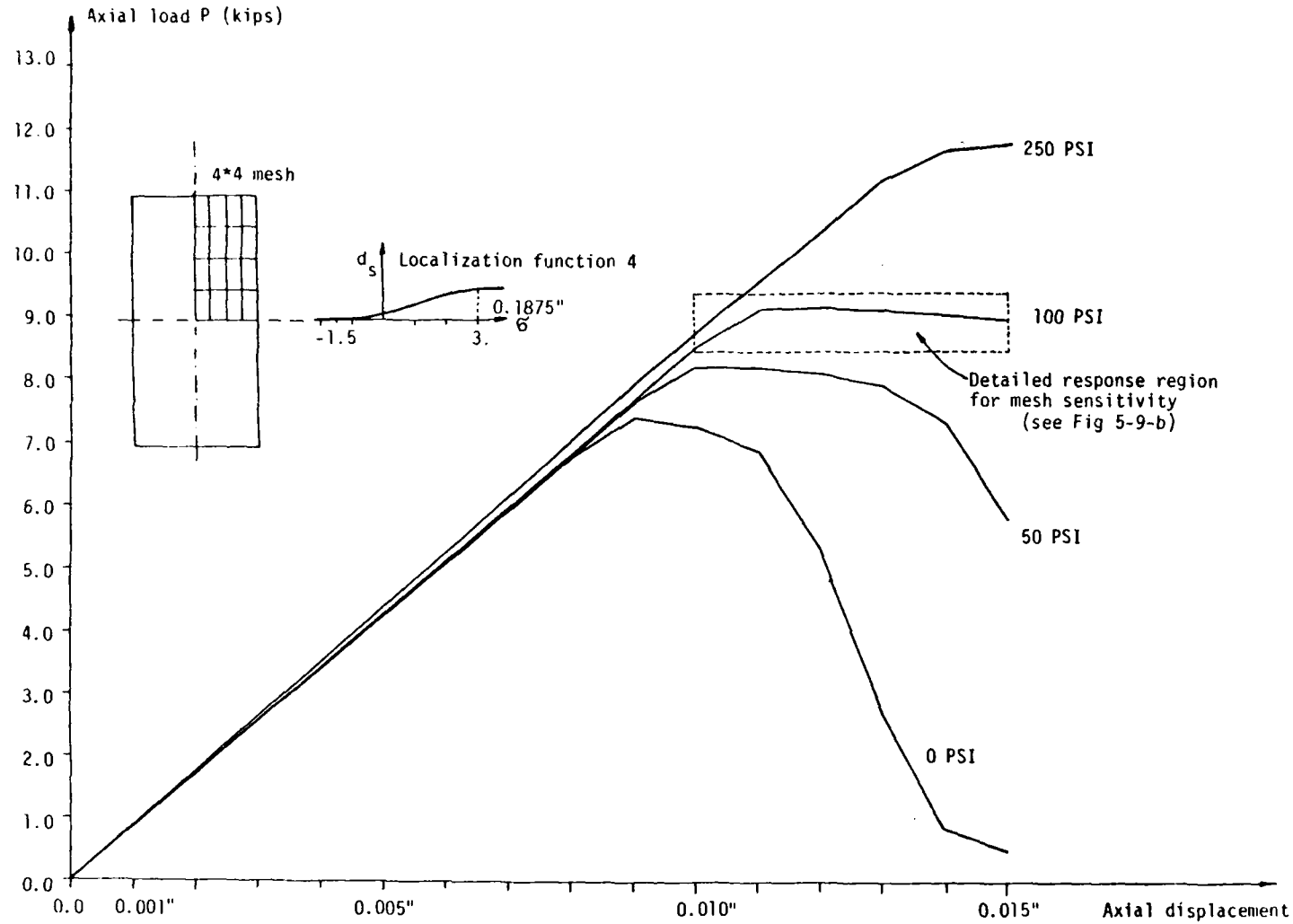

Fig 5-9-a Prediction analyses for compression test (0,50,100 and 250 psi confining pressure) using localization function 4

TABLE 5.1 COMPRESSION TEST PREDICTION ANALYSES TO STUDY MESH SIZE EFFECTS

Mesh Size	Localization Function Parameter			Localization Model	Prediction Label
	σ_{m_1}	σ_{m_2}	$d_{s_{max}}$		
4*4	3.0	-1.5	0.1875	Control test Prediction	4C
2*2	3.0	-1.5	0.1875	Same V_d as control test prediction	2CV
2*2	3.0	-1.5	0.1875	Same V_d/V_t as control test prediction	2CR
6*6	3.0	-1.5	0.1875	Same V_d as control test prediction	6CV
6*6	3.0	-1.5	0.1875	Same V_d/V_t as control test prediction	6CR

Keeping V_d = constant in computational predictions leads to far too brittle response in the case of a fine mesh, and far too ductile response in the case of a coarse mesh.

As a result of this study, a constant damage volume fraction formulation will be adopted for the numerical predictions of direct shear test.

5.3 Calibration of the Tensile Localization Parameter d_t

The procedure used to calibrate the tensile localization parameter d_t follows similar reasoning as the procedure adopted in the calibra-

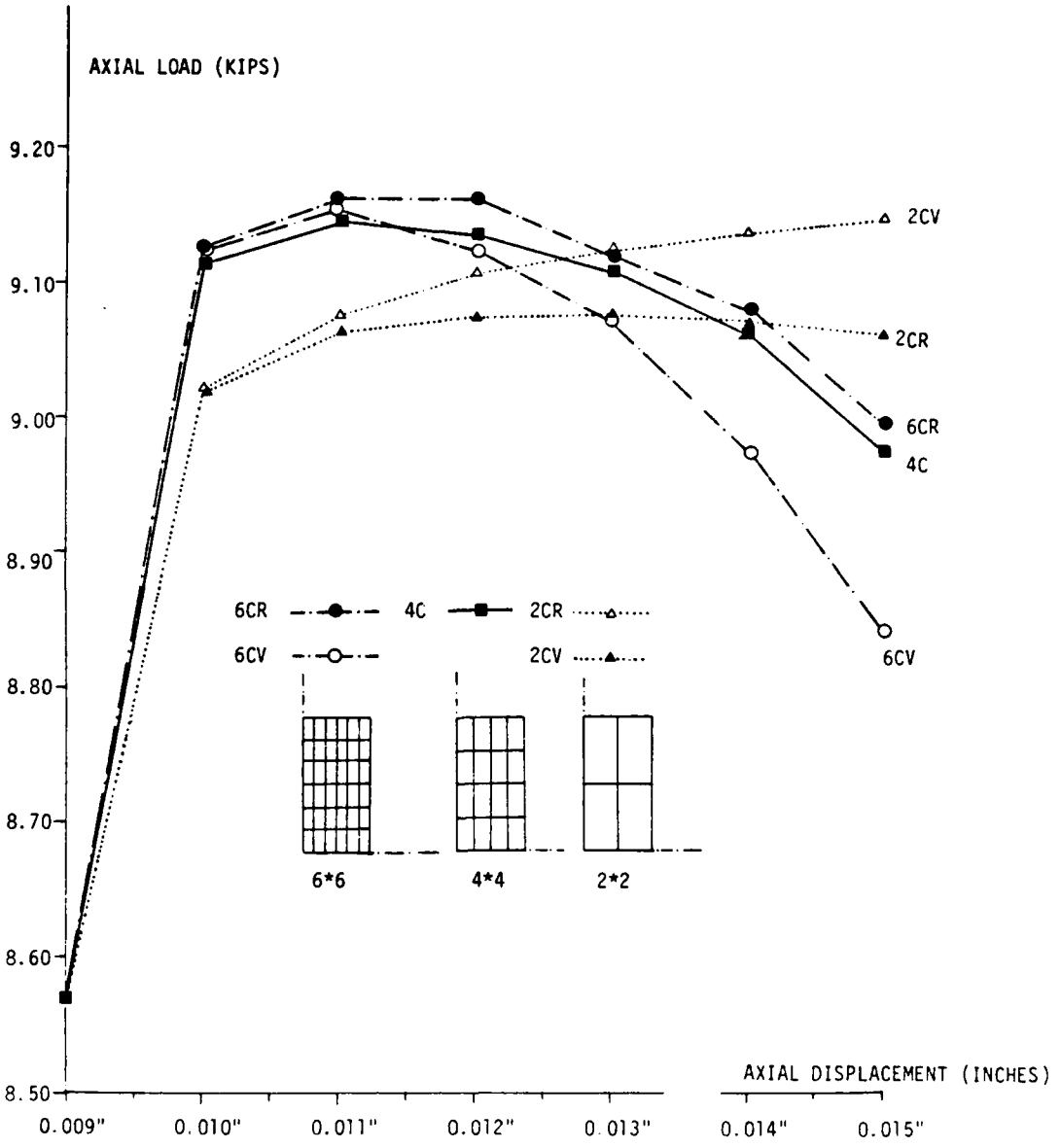

Fig 5-9-b Mesh sensitivity for compression test prediction analyses

tion of shear localization parameter d_s. The medium 4*4 element mesh was again used for the control prediction.

In results similar to the shear localization study, the two bracketing predictions for perfectly ductile and brittle behavior indicated that considerable ductility is present in the tensile post peak response. To start the calibration, the localization function for shear slip was adopted (see Fig. 5-10), but the obtained response was too brittle when compared to the experimental results. After several trials trials the damage localization function $\phi_t(\sigma)$ with $\sigma_{m1} = 3.0$, $\sigma_{m2} = -1.5$ and, $d_{tmax} = 0.09375"$ led to a reasonable reproduction of the post-peak response. Hence this response prediction was further used as softening control curve for the subsequent mesh sensitivity study.

5.3.1 Mesh Size Effects

In completely analogous fashion (Table 5.2) to the triaxial compression tests, predictive analyses were performed using the coarse 2*2 and fine 6*6 mesh, again keeping either V_d or the V_d/V_t fraction equal to the control test prediction for the 4*4 mesh.

Response curves for all five predictions are shown in Fig. 5-11 and support the same conclusion reached for the triaxial compression test study. For both the coarse and the fine mesh, predictions that keep the damage volume fraction $\alpha = V_d/V_t$ constant show better agreement with control response curve labelled 4T.

Again, the predictions using the same V_d as the control test prediction led to the too ductile response curve for the coarse 2*2 mesh and to the too brittle response curve for the fine 6*6 mesh.

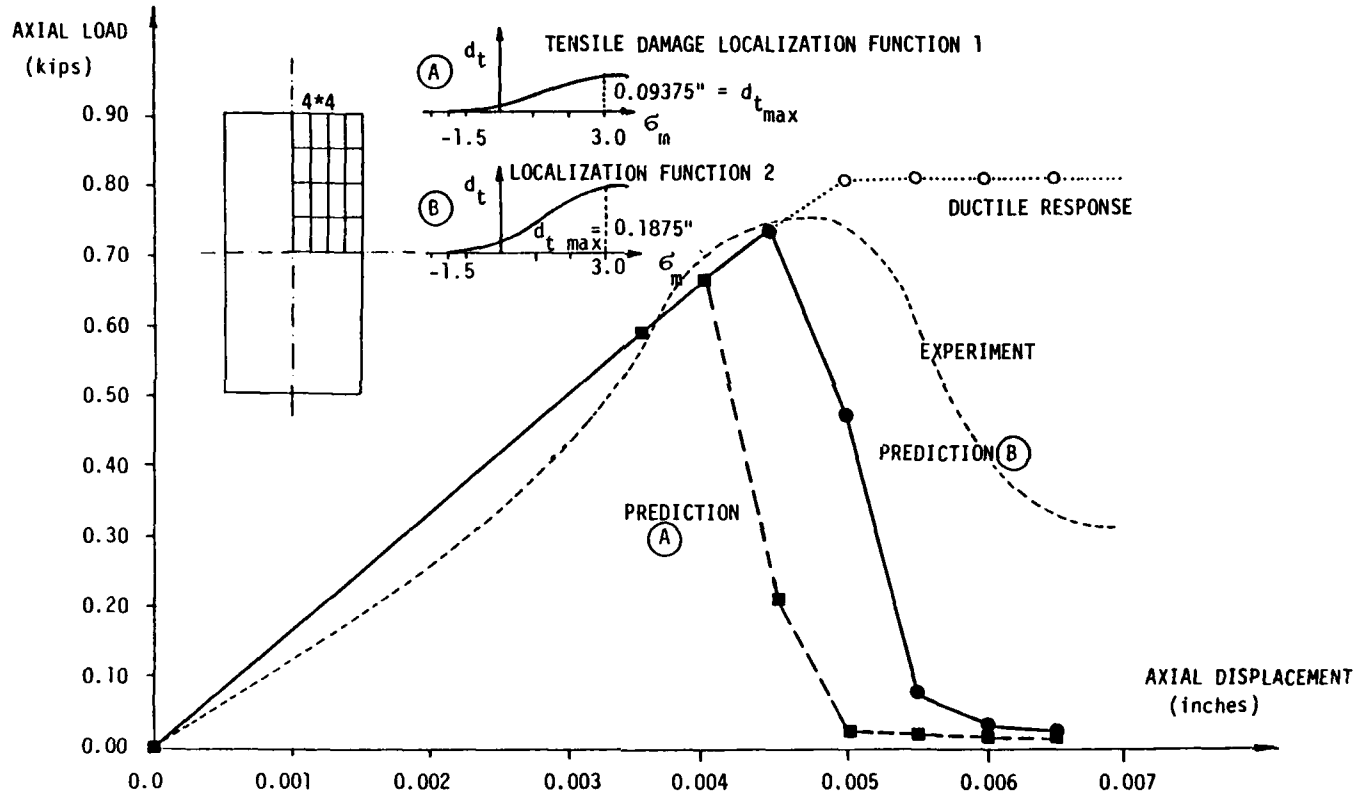

Fig 5-10 Tensile damage localization damage function calibration

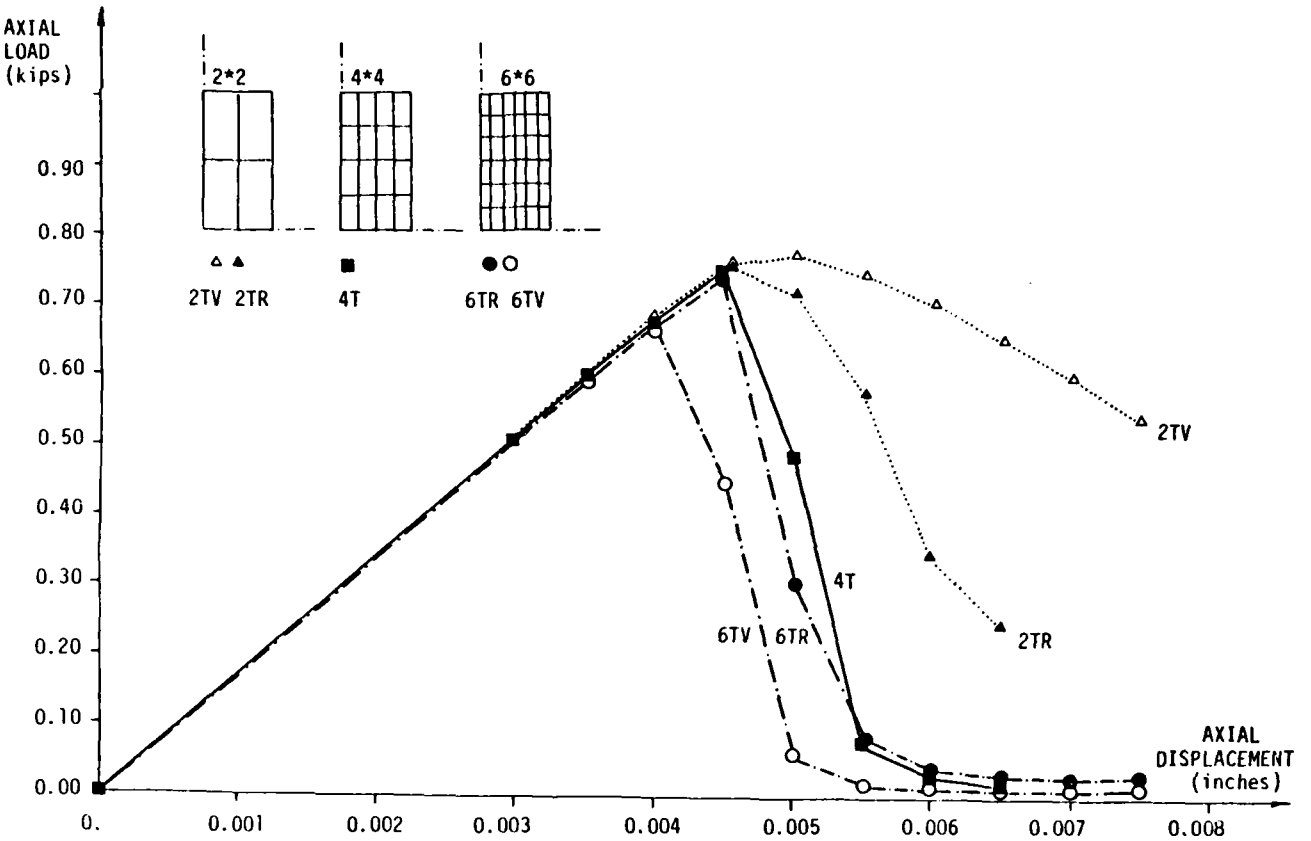

Fig 5-11 Prediction analyses for tension test with mesh sensitivity study

TABLE 5.2 TENSION TEST PREDICTION ANALYSES TO STUDY MESH SIZE EFFECTS

Mesh Size	Localization Function Parameters			Localization Model	Prediction Identification
	σ_{m_1}	σ_{m_2}	d_{tmax}		
4*4	3.0	-1.5	0.09375	Control test Prediction	4T
2*2	3.0	-1.5	0.09375	Same V_d as control test prediction	2TV
2*2	3.0	-1.5	0.09375	Same V_d/V_t as control test prediction	2TR
4*4	3.0	-1.5	0.09375	Same V_d as control test prediction	6TV
4*4	3.0	-1.5	0.09375	Same V_d/V_t as control test prediction	6TR

As a result of this study the constant damage volume fraction formulation will again be adopted for the numerical predictions of the direct shear tests.

5.3.2 Fracture Strain Localization

The overall force displacement response curves do not allow the inspection of possible fracture strain localization, which is exactly the intent of the localized fracture model using the smeared approach.

For that reason, additional information about the fracture strain localization is illustrated in Fig. 5-12 for the tensile control test specimens (4T). Along each of the vertical lines connecting nodes with

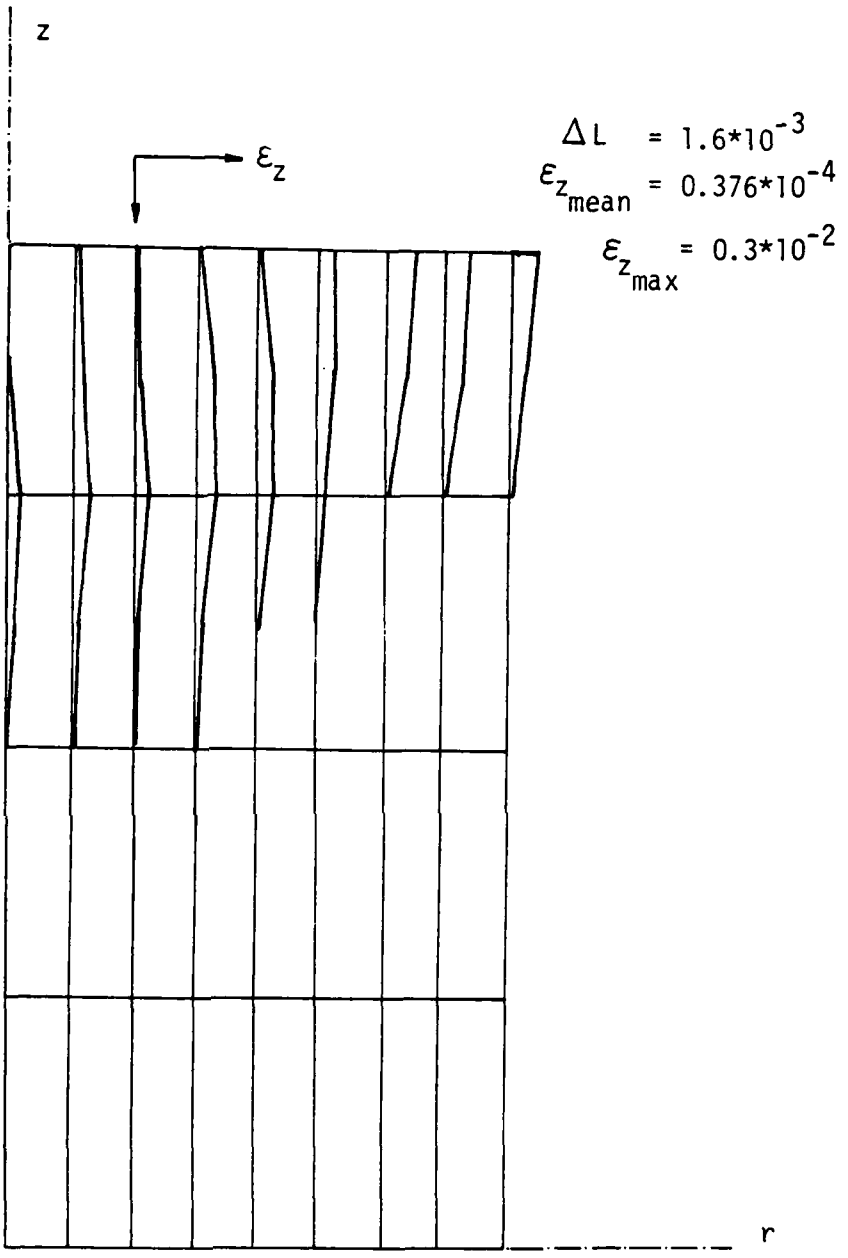

Fig 5-12 Fracture strain localization - distribution of axial strain ε_z over the specimen height

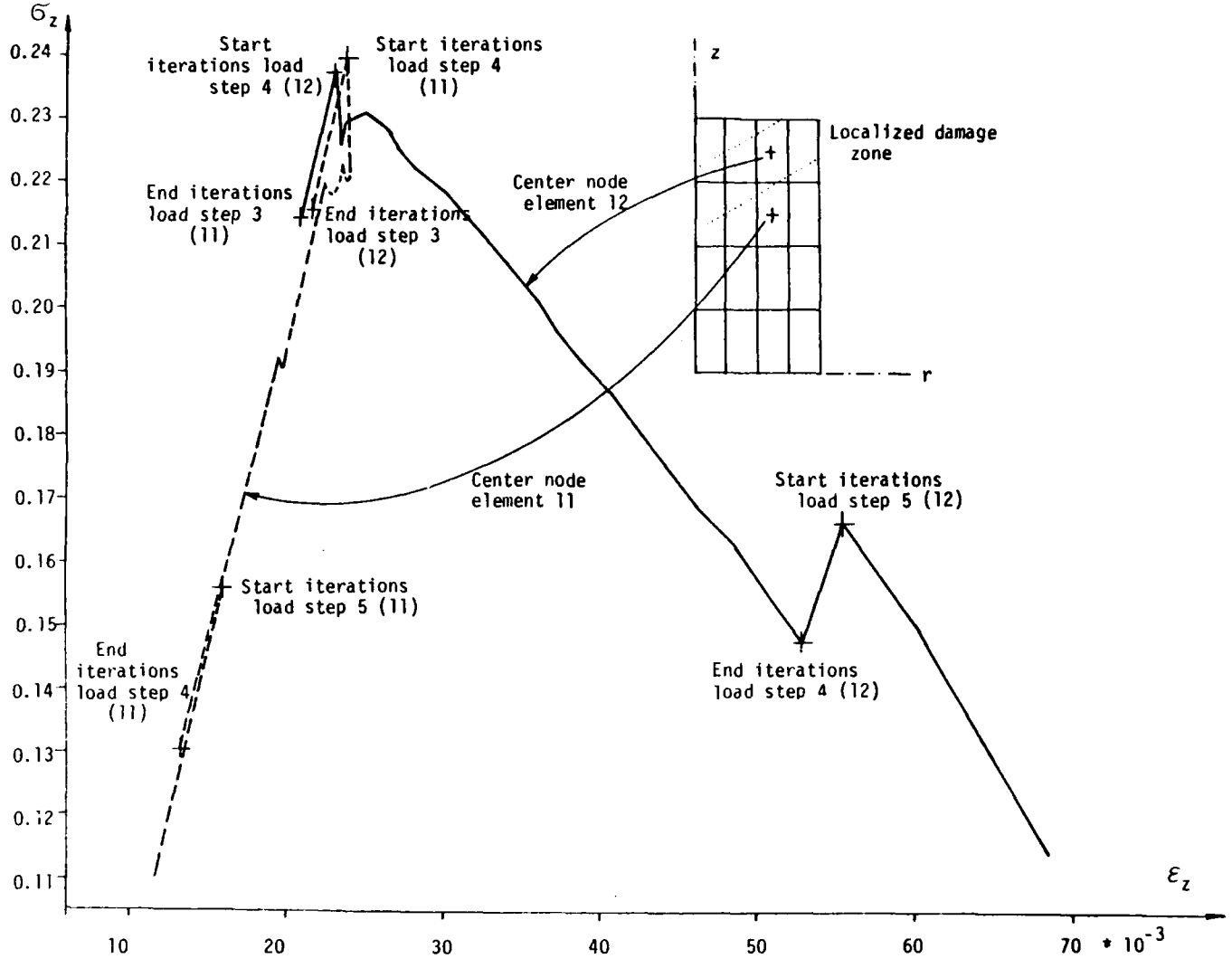

Fig 5-13 Stress/strain histories (σ_z / ε_z) within and outside the localized damage zone - softening vs elastic unloading

the same r-coordinate the distribution of the total axial strain ε_z is displayed. This strain distribution corresponds to the deformation state when the overall specimen elongation is $\Delta\ell = 1.6 \cdot 10^{-3}$", with a nominal strain $\bar{\varepsilon}_z = 0.376 \cdot 10^{-4}$.

The predicted ε_z distribution reveals that the material in localization zone exhibits large tensile straining following the softening material law, whereas the material outside the tensile failure zone exhibits elastic unloading. It is interesting to note that local fracture strains are two orders of magnitude larger than the average strain.

To accentuate further the difference in material behavior within and outside the fracture localization zone, two stress/strain histories are plotted on Fig. 5-13. The material point located within the localized damage zone follows the softening branch, while the material point outside the damage zone exhibits elastic unloading. The discontinuities correspond to elastic loading with the initial stiffness K_0 which is followed by a stress decrease due to progressive cracking enforced by residual load iterations.

5.3.3 Tensile Notched Specimen Predictions

In both compression and tension test predictions the initial state of stress was fairly uniform, and only the slight variation in the stress field due to the lateral restraint at the loading platen led to crack or shear slip initiation. In order to examine localization at a predetermined crack, the response behavior of a hypothetical tensile notched specimen was studied, again using all three meshes, coarse 2*2, medium 4*4, and fine, 6*6 idealizations. The damage volume fraction was

kept constant (irrespective of the mean stress), for the analogous mesh sensitivity study. Medium mesh response was regarded as the control solution. Again the computational predictions using the same damage volume fraction V_d/V_t yielded better agreement with the target response curve than the predictions with same damage volume V_d, Fig. 5-14.

It should be noted that this conclusion is based only on the results from the 4N, 6NV and 6NR predictions. Both results for the 2*2 mesh are distorted by gross discretization errors. This mesh is far too coarse to capture the severe stress concentrations around the notch.

TABLE 5.3 HYPOTHETICAL NOTCHED SPECIMEN PREDICTION ANALYSES

Mesh Size	Localization Function Parameters			Localization Model	Prediction Label
	σm_1	σm_2	dmax		
4*4	$+\infty$	$-\infty$	0.057	Control test Prediction	4N
2*2	$+\infty$	$-\infty$	0.057	Same V_d as control test	2NV*
2*2	$+\infty$	$-\infty$	0.057	Same V_d/V_t as control test	2NR*
6*6	$+\infty$	$-\infty$	0.057	Same V_d as control test	6NV
6*6	$+\infty$	$-\infty$	0.057	Same V_d/V_t as control test	6NR

* discretization error too big - mesh too coarse

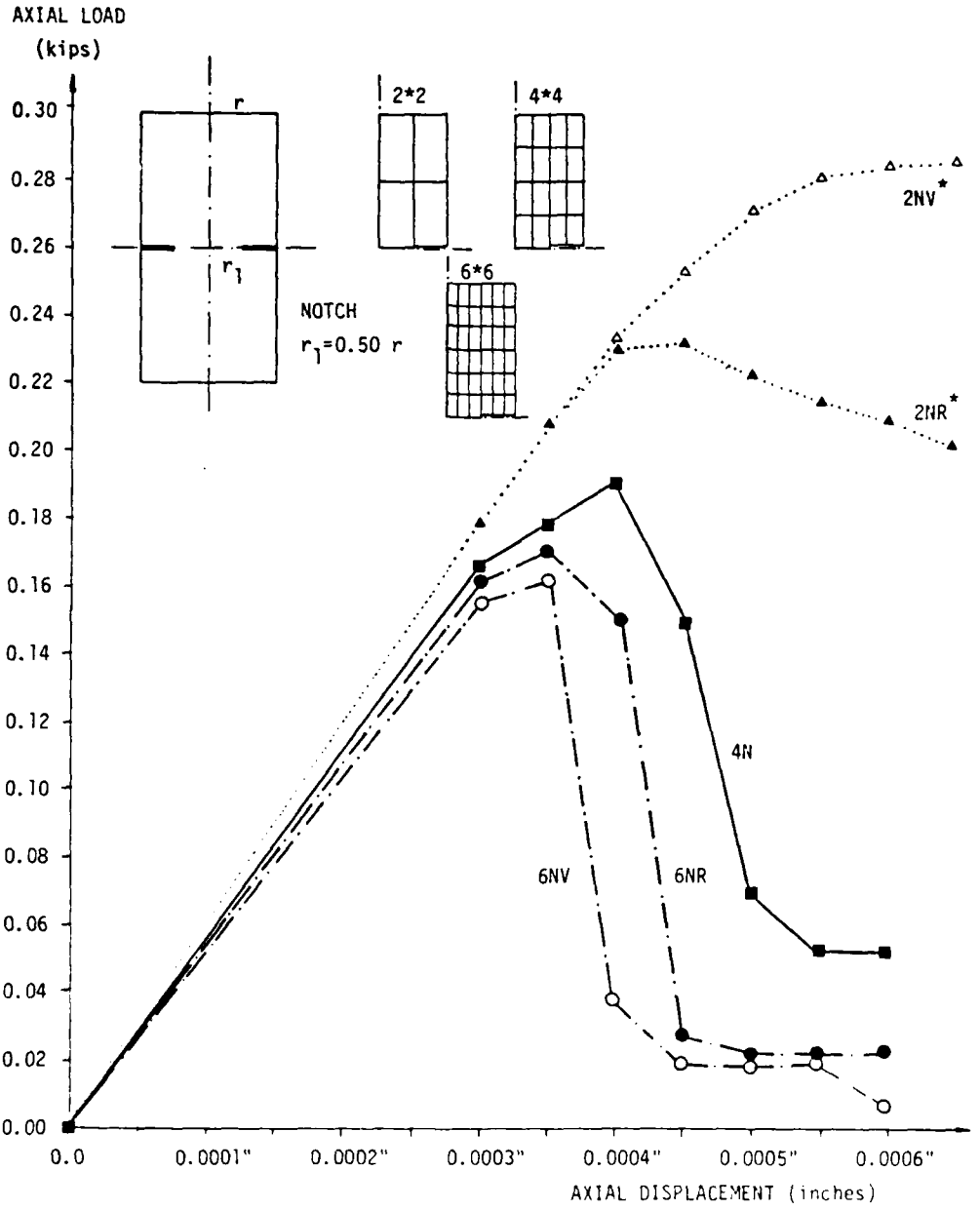

Fig 5-14 Prediction analyses and mesh sensitivity study for the hypothetical notched tension specimen

Inspection in elastic stress field distribution revealed very poor agreement between the local stresses and the overall reactions which is entirely due to discretization error.

However, this notched specimen study indicated again less mesh size sensitivity if softening is formulated assuming that the damage volume fraction remains constant during cracking.

It should be noted that this conclusion is somewhat misleading and can be attributed to the particular functional relationship for the damage zone material law.

Namely, the damage zone law

$$\eta_t = 2\alpha_t - 1$$

does not keep the fracture energy content of an element constant if the mesh size is changed, while keeping d_t constant.

Several additional computational investigations have been conducted using the constant damage zone behavior, i.e.

$$\eta_t = C_1 \quad \eta_s = C_2$$

which correspond to the constant fracture energy content for elements of different sizes.

The conclusions of these investigations indicate that the formulation keeping the damage volume fraction constant leads to less mesh sensitivity for all compression test computations and even for the direct tension test prediction. However, in the case of the notched specimen, the formulation keeping the size of the damage zone constant leads, as expected, to less mesh sensitivity.

6. DIRECT SHEAR TEST STUDY

As it has been indicated earlier, the direct shear box test represents a confined fracture test within a miniature structure rather than a material test. Both tensile and shear slip failures take place - tensile cracking being dominant at low confining pressure, whereas the shear slip failure dominates the response at high confining pressures. The complexity of the direct shear test apparatus requires the partial inclusion of the loading frames and shear box compartments into the finite element model, see Ref. [7]. The details of the adopted element idealization developed by Christensen [38] are discussed in Section 6.1. The influence of different concrete ductility (brittle, perfectly plastic and linearly softening behavior) and mesh size effects are addressed in Section 6.2, where hypothetical low strength concrete material parameters are employed. Finally, Section 6.3 discusses the numerical predictions of the direct shear test, using the composite damage model for both tensile and shear softening, developed in Chapters 4 and 5.

6.1 Finite Element Idealization

The direct shear test apparatus was described earlier. Figure 6-1 gives more detailed information about the particular components of the test apparatus that are discretized using the finite elements for the numerical study. The specimen supporting apparatus is designed to test samples with dimensions up to 8" x 8" x 4 5/8", however, samples measuring 8" x 4" x 4 5/8" were actually tested. The upper and lower

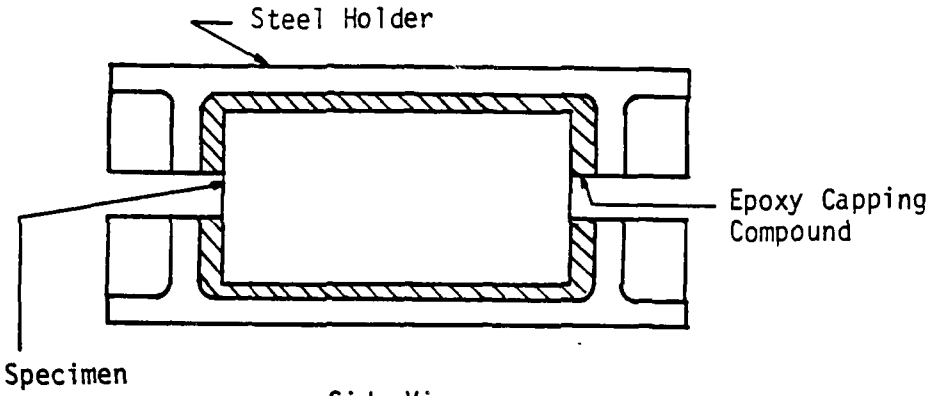

Side View

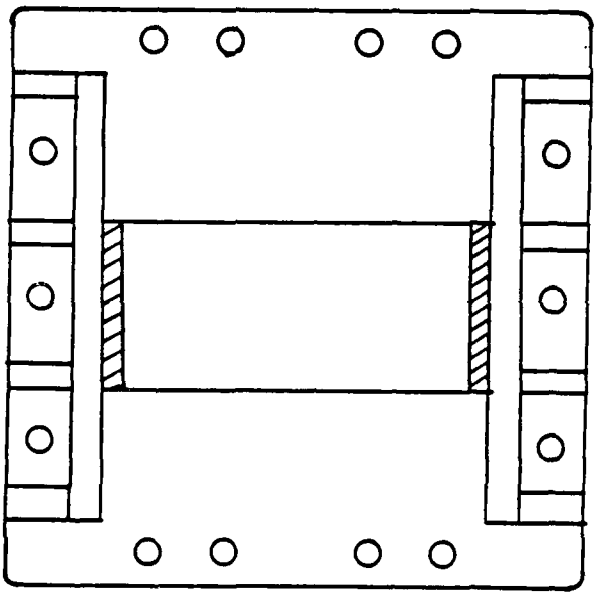

Top View

Fig 6-1 Specimen Holder

shear box compartments are made from 14" x 14" x 3/8" steel plate with 2" x 3/4" stiffening end walls welded into place.

It is assumed that the specimen and the test apparatus can be modeled in a plane strain state. Under this assumption, the nine node quadrilateral and six node trangular plane strain elements of the three dimensional finite element program SMART [39] are used in the analysis.

The behavior of the test specimen cannot be predicted by discretizing only the test sample, since the load transfer from the apparatus to the test specimen is not accurately represented if only the specimen is idealized. This load transfer is captured by including the upper and lower shear box compartments in the discretization. A typical example of the shear box mesh is shown in Figure 6-2. Upper and lower loading frames are included in the finite element model so that the horizontal load and the horizontal reactions are collinear with the prevailing shearing plane of the test specimen. These loading frames are accentuated by the bold lines in Figure 6-3. The upper portion of the loading frames represents a lumping of the top reaction frame and the top support frame. The lower portion of the loading frame in Figure 6-3 represents a lumping of the shear load transmitting block and the bottom support plate. The loading frames represent considerable stiffness and are assigned the appropriate properties in the finite element model; i.e., steel material properties and a thickness of 14 inches. Figure 6-4 shows the complete idealization of the test specimen supporting apparatus. The shaded elements represent the epoxy capping compound that is used to bond the test specimen into the shear box.

The uniform geometry of the test specimen is discretized with quadrilaterial elements as shown in Figure 6-5. Figure 6-6 illustrates

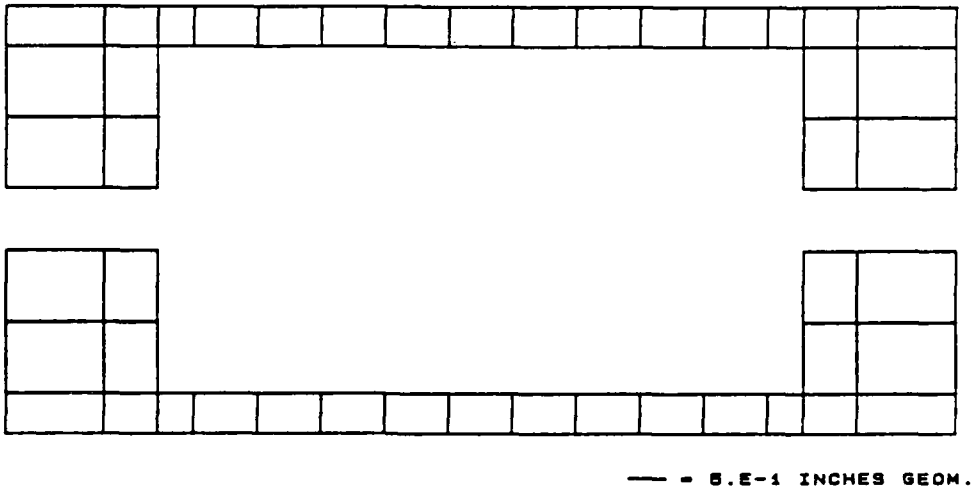

Fig 6-2 Specimen Shear Box Idealization

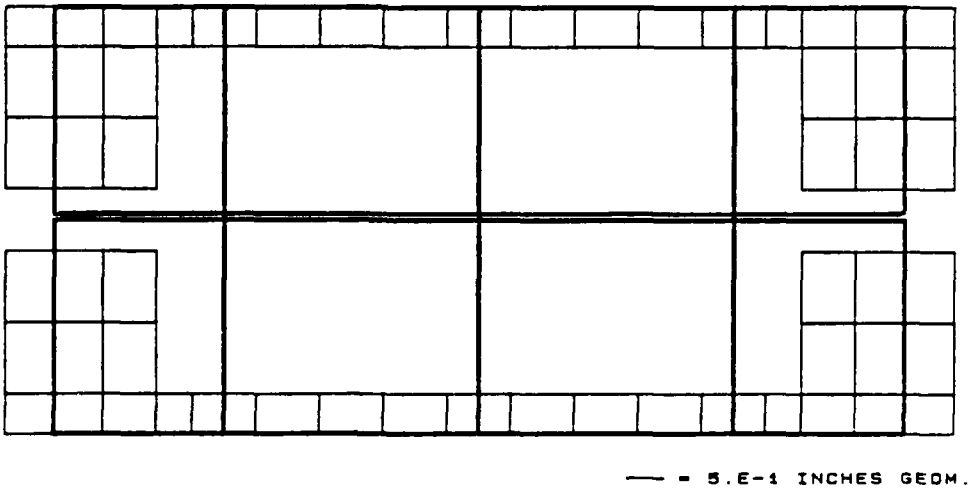

Fig 6-3 Loading Frame Idealization

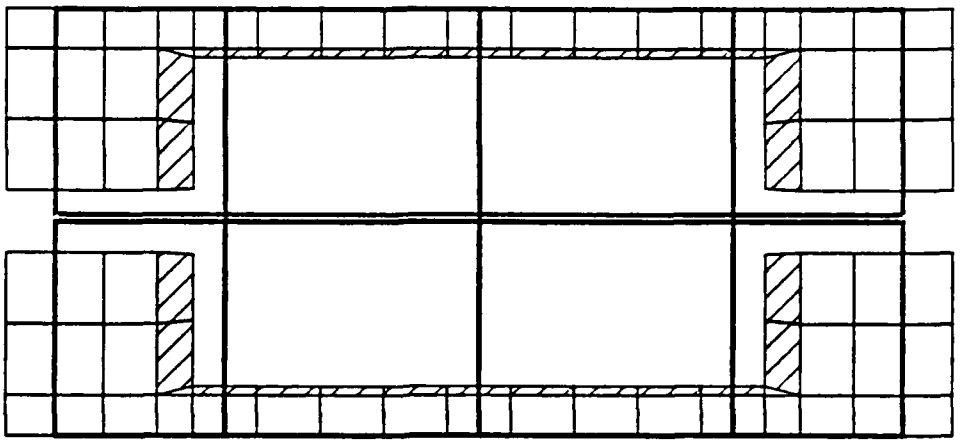

Fig 6-4 Test Specimen Supporting Apparatus Idealization

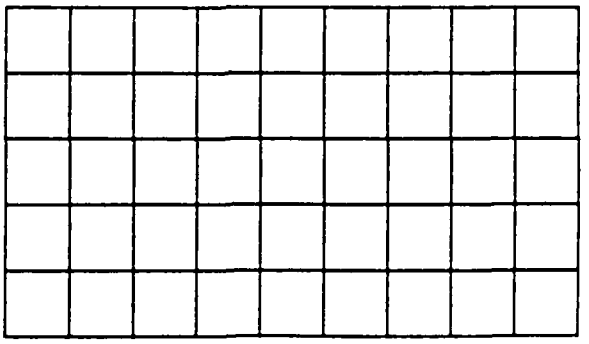

Fig 6-5 Test Specimen Idealization

how the finite element mesh for a sample fits into the remainder of the finite element model.

The boundary and loading conditions are illustrated in Figure 6-7. That part of the test apparatus which is not discretized is assumed to be rigid and is modeled by appropriate boundary conditions. The confining pressure due to the normal load actuator, is applied in the form of consistent nodal loads along the top edge of the upper shear box compartment. A prescribed displacement is imposed on the lower loading frame to represent the lateral motion due to the horizontal actuator.

6.2 Parametric Studies

Parametric studies involve two different numerical investigations. The first one is related to the post-failure softening strategy and how it influences the overall response of the model. The second investigates the mesh sensitivity of the finite element model in terms of a convergence study involving three different meshes. These two parameter studies are performed in order to gain a better understanding of the techniques involved, see also Ref. [38].

The material properties adopted for these parameter studies are representative of a typical low strength concrete and are not related to the concrete material used for the actual specimens.

The properties of all materials used in the finite element model (concrete, steel, epoxy) are listed in Tables 6-1 and 6-2. The uniaxial compressive strength of concrete is assumed to be f'_c = 2.0 ksi. Using this value and the ACI recommendations, the modulus of elasticity is

$$E_c = 33\ w^{1.5}\ \sqrt{f'_c}$$

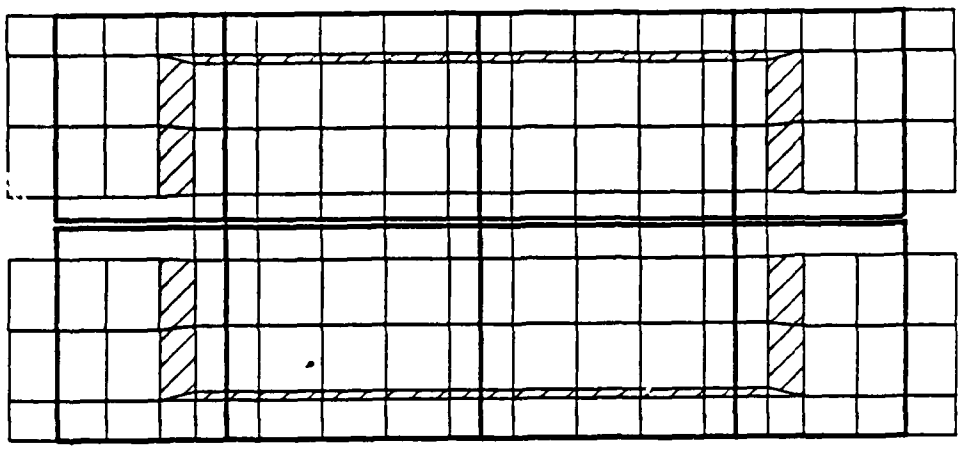

- 125 DOF - 1105 - 4

Fig 6-6 Finite Element Idealization of the Test Apparatus and Test Specimen

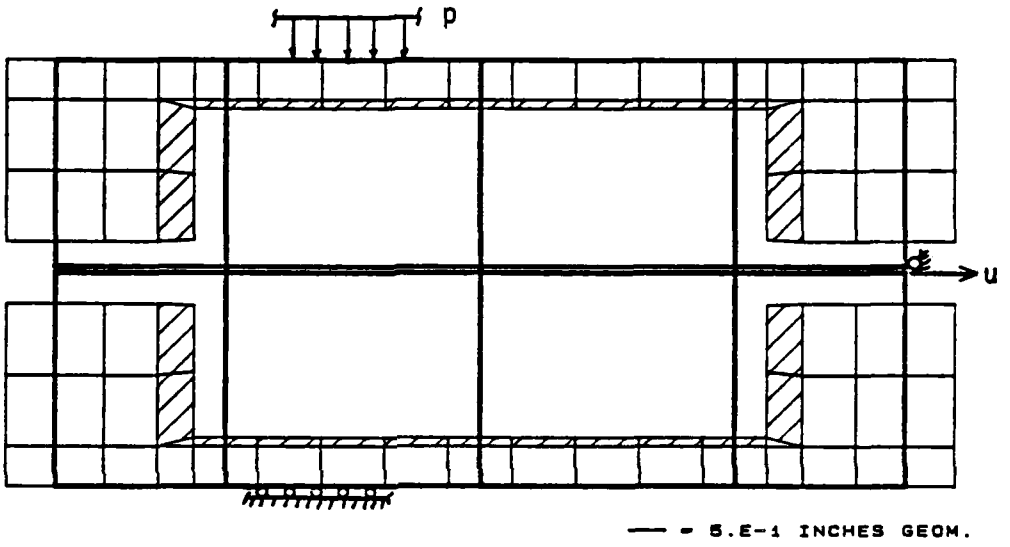

Fig 6-7 Model Boundary and Loading Conditions

A Poisson's ratio of $\nu = 0.2$ is adopted for the parametric study below. The epoxy properties were determined from laboratory tests.

TABLE 6.1 Material Properties

MATERIAL	YOUNG'S MODULUS (ksi)	POISSON'S RATIO
Steel	29,000	.32
Epoxy	400	.35
Concrete	2,500	.20

TABLE 6.2 Finite Element Model Properties

COMPONENT	MATERIAL	THICKNESS
		(inches)
Specimen Shear box Compartment	Steel	14
Upper and Lower loading Frame	Steel	14
Specimen	Concrete	4
Capping Compound	Epoxy	4

6.2.1 Influence of Post-Peak Model

One of the principal interests is the influence of the post-peak softening strategy reflecting material ductility on the predicted response of a structure that has experienced shear failure. In the direct shear test specimen under lateral loading and low normal pressure tensile cracking dominates the failure mechanism; therefore, a high normal pressure of 6.90 MPa (1000 psi) was used in the parameter study in order to mobilize the frictional slip mode of failure. The high normal pressure increases the compressive stresses in the specimen, thereby increasing the amount of shear slip and reducing the amount of tensile cracking.

The initial fracture criterion was constructed using a friction angle of 41.0 degrees, a cohesion value of 0.45 ksi, and a tension cutoff of 0.18 ksi. The initial fracture surface is shown in Figure 6-8. Three different post-failure softening strategies were investigated: brittle, perfectly plastic, and linear softening behavior.

The brittle post-peak model is illustrated in Figures 6-9 and 6-10 and gives a lower bound solution to the ultimate strength. This abrupt softening concept was imposed on the fractured elements by establishing a post-peak surface which had no cohesive or tensile strength. After brittle failure takes place only residual shear strength can be mobilized, which is controlled by the residual friction angle.

The perfectly plastic post-failure behavior is illustrated in Figures 6-11 and 6-12 and gives an upper bound solution to the ultimate strength. This perfectly plastic concept was imposed on the fractured

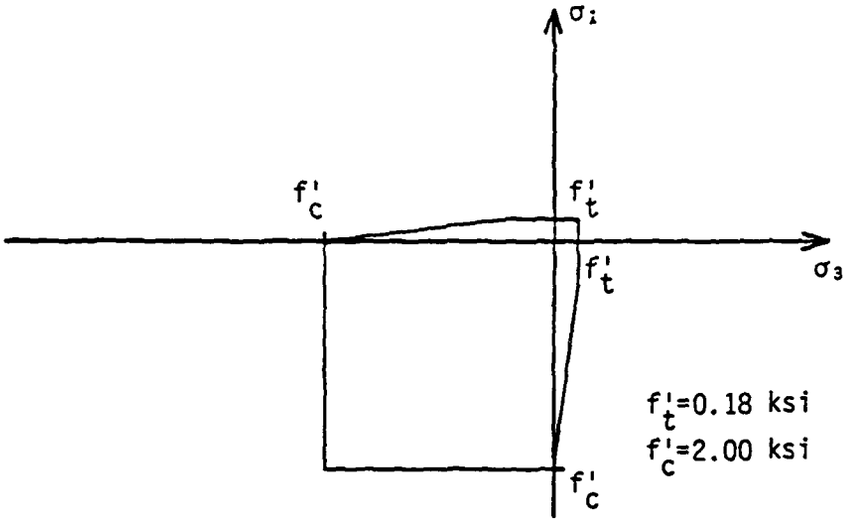

Biaxial Stress Space

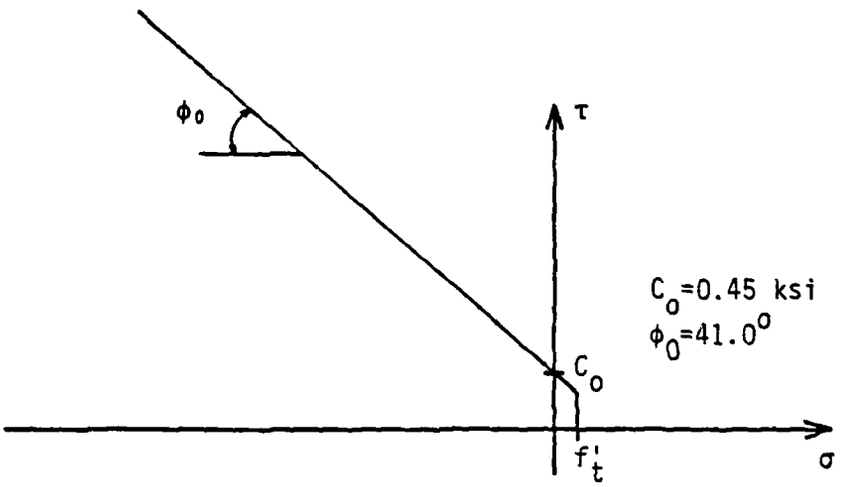

Mohr's Diagram

Fig 6-8 Initial Fracture Surface

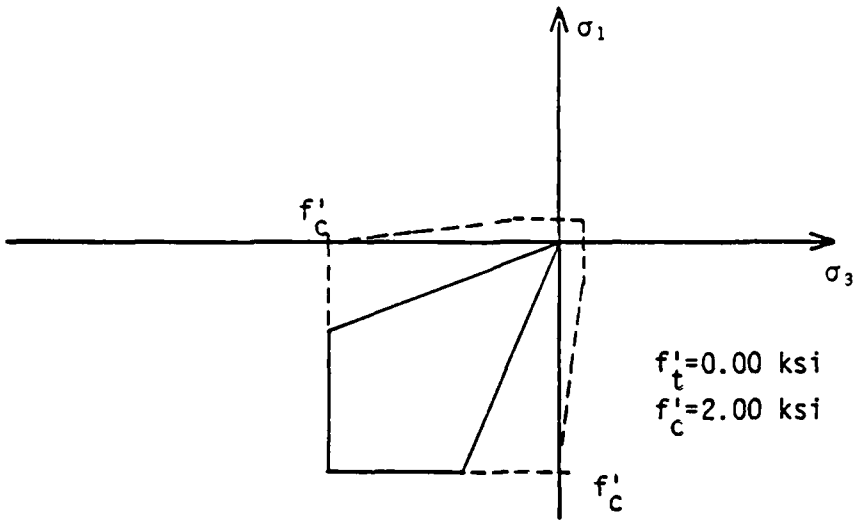

Biaxial Stress Space

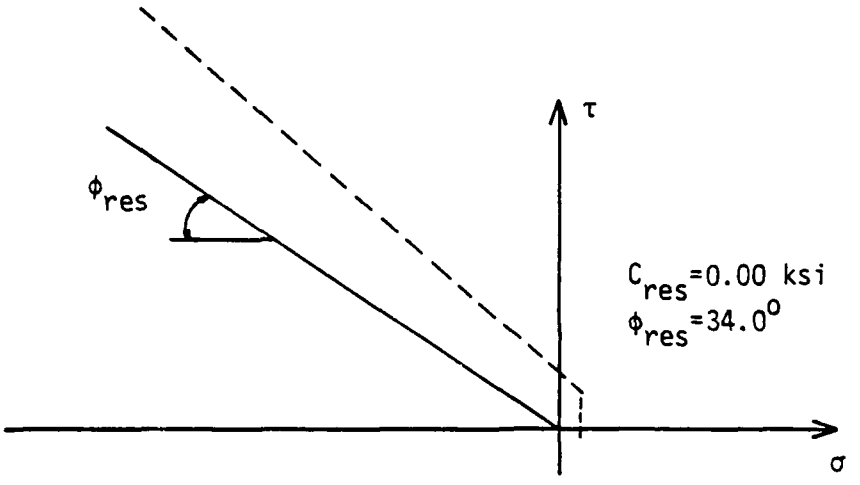

Mohr's Diagram

Fig 6-9 Residual Strength Criteria for Brittle Softening Assumption

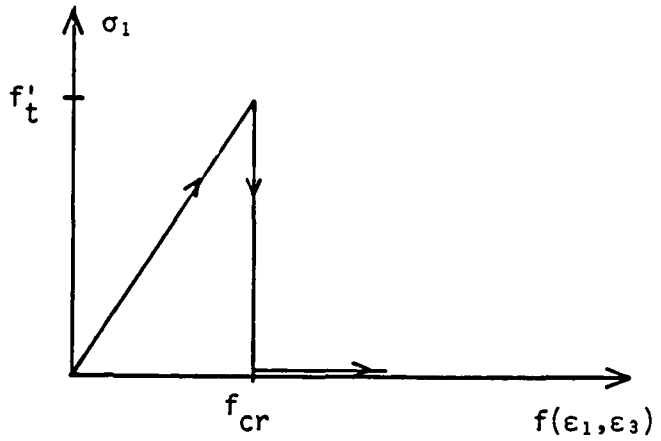

Tensile Stress-Strain Relation

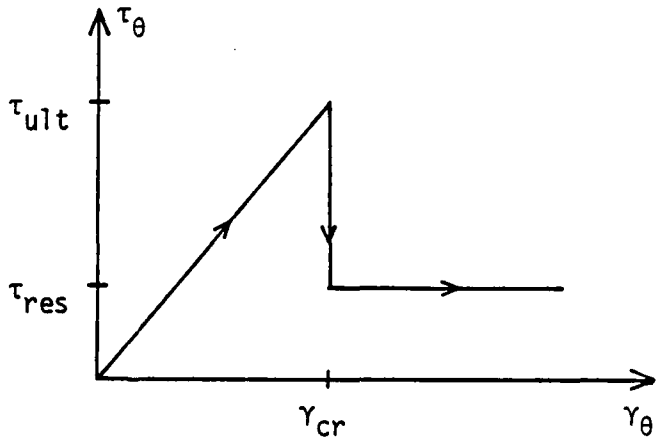

Shear Stress-Strain Relation

Fig 6-10 Stress-Strain Behavior for Brittle Softening Assumption

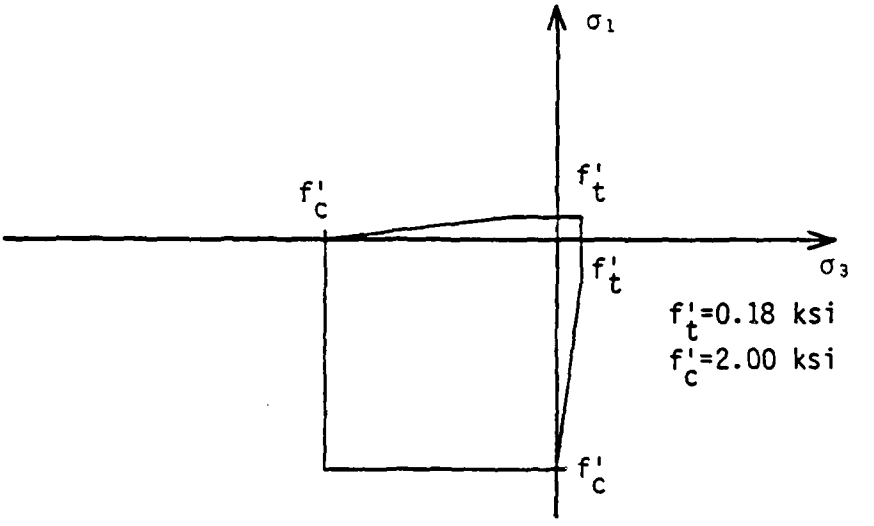

Biaxial Stress Space

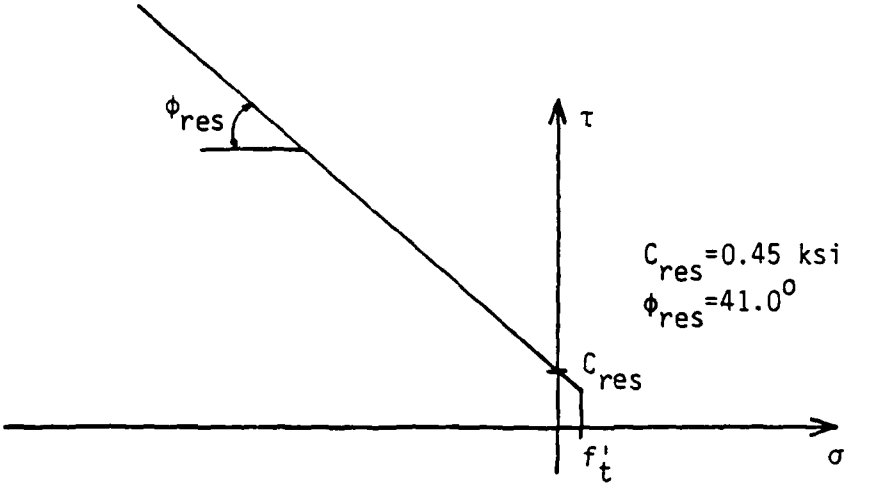

Mohr's Diagram

Fig 6-11 Residual Strength Criteria for Perfectly Plastic Assumption

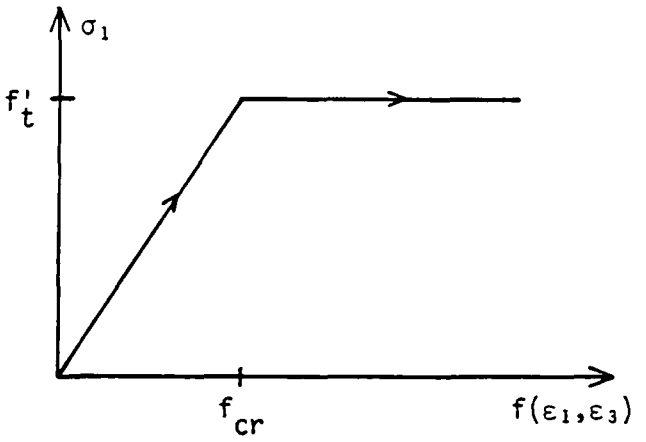

Tensile Stress-Strain Relation

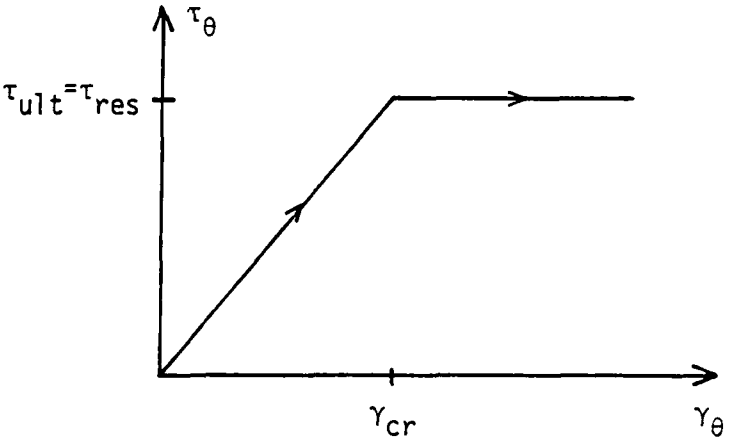

Shear Stress-Strain Relation

Fig 6-12 Stress-Strain Behavior for Perfectly Plastic Assumption

elements by leaving the initial surface unchanged after fracture.

The linearly degrading post-peak softening is illustrated in Figures 6-13 and 6-14. This softening was imposed on the fractured elements by degrading the post-failure strength criteria with increasing strains, along the line of composite damage model described in Chapter 4.

In the parameter study the damage volume fractions α_t and α_s were kept constant, and were adjusted to give $E_s = -E$ and $G_s = -G$ softening behavior. A shear stress transfer strategy, which keeps the mean stress on a shear slip plane constant, was adopted.

The load versus displacement response of the finite element model for the three softening strategies is shown in Figure 6-15. The analysis was carried out in the following sequence:

a. The 1.00 ksi normal load was applied first.

b. An increment of displacement was prescribed to the lower loading frame to raise the specimen's stress state to the elastic limit when cracking initiates.

c. The lower loading frame was given an additional small increment of displacement to initiate the fracture process.

d. Results were recorded, and additional increments of displacement were prescribed until the residual strength level was reached.

The distribution of principal stresses for the limiting cases of brittle behavior and perfectly plastic behavior is shown in Figures 6-16 through 6-18. The state of stress at the elastic limit is shown in Figure 6-16, and is the same for both cases. The stresses at the peak response are shown in Figure 6-17. This figure illustrates the dramatic

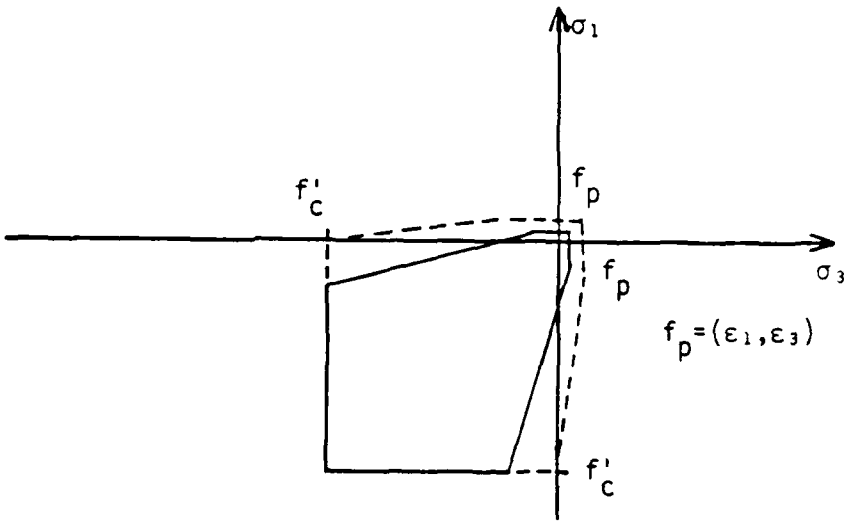

Biaxial Stress Space

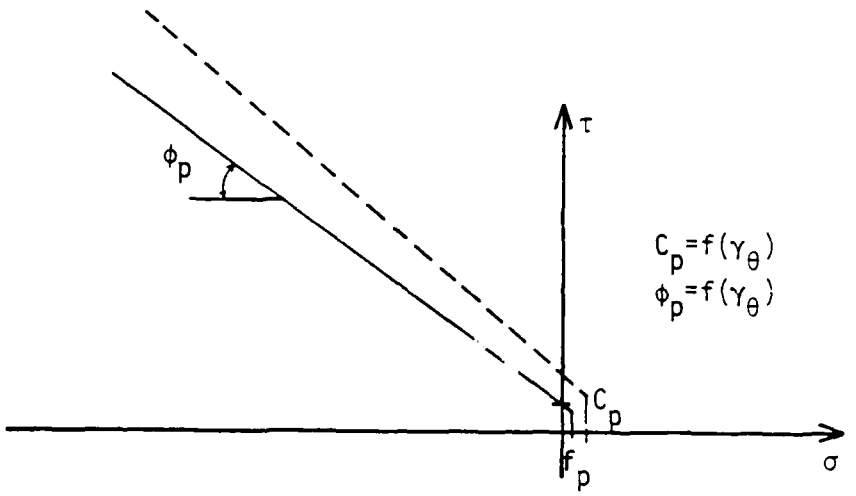

Mohr's Diagram

Fig 6-13 Post Fracture Criteria for Linear Softening Assumption

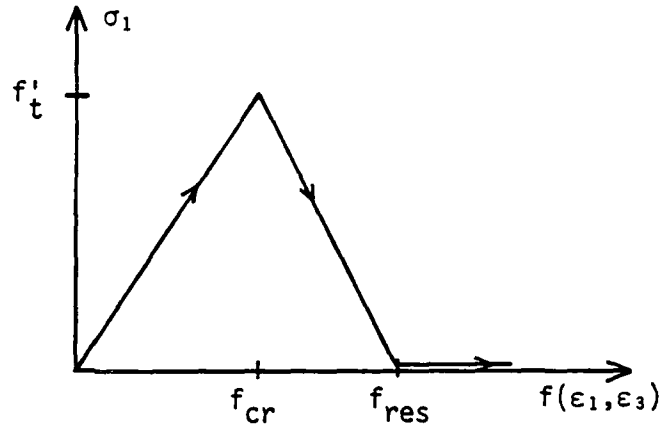

Tensile Stress-Strain Relation

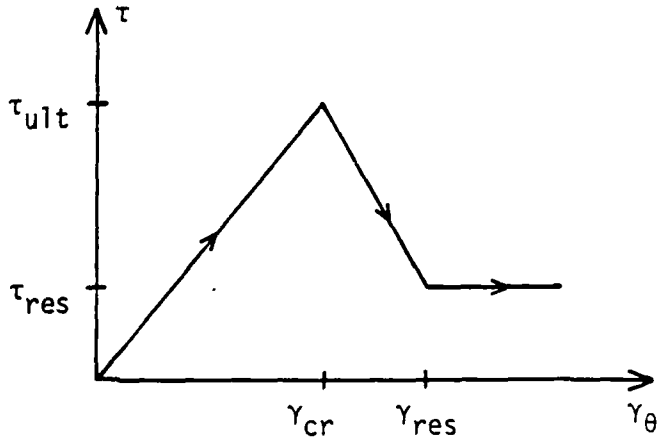

Shear Stress-Strain Relation

Fig 6-14 Stress-Strain Behavior for Linear Softening Assumption

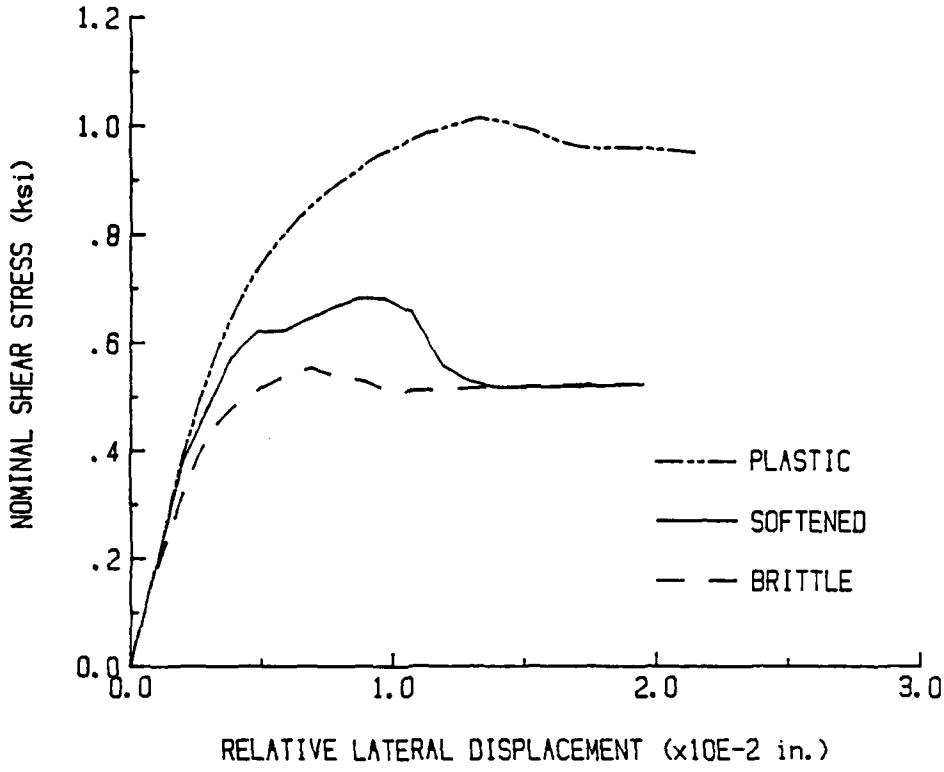

Fig 6-15 Softening Study Response Curves

effect that the softening strategy has on the magnitude of the principal stress and therefore on the level of the peak response of the model. Figure 6-18 shows the pricipal stresses that exist at the residual load level. The principal stresses along the horizontal center line are reduced compared to the stresses that form the diagonal compression struts. These low stresses correspond to the formation of a continuous horizontal slip plane along the center line of the specimen. The formation of the continuous slip plane is caused by the high shear strain caused by the confinement exerted on the specimen by the upper and lower shear box compartments. The deformed meshes shown in Figure 6-19 illustrate this confinement.

It can also be seen in the stress distribution for the brittle softening assumption of Figure 6-18 that integration of the vertical stress component along the horizontal centerline of the specimen does not satisfy static equilibrium of the vertical forces. We should, however, keep in mind that the brittle post-peak model imposes dramatically reduced shear strength values in the areas of the potential slip planes. The analysis attempts to enforce this low shear strength locally in the form of iterative stress transfer. However, since the average stress remains unchanged in the adopted shear stress redistribution strategy and because the vertical stress component, σ_y, should remain equal to 0.10 ksi for local equilibrium the stress transfer is severely constrained. The finite amount of iterative effort coupled with the global convergence criteria enforces only global equilibrium to be satisfied at the nodes thereby allowing local equilibrium of stresses to be violated.

One significant conclusion that can be drawn from the softening study is that a wide spectrum of responses can be obtained depending on

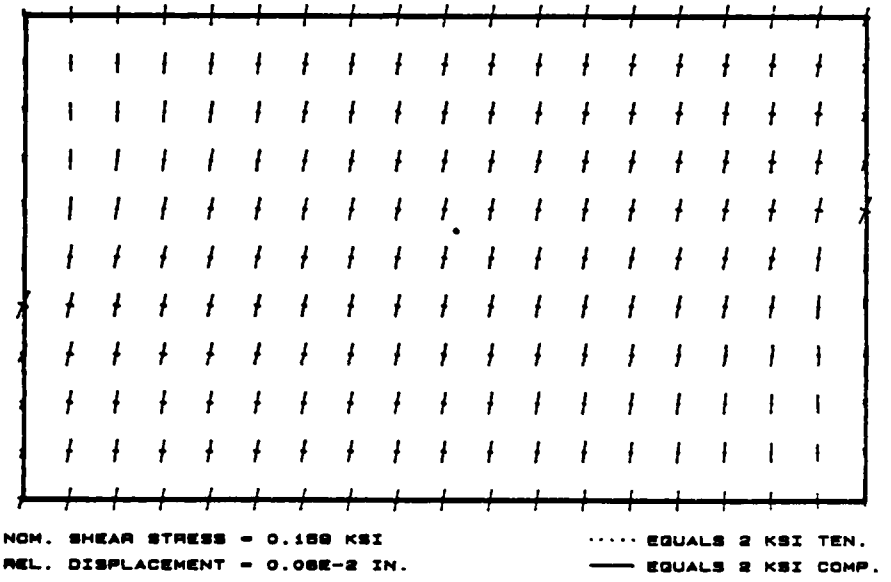

Fig 6-16 Principal Stress Distribution at the Elastic Limit (p=1.00 ksi)

BRITTLE SOFTENING ASSUMPTION

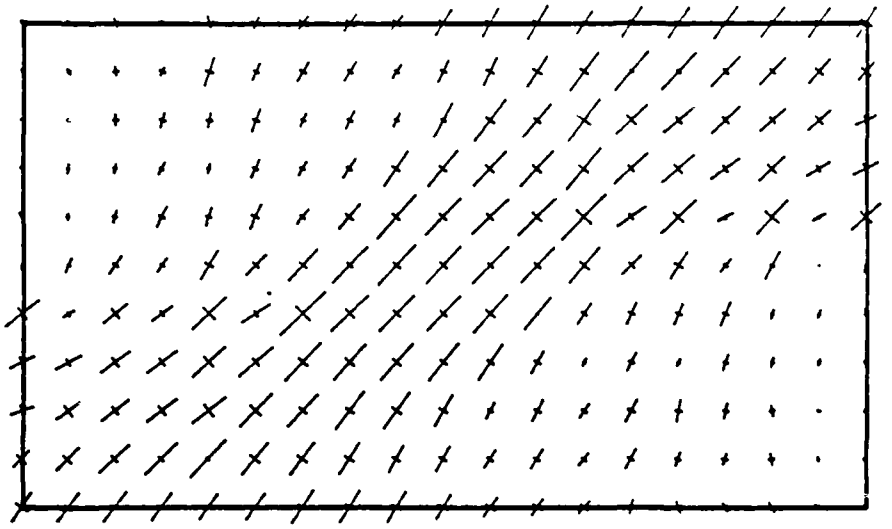

NOM. SHEAR STRESS = 0.555 KSI
REL. DISPLACEMENT = 0.88E-2 IN.

····· EQUALS 2 KSI TEN.
—— EQUALS 2 KSI COMP.

PERFECTLY PLASTIC ASSUMPTION

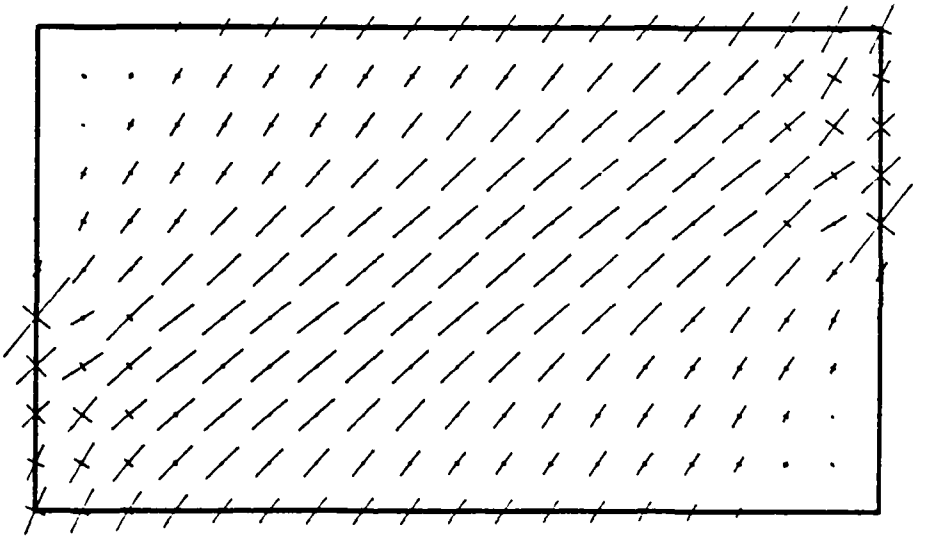

NOM. SHEAR STRESS = 1.003 KSI
REL. DISPLACEMENT = 1.23E-2 IN.

····· EQUALS 2 KSI TEN.
—— EQUALS 2 KSI COMP.

Fig 6-17 Principal Stress Distribution at the Peak Response (p=1.00 ksi)

BRITTLE SOFTENING ASSUMPTION

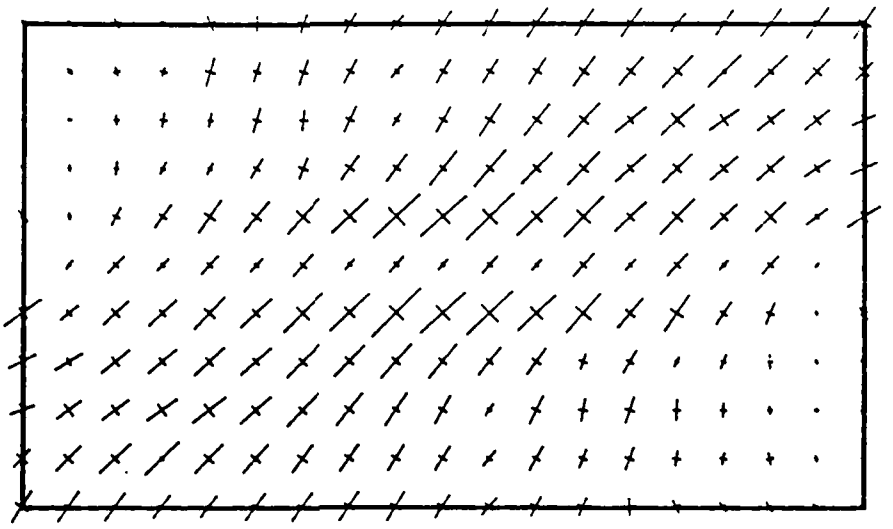

NOM. SHEAR STRESS = 0.621 KSI
REL. DISPLACEMENT = 1.88E-2 IN.

····· EQUALS 2 KSI TEN.
—— EQUALS 2 KSI COMP.

PERFECTLY PLASTIC ASSUMPTION

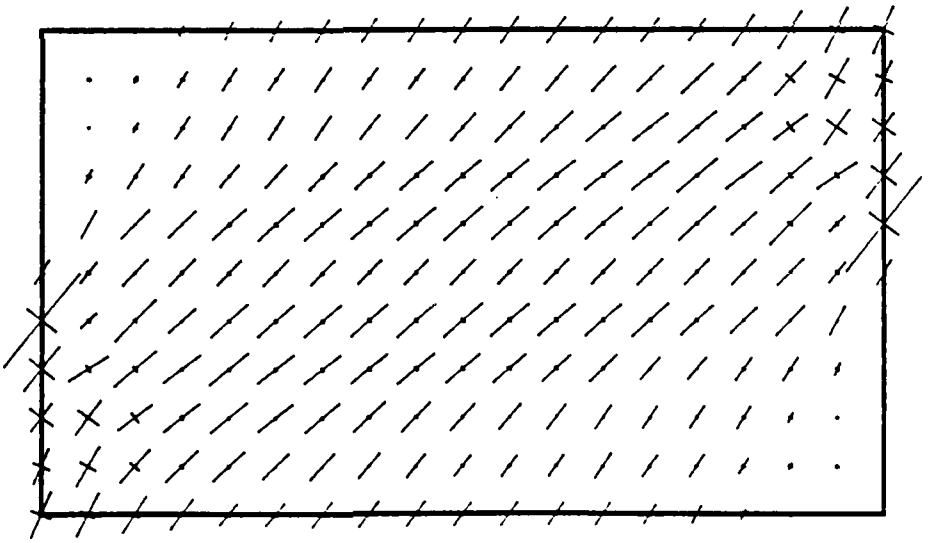

NOM. SHEAR STRESS = 0.950 KSI
REL. DISPLACEMENT = 2.14E-2 IN.

····· EQUALS 2 KSI TEN.
—— EQUALS 2 KSI COMP.

Fig 6-18 Principal Stress Distribution in the Residual Response Regime (p=1.00 ksi)

PEAK RESPONSE -- BRITTLE

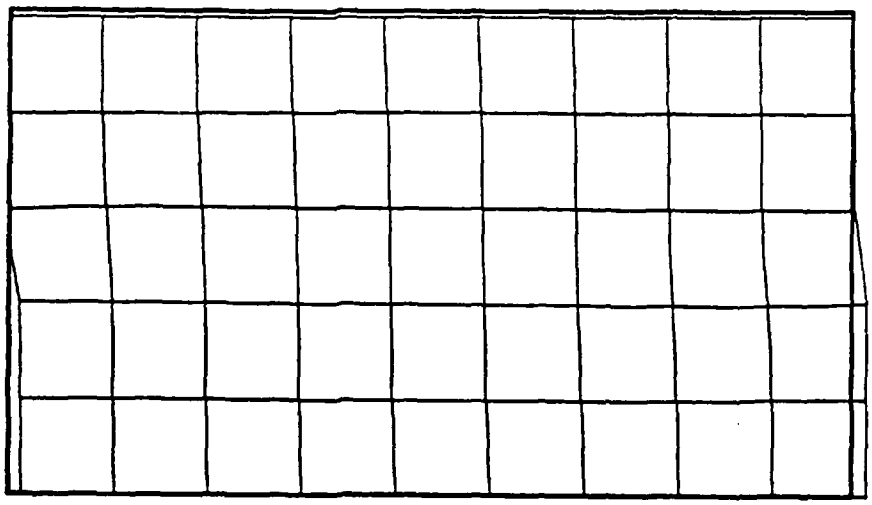

NOM. SHEAR STRESS = 0.685 KSI
REL. DISPLACEMENT = 0.88E-2 IN.

— = 2.E-1 INCHES GEOM.
—— = 2.E-2 INCHES DISP.

RESIDUAL RESPONSE -- BRITTLE

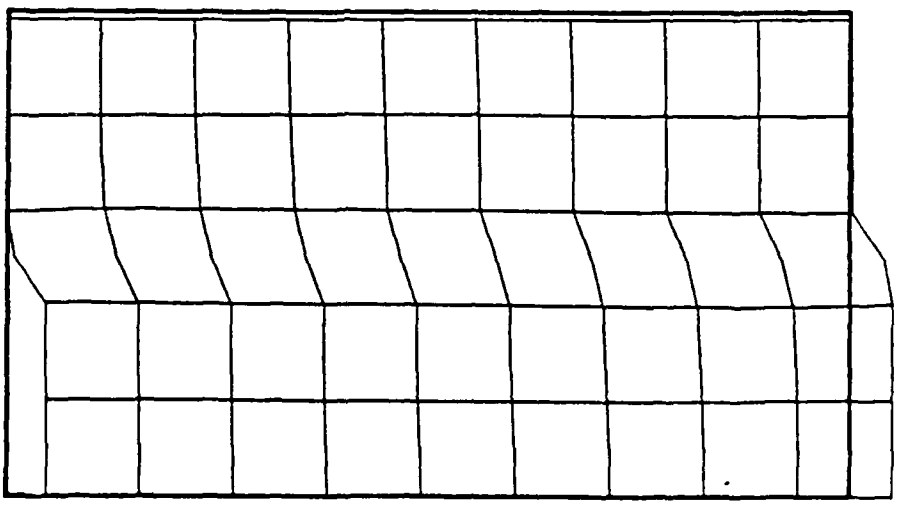

NOM. SHEAR STRESS = 0.521 KSI
REL. DISPLACEMENT = 1.98E-2 IN.

— = 2.E-1 INCHES GEOM.
—— = 2.E-2 INCHES DISP.

Fig 6-19 Deformed Meshes

the type of softening formulation that is selected. This indicates again a definite need for a rational approach to the determination of the post-peak behavior of the fractured material model.

6.2.2 Mesh Size Effects

It has been noted by many investigators, such as Bazant and Cedolin [28], and Pietruszczak and Mroz [8], that the predicted nonlinear behavior of brittle materials is very sensitive with regard to the mesh size. For this reason, a convergence study was carried out to gain additional insight into the mesh sensitivity of the finite element damage predictions.

The loading and support conditions, as well as the material properties used in the parametric mesh size study are the same as those given in Section 6.2.1. A linearly degrading post-peak strength criterion is used throughout this mesh sensitivity study.

The convergence study is carried out by examining three different mesh configurations. The number of elements used to idealize the specimen ranges from 18 elements to 84 elements. The intermediate mesh contains 45 elements. The three specimen idealizations are shown in Figure 6-20.

The rate of convergence for this analysis can not be determined from the three meshes chosen for the convergence study; however, some qualitative observations about the mesh sensitivity of the analysis can certainly be made.

Figure 6-21 shows the load-displacement response of the three meshes. The figure indicates that there is very little mesh sensitivity in the pre-peak range of response, but that in the post-peak range the

3 X 6 ELEMENT MESH

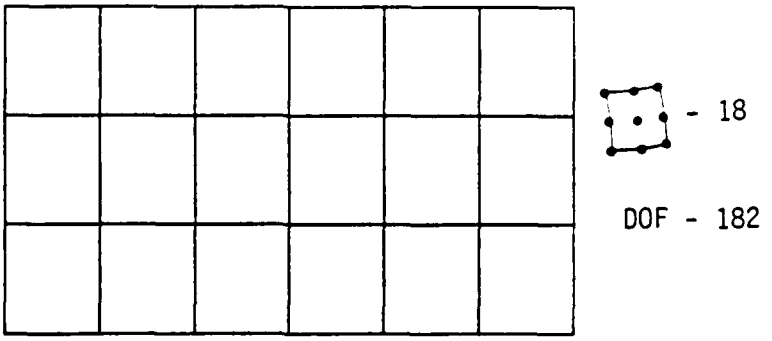

5 X 9 ELEMENT MESH

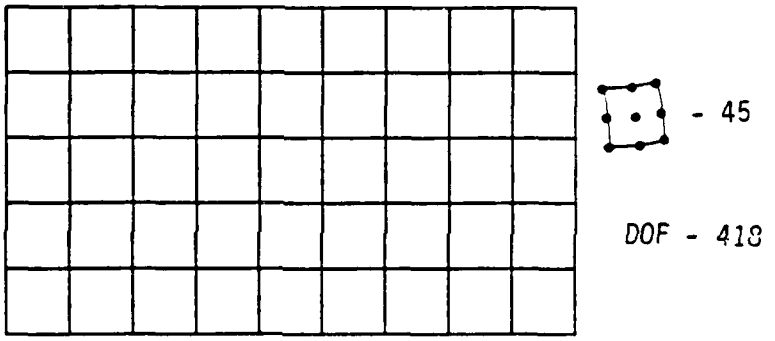

7 X 12 ELEMENT MESH

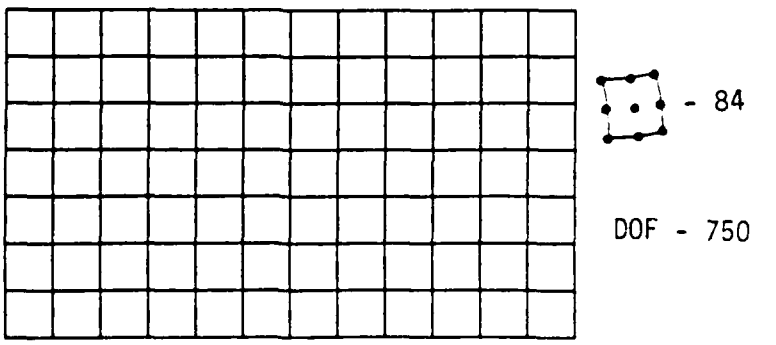

Fig 6-20 Specimen Meshes Examined in the Convergence Study

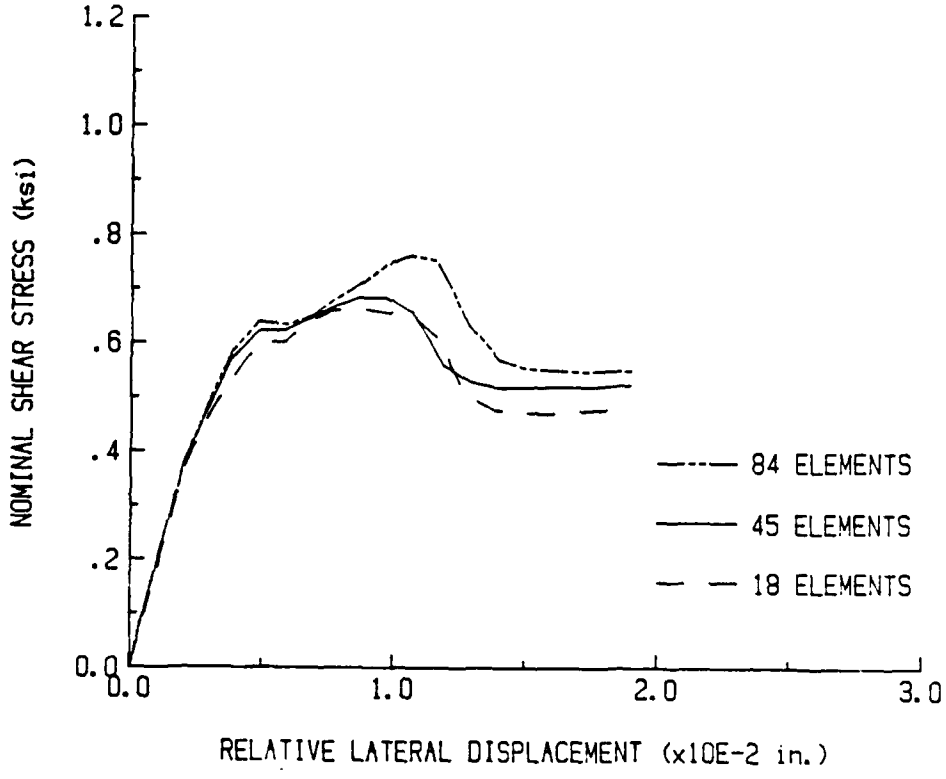

Fig 6-21 Convergence Study Response Curves

response tends to vary more with the mesh size. The mesh sensitivity is not extreme - the peak response varies by only 15% between the coarse and the fine mesh. This lack of mesh sensitivity may be a result of the fact that the reponse for a shear slip mode of failure, which is predominant under the 1.00 ksi normal load, is less sensitive to size effects than the tensile mode of fracture.

6.3 Experimental and Computational Results

The convergence study, presented in Section 6.2, showed that the calculated response of the model is not particularly sensitive with regard to the selection of the finite element mesh. Therefore, the finite element model employing 45 elements for specimen idealization and the linear softening formulation was used to predict the direct shear test results. This medium mesh is quite efficient from a computational standpoint, since the adopted number of degrees of freedom do require considerable computer resources.

The parameters used in the finite element model are those given in Tables 6.1 and 6.2. The damage localization functions for d_s and d_t are adopted from the calibration procedures illustrated in Chapter 5. The finite element idealization was described in Section 6.1.

Only the case of normal pressure p_n = 0.20 ksi is considered here. The normal pressure test p_n = 1.0 ksi was not analyzed because of its pronounced out of plane behavior, which tends to invalidate the underlying plane strain assumption of the computational model.

Figures 6-22a,b illustrate the deformed shapes of the specimen finite element idealization for different stages, while figures

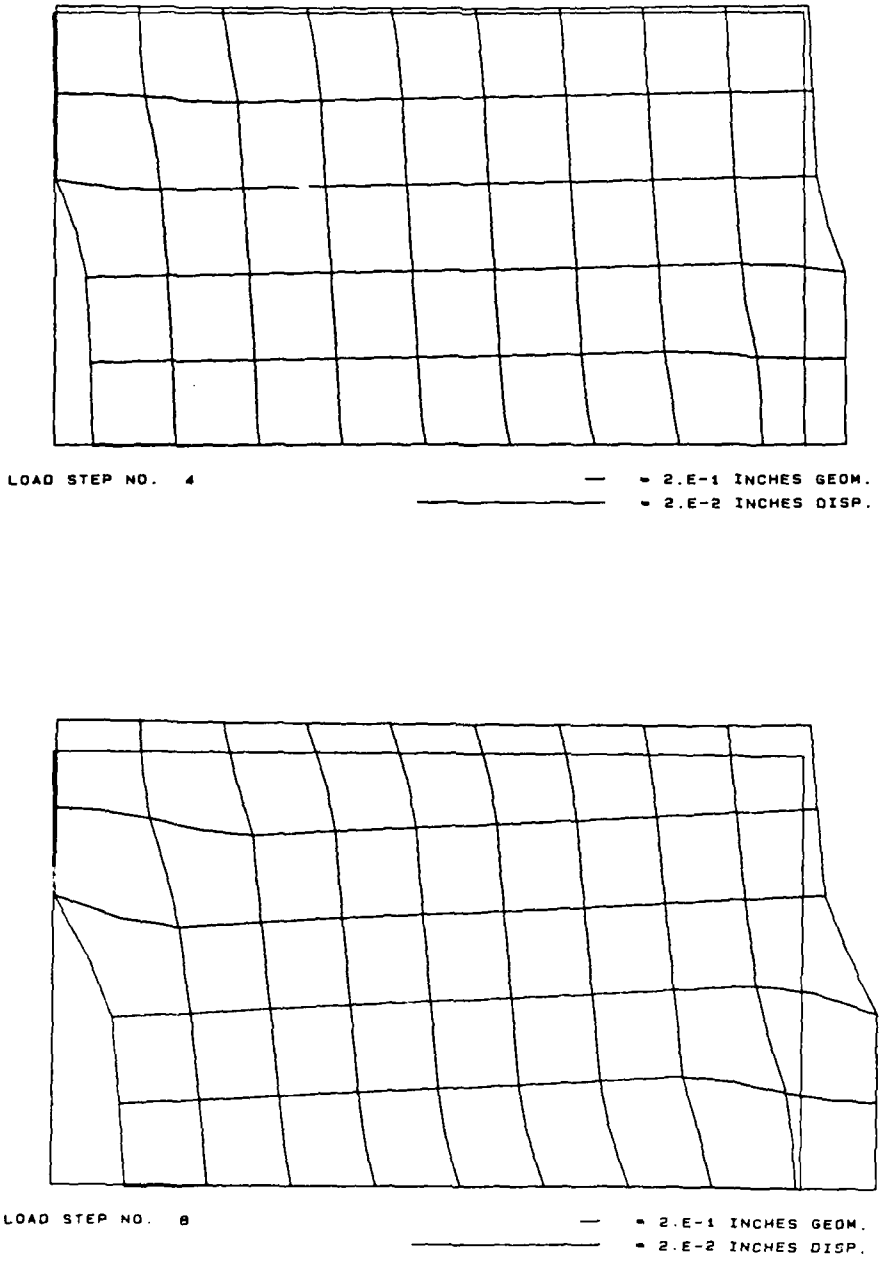

Fig 6-22 Direct shear test - deformed geometry for load steps 4 and 8

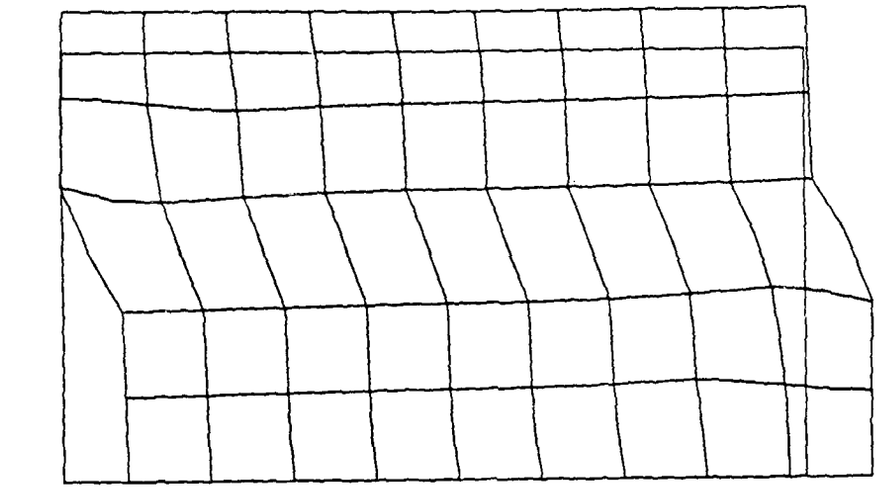

LOAD STEP NO. 16

— = 2.E-1 INCHES GEOM.
—— = 2 E-2 INCHES DISP.

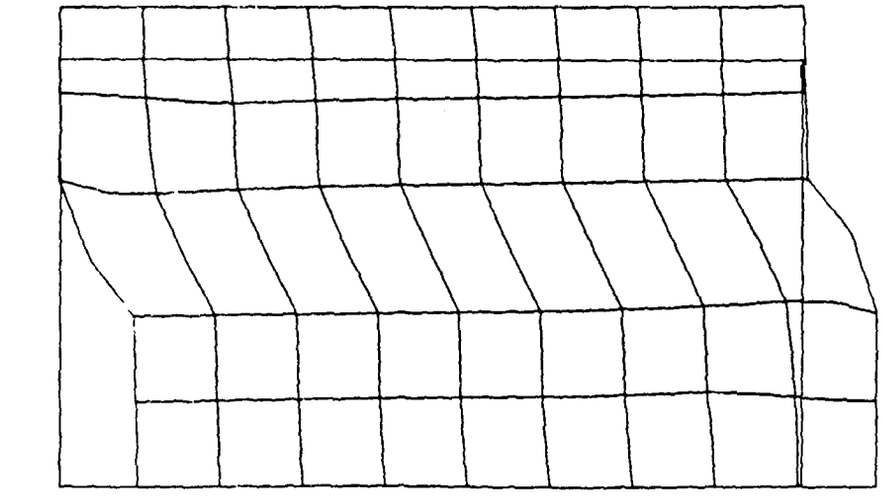

LOAD STEP NO. 20

— = 2.E-1 INCHES GEOM.
—— = 2.E-2 INCHES DISP

Fig 6-22.a Direct shear test - deformed geometry for load steps 16 and 20

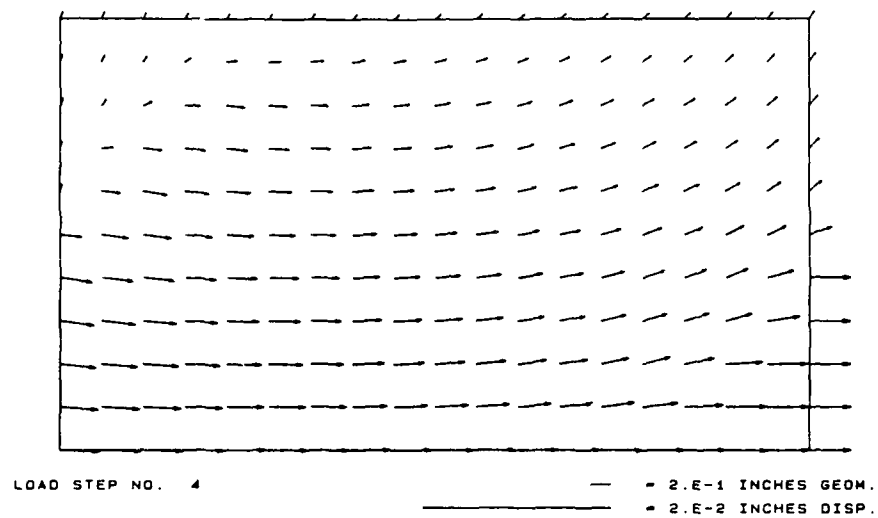

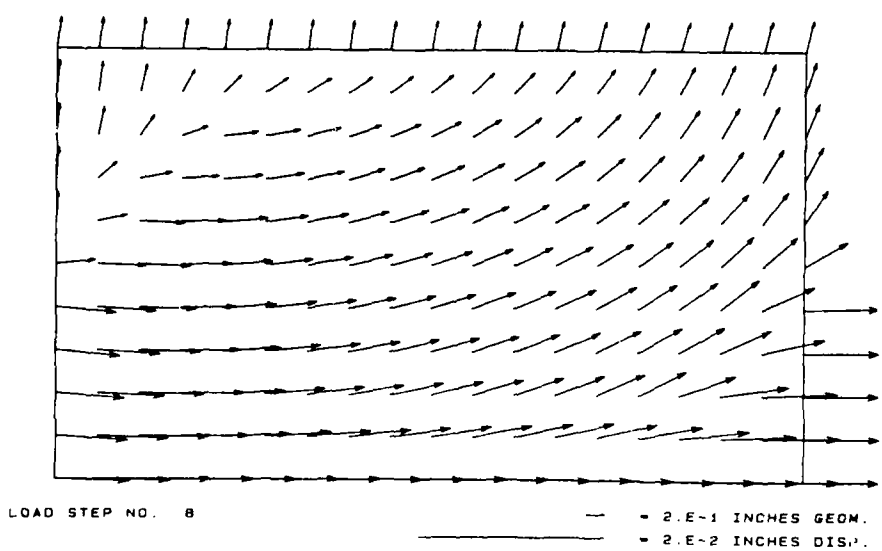

Fig 6-23 Direct shear test - displacement vectors for load steps 4 and 8

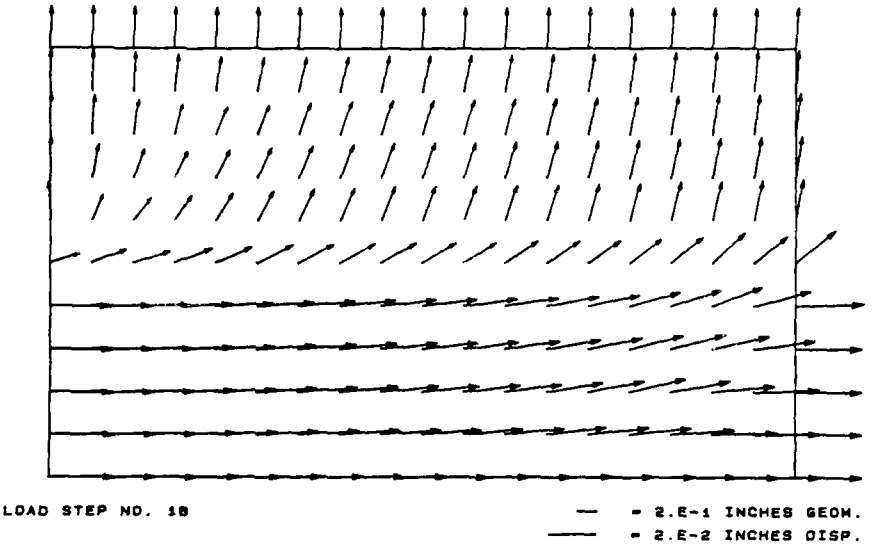

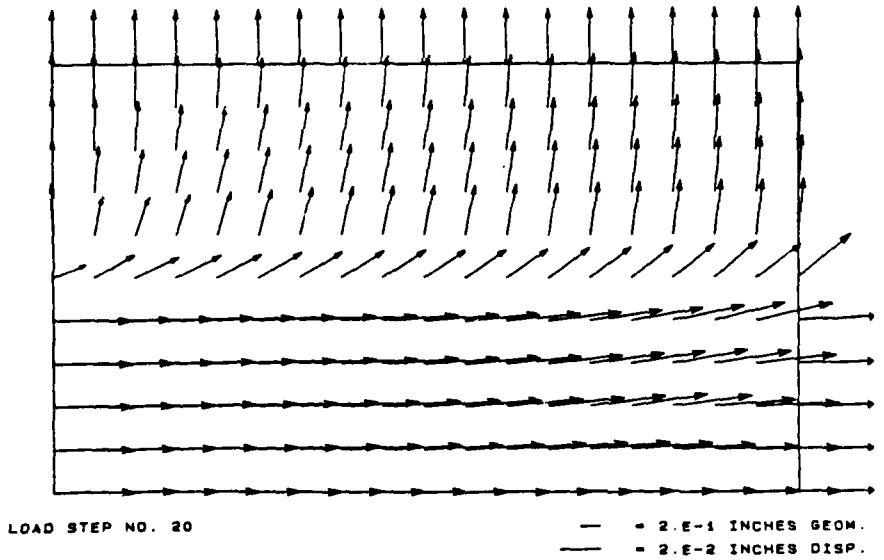

Fig 6-23.a Direct shear test - displacement vectors for load steps 16 and 20

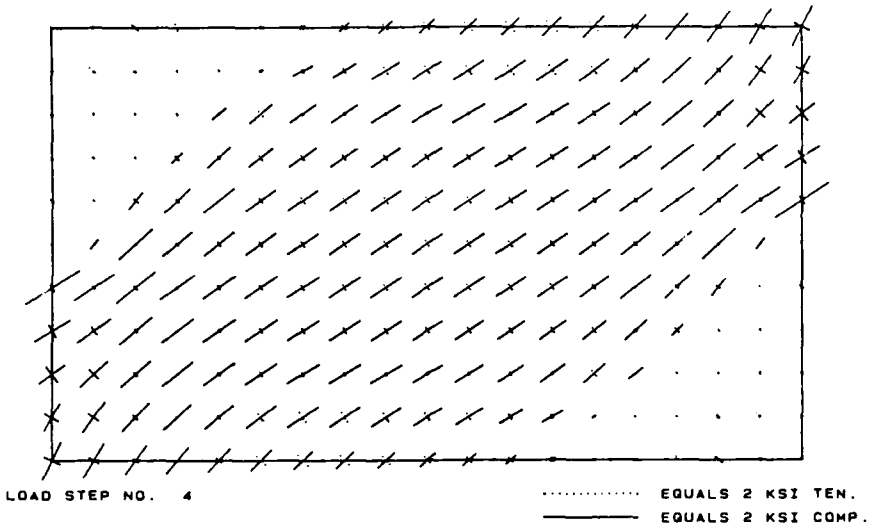

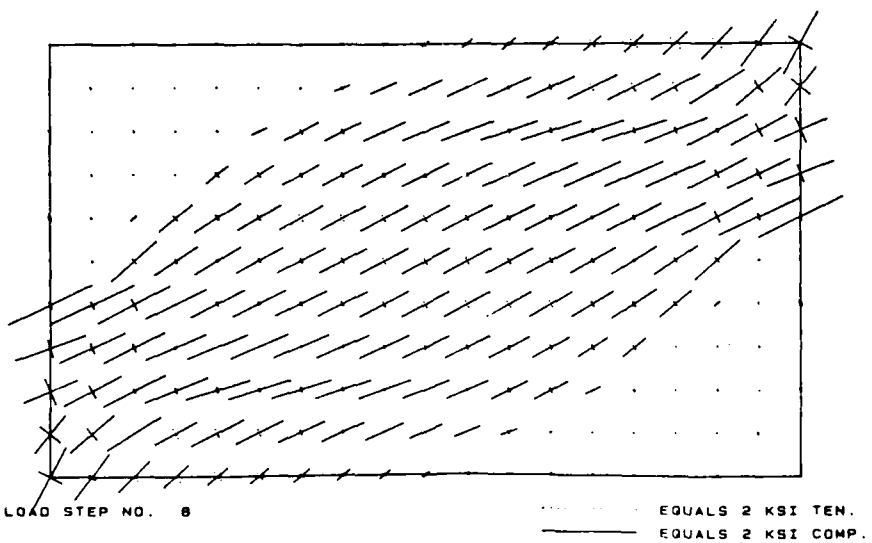

Fig 6-24 Direct shear test - principal stresses for load steps 4 and 8

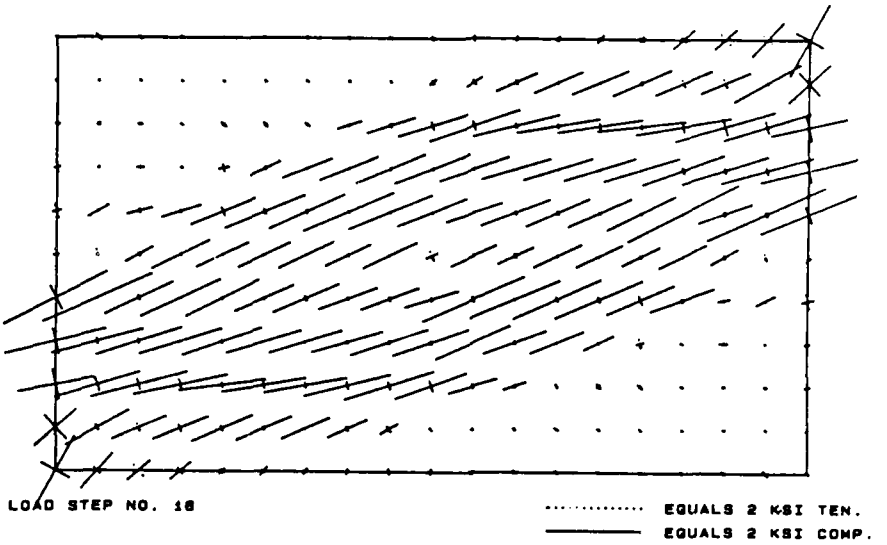

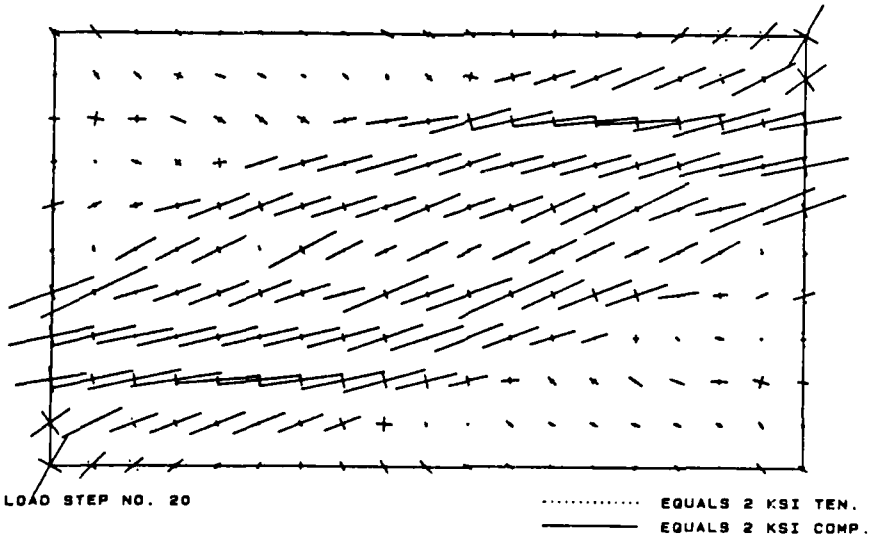

Fig 6-24.a Direct shear test - principal stresses for load steps 16 and 20

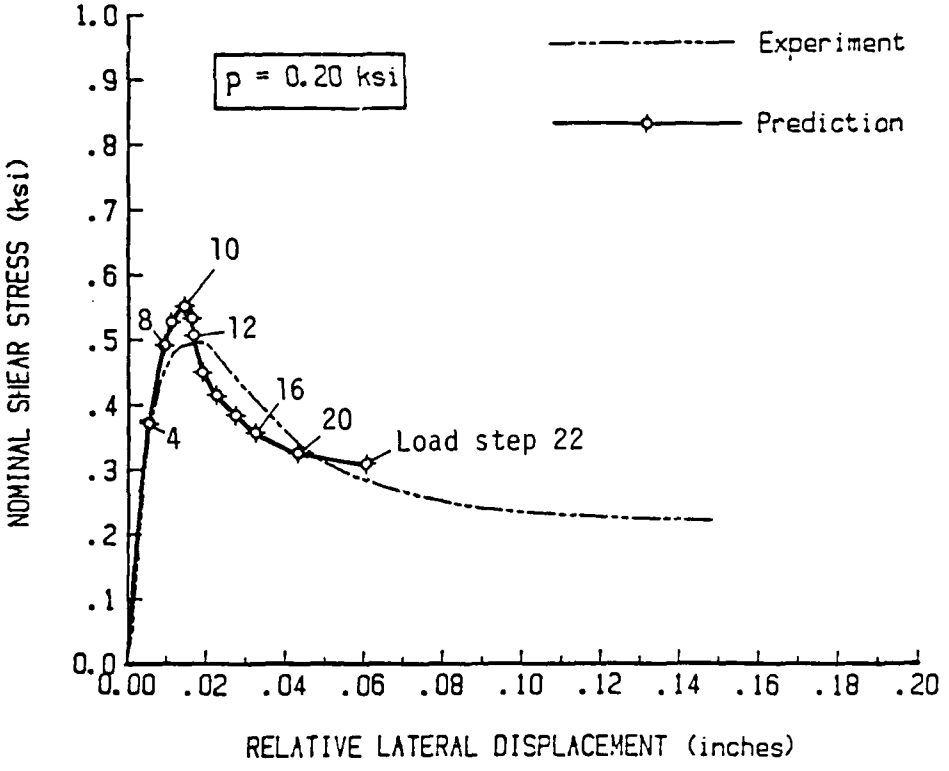

Fig 6-25 Comparison of the Predicted to the Experimental Response (p=0.20 ksi)

6-23a,b illustrate the nodal displacement vectors at the same stages. Significant tendency of vertical displacement is noted. Recall that similar experimented evidence is reported earlier in Chapter 3 (see Fig. 3-13)

Figures 6-24a,b show the distribution of the principal stresses during different response regimes. The figures illustrate the significant rotation of the principal stress directions as contained tensile cracking leads to the formation of compression struts, particularly at the lower normal load levels.

The load versus displacement response of the finite element model is shown in Fig. 6-25 compared with the experimental response curve. The prediction shows good agreement with the experimental response in the pre-peak regime. Response in this regime is controlled primarily by the modulus of elasticity and the initial fracture surface. In the post-peak regime the predicted response curves demonstrate surprisingly good agreement with the experimental response curve in view of the calibration of tensile and shear fracture parameters from a totally different set of test data and mesh layouts.

The accuracy of the numerical prediction is expected to be further improved with increasing normal pressure. Low values of normal pressure lead to the formation of large zones of tensile cracking, and the calibration of d_t was based only on very limited number of direct tension tests. High values of normal pressure reduce these zones of tensile cracking and enforce predominantly shear slip to occur. Since d_s was determined from triaxial compression tests under different confining pressures the prediction for the higher normal pressure tests where shear failure dominates the structural response is expected to be improved.

7. CONCLUDING REMARKS

The research report focused on brittle and ductile fracture phenomena and the computational failure prediction of structural components made of cementitious materials. The main thrust of the study was concerned with the basic issues of strain localization during fracture and stable finite element modeling of strain-softening materials. A composite damage model was developed to incorporate localized material damage into an equivalent smeared finite element approach for tensile cracking and frictional slip. Two localization parameters were introduced which define the extent of the damage zones in which strain-softening behavior takes place independently of the mesh size. The correspondence to fracture energy concepts was finally established whereby the computational complications of the discrete fracture analysis model could be circumvented.

Since the post-peak behavior is really a structural rather than a material property an inverse identification procedure was developed in order to calibrate the governing fracture parameters of localized damage. To this end displacement controlled uniaxial tension and triaxial compression tests were carried out in-house independently from the direct shear tests for verification of the smeared fracture computations. The effect of confining pressure on ductility was incorporated in the composite damage model in order to allow for a continuous transition from perfectly brittle fracture to perfectly plastic flow.

The computational fracture predictions were verified with experimental results from our large capacity direct shear test

apparatus. Depending on the ratio of normal to tangential loading contained fracture took place within the structurally stiff shear box device either in the form of predominantly tensile cracking or frictional slip. Consequently, the direct shear test experiment was considered representative for the actual fracture conditions within highly confined structures.

The numerical mesh sensitivity studies clearly indicated that the size of the damage zone V_d is not a mesh-independent fracture property. In fact, the computational results demonstrated instead that the damage volume fraction $\alpha = V_d/V_t$ should be kept constant for distributed fracture process. This observation is synonymous to saying that no explicit size effect has to be introduced in the softening formulation of the equivalent continuum element, quite in contrast to recent proposals of prominent researchers who suggest that the characteristic size of the fracture band must be considered. This leads to the conclusion that the composite damage models within the framework of softening plasticity, viscoplasticity or internal variable based damage theories provide an appropriate constitutive format for the progressive development of microdefects in structures . In fact there is little evidence for the explicit inclusion of size effects except for tensile cracking in highly localized fracture problems in which the fracture energy release should be kept constant rather than the damage volume fraction.

ACKNOWLEDGEMENTS

This research was sponsored by the U.S. Air Force Office of Scientific Research under contract AFOSR 82-0273 with the University of Colorado, Boulder. The authors would like to acknowledge the liason efforts of Lt. Col. John Allen and Lt. Col. Lawrence Hokanson and their support of this work. They would also like to thank Mrs. Shari Day for her help in preparing this report.

8. REFERENCES

[1] Sture, S. and H.Y. Ko, "Strain Softening of Brittle Geological Materials", Int. J. Num. Anal. Meth. Geomech. 2 (1978), pp. 237-254.

[2] Sture, S., "Experimental Modeling of Strength and Deformation Behavior of Concrete in Direct Shear", Proceed. Symp. on Interaction of Non-Nuclear Munitions with Structures, USAF Academy, Colorado Springs, May 10-13 (1983), pp. 95-100.

[3] Heilmann, H.G., "Zugspannung and Dehnung in unbewehrten Beton-querschnitten bei exzentrischer Belastung", Deutscher Ausschuss fur Stahlbeton, Issue 269, Berlin (1976), pp. 1-61.

[4] Petersson, P.T., "Fracture Energy of Concrete: Model of Determination Cement and Concrete Research, Vol. 10, (1980), pp. 78-89.

[5] Gopalaratnam, V.S. and S.P. Shah, "Softening Response of Concrete in Direct Tension", submitted for publication to ASCE, STD, Dec. 1983.

[6] Argyris, J.H., Faust, G. and K.J. Willam, "Limit Load Analysis of Thick-Walled Uniaxial Structures a Finite Element Approach to Fracture", Comp. Meth. Appl. Mech. Eng. Vol. 8, (1976) pp. 215-243.

[7] Christensen, J., Ickert, K., Stankowski, T., Sture, S. and K. Willam, "Numerical Modeling of Strength and Deformation Behavior for Engineering Materials", C. S. Desai and R. H. Gallagher eds. Tucson, Arizona, Jan. 10-14, 1983, pp. 537-544.

[8] Pietruszczak, St. and Z. Mroz, "Finite Element Analysis of Deformation of Strain-Softening Material", Int. J. Num. Meth. Eng., Vol. 17 (1981), pp. 327-334.

[9] Bazant, Z.P. and B.H. Oh, "Crack Band Theory for Fracture of Concrete", Rilem-Materiaux et Constructions, Vol. 16, No. 93 (1983), pp. 155-177.

[10] Hillerborg, A., Modeer, M. and P.E. Petersson, "Analysis of Crack Formulation and Crack Growth in Concrete by Means of Frac Mechanics and Finite Elements", Cement and Concrete Research, Vol. 6, (1976), pp. 773-782.

[11] Saouma, V.E. and A.R. Ingraffea, "Fracture Mechanics Analysis of Discrete Cracking", Proc. IABSE Conf. on Advanced Mechanics of Reinforced Concrete, Delft, June 2-4, 1981, pp. 393 - 416.

[12] Rudnicki, J.W. and J.R. Rice, "Conditions for the Localization of Deformation in Pressure-Sensitive Dilatant Materials", J. Mech. Phys. Solids, Vol. 23, (1975), pp. 371-394.

[13] Vardoulakis, I., "Bifurcation Analysis of the Triaxial Test on Samples", Acta Mechanica, 32, (1979), pp. 35-54.

[14] Vermeer, P.A., "A Simple Shear Bank Analysis Using Compliances", Proc. IUTAM Symp. on Deformation and Failure of Granular Materials, P.A. Vermeer and H.J. Luger, Eds., Delft, Aug. 31-Sept. 3, 1982, pp. 493-499.

[15] Hill, R., "A General Theory of Uniqueness and Stability in Elastic-Plastic Solids", J. Mech. Phys. Solids, Vol. 6, (1958), pp. 236-249.

[16] Needleman, A. and V. Tvergaard, "Finite Element Analysis of Localization in Plasticity", Chapter 3 in Finite Elements, Special Problems in Solid Mechanics Vol. 5, J.T. Oden and G.F. Carey Eds., Prentice-Hall, Englwood-Cliffs (1984), pp. 94-157.

[17] Dougill, J.W., "Constitutive Relations for Concrete and Rock: Applications and Extensions of Elasticity and Plasticity Theory", Preprints W. Prager Symp. on Mechanics of Geomaterials, Rocks Concrete Soils, Z. Bazant, Ed. Northwestern University, Evanston, Sept. 11-15, 1983, pp. 18-54.

[18] Naghdi, P.M., and J.A. Trapp, "The Significance of Formulating Plasticity Theory with Reference to Loading Surfaces in Strain Space", Int. J. Eng. Sci., Vol. 13 (1975), pp. 785-787.

[19] Kachanov, L.M., "On the Creep Fracture Time", ANSSSR, Otn, Tekhn. Nauk, Vol. 8, (1958), pp. 26-31.

[20] Lemaitre, J. and J.L. Chaboche, "Aspet Phenomenologique de la Rupture par Endommagement", J. de Mec. Appl., Vol. 2, (1978), pp. 317-365.

[21] Krajcinovic, D. and G.U. Fonseka, "A continuous Damage Theory of Brittle Materials", J. Appl. Mech., Vol. 48 (1981), pp. 809-815.

[22] Chen, W.F. and A.F. Saleeb, "Constitutive Equations for Engineering Materials, Vol. 1: Elasticity and Modeling", J. Wiley & Sons, New York, 1982.

[23] Hadamard, J.S., "Lecons sur la Propagation des Ondes", Chelsea Publ. Co., New York, 1949, Chapter 6.

[24] Dougill, T.H., "A Mathematical Model for Progressive Failure of Cement Paste and Mortar", Magazine of Concrete Research, Vol. 19 (1967), pp. 135-142.

[25] Maier, G., Zavelani, A. and J.C. Dotreppe, "Equilibrium Branching due to Flexural Softening", J. ASCE, Vol. 99, EM4 (1973), pp. 897-901.

[26] Bazant, F.P., "Instability, Ductility and Size-Effect in Strain-Softening Concrete", J. ASCE, Vol. 102, EM2 (1976), pp. 331-344.

[27] "Fracture Mechanics of Concrete", ed. F.H. Wittmann, Elsevier, Amsterdam, 1983.

[28] Bazant, Z.P. and L. Cedolin, "Fracture Mechanics of Reinforced Concrete", J. ASCE Vol. 106, EM6 (1980), pp. 1287-1306.

[29] Rice, J.R., "A Path-Independent Integral and the Approximate Analysis of Strain Concentration by Notches and Cracks", J. Appl. Mech, Vol. 6 (1968), pp. 379-386.

[30] Parks, D.M., "A Stiffness Derivative Finite Element Procedure for Determination of Crack Tip Stress Intensity Factors", Int. J. Fract. Vol. 10 (1974), pp. 487-502.

[31] Doltsinis, J. St., Zur Berechnung des Rissfortschmitts in Inelastischen Tragwerken," ZAMP, Vol. 30 (1979), pp. 58-63.

[32] Morgenstern, N.R. and J.S. Tchalenko, "Microscopic Structures in Kaolin Subjected to Direct Shear," Geotechnique, Vol. 17 (1967), pp. 309-328.

[33] Kutter, H.K., "Stress Distribution in Direct Shear Test Samples," Proc. Int. Symp. Rock Mech., Nancy, France, 4-6 Oct., 1971, paper II-6.

[34] Mandl, G., L.N.J. deJong and A. Maltha, "Shear Zones in Granular Material," Rock Mechanics, Vol. 9 (1977), pp. 95-144.

[35] Vallejo, L.E., "Development of a Shear Zone Structure in Stiff Clays," Proc. 4th Intl. Conf. Num. Meth. Geomech., Vol. 1, Edmonton, Canada, May 31-June 4, 1982, pp. 255-262.

[36] Walters, J.V. and J. N. Thomas, "Shear Zone Development in Granular Materials," Proc. 4th Intl. Conf. Num. Meth. Geomech., Vol. 1, Edmonton, Canada, May 31-June 4, 1982, pp. 263-279.

[37] Desai, C.S. and M.M. Zaman, "Models for Sliding and Separation at Interfaces under Static and Cyclic Loading," Proc. Int. Conf. on Constitutive Laws of Engineering Materials, C.S. Desai and R. H. Gallagher, eds., Tucson, Arizona, Jan. 10-14, 1983, pp. 383-392.

[38] Christensen, J.D., "Computational and Experimental Investigation of Concrete Failure in Shear", M. Sc. Thesis, Department of Civil, Environmental and Architectural Engineering, University of Colorado, Boulder, 1983.

[39] SMART I, Users Reference Manual, ISD Report, University of Stuttgart, 1976.

[40] Krempl, E., "Viscoplasticity Based on Overstress Experiment and Theory", Chapter 19 in Mechanics of Engineering Materials, C.S. Desai and R.A. Gallagher, Eds., J. Wiley and Sons, to appear 1984, pp. 369-384.

END